8

The Contrast Formation in Optical Microscopy

Ping-Chin Cheng

INTRODUCTION

In any form of microscopy, one needs not only an imaging system with enough resolution to delineate the fine details of the specimen but also a suitable contrast mechanism by which to "see" the shape of the structures of interest. Contrast is the difference between the signal in one pixel and that in another that conveys to the viewer information about the shape of the specimen. It is the difference between a blank screen and an image.

In photographic terms, contrast is the change in brightness of a negative or print. In other words, contrast is the difference in signal strength between various parts of an image or between details of interest and "background" (see also Chapter 4, *this volume*). The contrast (γ) is proportional to the intensity difference (ΔI) between two image areas, divided by the average image brightness $\bar{I}$.

$$\gamma = \frac{\Delta I}{\bar{I}}$$

In optical microscopy, contrast derives from differences in the way the various sub-volumes of the specimen (voxels) interact with the illumination. This interaction may include linear and nonlinear absorption, single- and multiple-photon fluorescence, Raman emission, fluorescence spectral shift, fluorescence lifetime, refraction, reflection, phase shift, scattering, changes in polarization, harmonic generation, etc. A contrast mechanism can thus be considered to be a special "filter" function by which specific types of spatial or temporal signals are selected to form a two-dimensional (2D) or three-dimensional (3D) image.

This chapter will provide an introduction to the contrast characteristics of those modalities that have been well investigated in confocal and nonlinear microscopy, including fluorescence and scattering contrast. It will also consider the deleterious influence on the confocal and multi-photon image of the absorptive, refractive, and reflective properties of structures that are between the plane-of-focus and the objective lens, of these topics are relevant to the operation of all epi-illuminated microscopes and some also apply to signals detected in transmission, particularly as used to detect second harmonic (SHG) and third harmonic (THG) signals.

In addition, this chapter will introduce ways in which the contrast present in the raw data from the microscope can be digitally modified before being presented in the final image. At various stages in this sequence, the signal may be ratioed, filtered, and corrupted and the contrast reduced by the addition of noise. In all these areas, this chapter serves as an introduction to other chapters in which individual contrast mechanisms are discussed in more depth.

Image contrast arises from the interaction of an incident light beam with the specimen. Various physical and digital "filters" can be used to select specific signals. For example, one can discriminate specific wavelengths using dichroic beam-splitters and barrier filters; the effective numerical aperture (NA) of the objective lens can produce topographic contrast from the geometric shape of specimen surfaces; polarized light can be used to obtain contrast caused by specimen birefringence; and fluorescence signals from ion-specific dyes in two different spectral channels can be ratioed to detect the concentration of ions such as $[Ca^{++}]$ and $[H^{+}]$.

The contrast that forms a microscopic image is determined by the number of physical, chemical, and biological phenomena. Contrast mechanisms can be subdivided into (a) optical contrast, (b) geometric contrast, (c) biological and chemical contrast, and (d) synthetic contrast. From the point of view of the specimen, the contrast mechanism can be intrinsic or extrinsic in nature. Although each of these contrast mechanisms will be discussed separately, it is not uncommon for more than one to be active at the same time and care must be taken to choose experimental parameters that emphasize the contrast that highlights the most informative of these interactions.

The interaction of an incident light beam with a sample is a complex event. Figure 8.1 shows a simplified version of such an interaction as well as some of the effects produced by the voxels above and below the voxel being sampled. These interactions give rise to the optical phenomena and the photochemical and biochemical effects that provide the bases of all the contrast.

When a beam of light with intensity I_0 is incident on a specimen, a number of physical phenomena may occur. These include the scattering of light due to Rayleigh, Mie, and Raman scattering (I_{S_R}, I_{S_M}, *and* I_{S_Raman}). Rayleigh scattering is caused by interactions with very small particles in the specimen (from the size of molecules up to ~10% of the wavelength) and its strength (I_{S_R}) is strongly wavelength dependent. It also depends on direction: scattering at right angles to the illumination is only half the forward intensity (I_{S_R}). Rayleigh scattering is elastic scattering because the scattered photons have the same energy as the incident photons.

By contrast, scattering in which the scattered photons have either a slightly higher or lower photon energy is called Raman scattering (I_{S_Raman}). This energy change usually involves either the excitation of some vibrational mode of the molecule (giving the scattered photon a lower energy), or the scattering of the photon off an excited vibrational state of a molecule (which adds its vibrational energy to the incident photon).

Cell organelles and other refractive structures larger than the wavelength of the illumination contribute to Mie scattering (I_{S_M}).

P.C. Cheng • State University of New York at Buffalo, Buffalo, New York 14260 and National University of Singapore, Singapore

 Handbook of Biological Confocal Microscopy, Third Edition, edited by James B. Pawley, Springer Science+Business Media, LLC, New York, 2006.

Mie scattering has a sharper and more intense forward lobe for larger particles than Rayleigh scattering (Fig. 8.2), is not wavelength dependent and is responsible for the almost white appearance of adipose and brain tissue. Such a scattering center can act as a secondary light source within the specimen.

In addition to these scattering events, refractive index (RI or **η**) differences between various biological structures can cause the incident ray to deviate from its original path, producing defocusing or sampling errors (i.e., imaging the signal from the "wrong" voxel). Reflection occurs at any interface separating regions of different RI.

The incident light can also be attenuated by absorption. Photon absorption occurs when the quantum energy of the photon matches the energy gap between the initial and final states of some electron in the specimen. If no pair of energy states exists such that the photon energy can elevate an electron from a lower to an upper state, then the matter is transparent to this radiation. In the absorption process, some of the absorbed energy can be re-emitted in the form of a fluorescent or phosphorescent photon. Biological molecules have specific absorption characteristics and the low effective absorbance of most tissue provides a relatively transparent "window" in the visible and near-infrared range (NIR). This window provides the working spectrum for all the optical microscopy (see Figs. 21.1 and 40.2, *this volume*). When the incident light intensity is very high, nonlinear optical phenomena such as nonlinear absorption, multi-photon fluorescence, and harmonic generation of incident light become prevalent (Fig. 8.1).

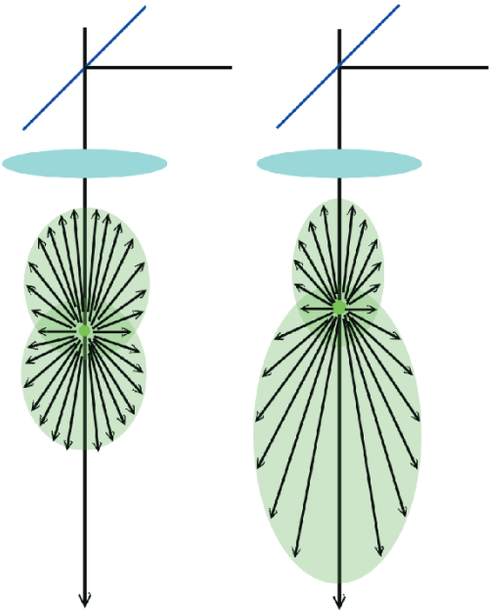

FIGURE 8.2. Rayleigh scattering (left) and Mie scattering (right). In Mie scattering, the forward lobe becomes larger as particles become larger. This is the reason that dark-field illumination produces more signal in transmission than in epi mode.

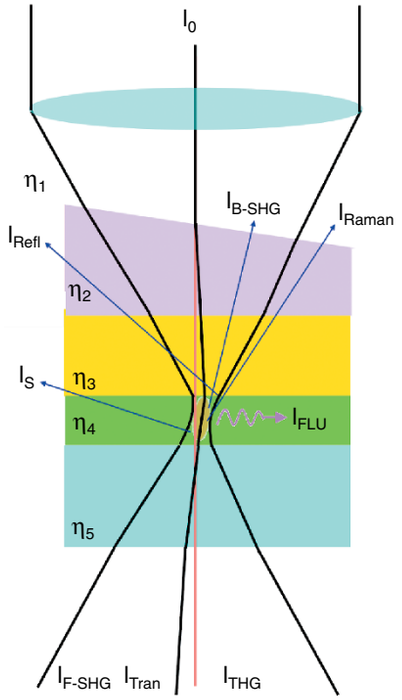

FIGURE 8.1. Interaction of light with a voxel of the specimen. The hypothetical specimen consists of four layers with different RIs (n2, n3, n4, n5) and the surface of the top layer is slanted with respect to the optical axis. The illuminating beam (I_0) is refracted by the surface of the top layer (pink) and subsequent layers with the result that the focal spot is not on the original optical axis (red line). Various signals, including fluorescence (I_{FLU}), scattering (I_S), reflection (I_{Refl}), Raman (I_{Raman}), second harmonic generation in both forward and backward direction ($I_{B\text{-}SHG}$ and $I_{F\text{-}SHG}$), and third harmonic generation (I_{THG}) may be produced when conditions are favorable. The pink spot at the focus indicates the volume where nonlinear phenomena prevail at high illumination intensity. Transmission intensity, I_{Tran}.

It is well known that different RIs can be associated with different crystallographic orientations of crystalline materials. For example, calcite crystals have indices of refraction for the o- and e-rays of 1.6584 and 1.4864, respectively. Mineral crystals showing two distinct indices of refraction are referred to as birefringent materials. Birefringence has to do with anisotropy in the binding forces between the atoms forming a crystal. A large number of quasi-crystalline biological materials also exhibit birefringence (Fig. 8.3).

SOURCES OF CONTRAST

Absorption Contrast

If the light–specimen interaction is predominantly photon absorption (as it is in the prepared tissue sections, stained with absorbing dyes), and the specimen has a uniform thickness [Fig. 8.4(A)], and if the incident light is I_0, then the transmitted intensity, I_1 and I_2 through structures 1 and 2 in the voxel being sampled is:

$$I_1 = I_0 e^{-\mu_1 x}$$

and

$$I_2 = I_0 e^{-\mu_2 x}$$

where μ_1 and μ_2 are the absorption coefficients of structures 1 and 2, respectively, and x is the length of the absorption path (the thickness of the voxel in this case). The contrast due to absorption (γ_{abs})

$$\gamma_{abs} = \frac{\Delta I}{\bar{I}} = \frac{I_1 - I_2}{\bar{I}}$$

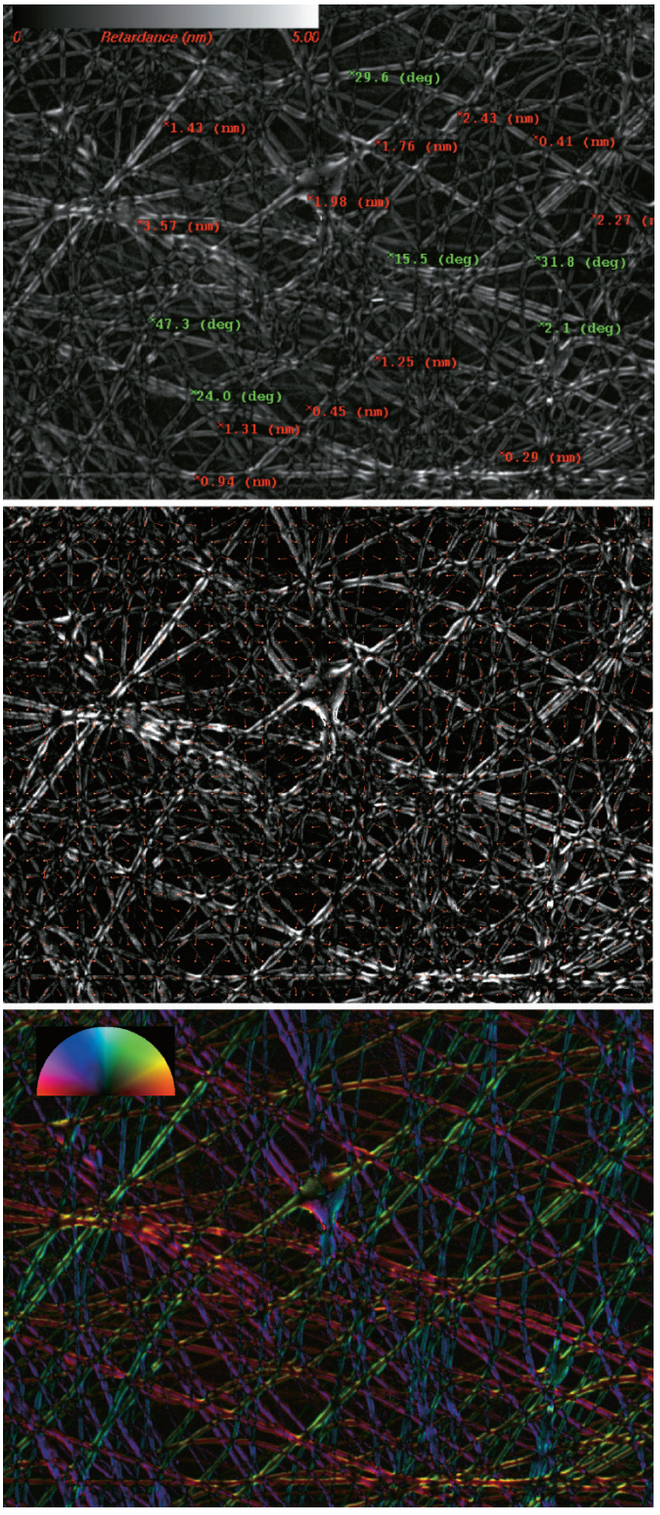

FIGURE 8.3. Birefringence of artificially reconstituted collagen fibers. (Upper) A retardance image of collagen fibers. (Middle) Orientation of the collagen fibers indicated by small arrows. (Lower) Orientation coded as color. [Images courtesy of Hanry Yu, Department of Physiology, National University of Singapore and made using a Polscope (Cambridge Research Inc., Cambridge, MA).]

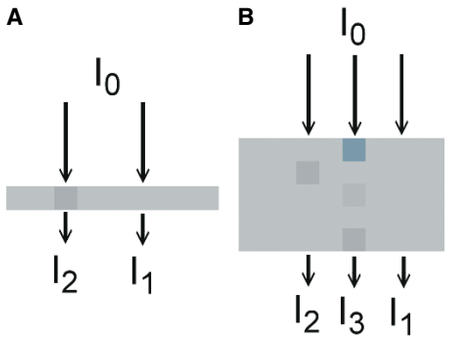

FIGURE 8.4. Hypothetical thin (A) and thick (B) specimens composed of a light-absorbing matrix with an absorption coefficient of μ_1 and containing small structures with an absorption coefficient of μ_2. The transmission intensities of the matrix and structure are I_1, I_2, and I_3, as marked.

However, in real specimens, the structure of interest is generally much smaller than the thickness of the specimen and therefore, it resembles the situation in Figure 8.4(B), the effective absorption coefficient μ_T for a given light path is:

$$\mu_T = \sum_{i=1}^{m} \mu_i$$

a term that describes an absorbing specimen composed of m different subunits, each having an absorption coefficient (μ_i), where μ_T is the absorption coefficient associated with the light attenuation along the specific light path.

For a sample with thickness x, and the effective absorption coefficients of an area of interest (μ_{T1} and μ_{T2}), the absorption contrast (γ_{abs}) is:

$$\gamma_{abs} = \frac{\Delta I}{\bar{I}} = \frac{I_1 - I_2}{\bar{I}} = I_0\left(e^{-\mu_{T_1}x} - e^{-\mu_{T_2}x}\right)\Big/ I_B$$

where $\bar{I} = \dfrac{\sum_{k=1}^{n} I_0 e^{-\mu_k x}}{n} = \dfrac{I_0 \sum_{k=1}^{n} e^{-\mu_k x}}{n} \approx I_B$ and n is the number of pixels in the image. The absorption contrast (γ_{abs}) between pixel 1 and 2 shown in Figure 8.4(B) is:

$$\gamma_{abs} = I_0\left(e^{-\mu_{T_1}x} - e^{-\mu_{T_2}x}\right) \cdot e^{\mu_B x}$$

The Rose criterion (Rose, 1948) relates contrast and noise to visibility. It states that, to be visible, the contrast between a feature and its surroundings must be 5 times the noise in the surroundings [signal-to-noise ratio (S/N) >5 : 1],

$$e^{(\mu_2 - \mu_1)x} \geq 5$$
$$(\mu_2 - \mu_1)x \geq \ln 5$$
$$\mu_2 - \mu_1 \geq \frac{\ln 5}{x}$$

Apart from the fact that the optical transfer function implies that small features will be rendered in the image with less contrast than large ones and that the Poisson noise associated with recording any image adds uncertainty to the measurement of contrast, large features will also have low contrast if the tissue is only lightly stained, and small, intensely stained structures will have less contrast when visualized inside a thick, stained region of the sample. Finally, unstained biological tissues contain few molecules that absorb in the visible and our ability to detect small changes in

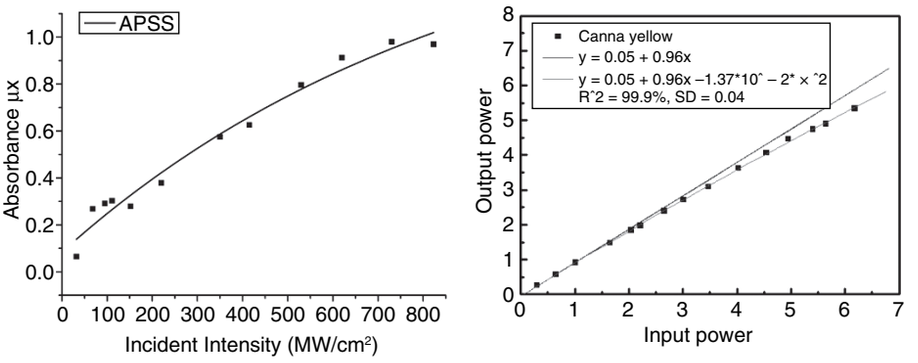

FIGURE 8.5. Nonlinear absorption of the up-converting dye, APSS, and of an ethanol extract of yellow petal of *Canna*, as a function of excitation light intensity.

absorbance by eye is poor. For all these reasons, linear absorbance contrast is used mainly on material that has been fixed and stained.

If one increases the incident intensity, the optical response of the specimen will eventually begin to show significant nonlinear components; in fact, the optical response can be described by the following power series $[\tilde{P}(t)]$:

$$\tilde{P}(t) = \varepsilon_0\chi^{(1)}\,\tilde{E}(t) + \varepsilon_0\chi^{(2)}\,\tilde{E}(t)^2 + \varepsilon_0\chi^{(3)}\,\tilde{E}(t)^3 + \ldots$$
$$\equiv \tilde{P}^{(1)}(t) + \tilde{P}^{(2)}(t) + \tilde{P}^{(3)}(t) + \ldots$$

where $\chi^{(1)}$ is the linear susceptibility, $\chi^{(2)}$ is the second-order nonlinear susceptibility, and $\chi^{(3)}$ is the third-order nonlinear susceptibility. The effective nonlinear absorption cross-section $\mu(I_0)_{eff}$ is a function of the incident intensity. The nonlinear transmission intensity,

$$I_{trans\_nonlinear} = I_0 e^{-\mu(I_0)_{eff}\cdot x}$$

assuming the concentration of the pigment is relatively low, and that fluorescence is not a factor. Figure 8.5 shows the effective absorbance, $\mu(I_0)_{eff}\cdot x$, plotted against the incident illumination for a solution of the up-converting dye, APSS [Fig. 8.5(A)] and a methanol extract of yellow *Canna* petals [Fig. 8.5(B)], when illuminated with 780 nm NIR light from a Ti:sapphire mode-lock laser (85 MHz, 120 fs pulse). If, as in these cases, the absorber is a fluorophore, this nonlinear absorption may produce fluorescence.

The absorption properties of a specimen (color or opacity) can have a negative impact on image contrast in the backscattered light (BSL) mode. For example, the nearly opaque carbon particles in the polyethylene cable material, shown in Figure 8.6, cause a significant loss in signal intensity by attenuating both the illuminating beam and the BSL signal.

Although deep coloration in biological specimens, such as that caused by pigment granules and chloroplasts, can also have this

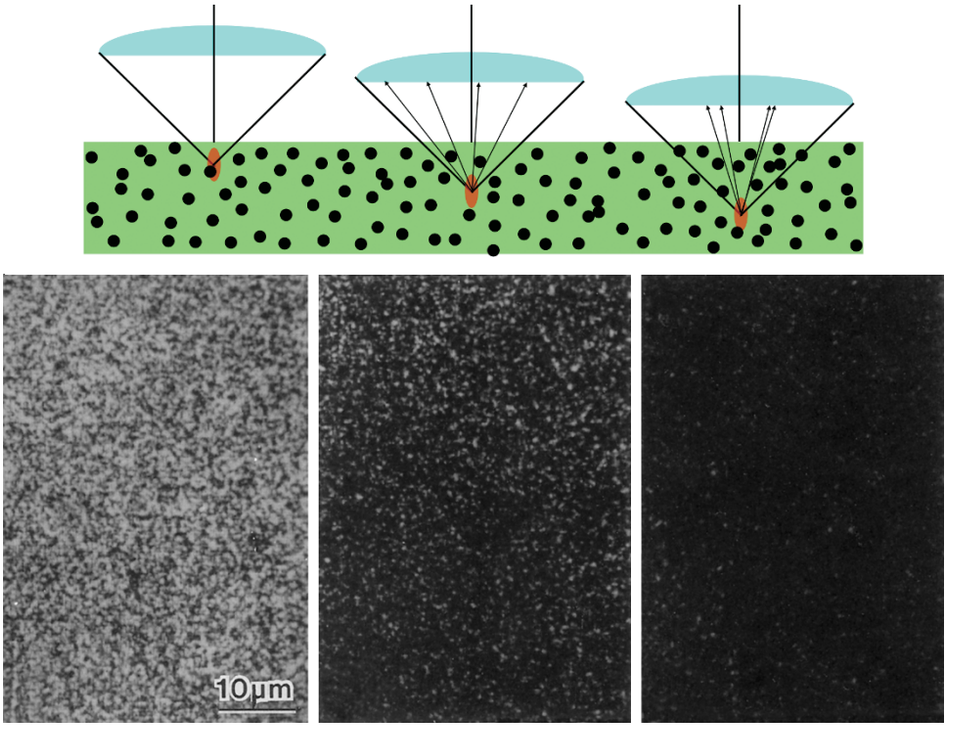

FIGURE 8.6. (Top) When the objective is focused into a particle-filled clear matrix, the scattered and reflected rays from the structure of interest are modulated by the particles located between the objective and focal plane. (Bottom) Diagram of self-shadowing.

effect, the problem can sometimes be minimized by selecting a λ that reduces absorption to a minimum. For example, when imaging plant cells, green illumination will be absorbed much less than blue or red. As many biological and polymeric specimens are very transparent to IR, it is sometimes worthwhile surrendering some resolution by using a longer λ in order to penetrate deeper into the specimen. For example, NIR (700–1200 nm) radiation can be used to study the internal structure of insects because insect cuticle is relatively translucent in this region of the IR spectrum. This improvement is due to lower absorbance and also to decreased Rayleigh scattering, which is proportional to λ^4. The other side of the equation is that objects of interest must now be somewhat larger to produce a detectable BSL signal.

Modern confocal microscopes are generally operated in an epi-illuminated configuration, both in fluorescence and BSL mode. However, it is also possible to operate the confocal microscope in the trans-illumination configuration to image absorption contrast (An *et al.*, 1990). The straightforward approach to designing a transmitted confocal microscope is to mount two opposed microscopes on a common optical axis with both objective lenses focused on a common point in a specimen. One serves as the light source and the other as the detector. Rastered images are obtained by scanning the specimen with an *xy* mechanical stage.

It is clear that such a design has some major drawbacks: (1) The stage scanning method is relatively slow and not suitable for most biological specimens because of the stage vibration involved. (2) In a beam-scanning system (either with a single laser beam or the multiple beams of a disk-scanning system), it is technically difficult to synchronize the scanning of separate illumination and detection systems perfectly. (3) Because of differences in the RI and optical path length within the specimen, a small translation of the specimen along the optical axis (*z*) can result in significant misalignment of the focal points of the two opposed objectives, reducing signal levels. Unfortunately, 3D sets of optical-section images can only be obtained by translation in *z* (Chapter 30, *this volume*).

Cheng and Lin (1990) demonstrated a simple trans-illuminated confocal design utilizing folded optics [Fig. 8.7(A)]. The design uses a second high-NA, infinity-corrected objective that is coaxial and confocal with the primary objective so that light transmitted through the specimen is captured by this second lens. A mirror normal to the optical axis and placed behind the second objective reflects the transmitted light back to the first objective along the same path, and a confocal configuration is maintained as long as the second objective remains confocal with the primary objective.

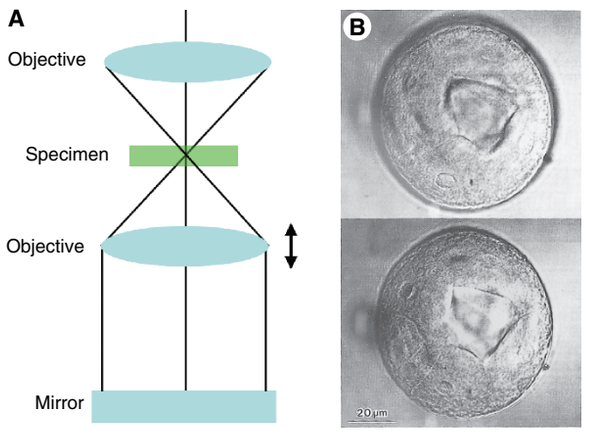

FIGURE 8.7. (A) Diagram of a double-pass, trans-illumination folded optical setup for trans-illuminated confocal light microscopy. (B) A set of trans-illuminated confocal images of a sea urchin embryo (*S. purpuratus*). The optical sections were obtained at 4 µm apart. The specimen was fixed in 3 : 1 (ethanol/acetic acid), stained by the Feulgen method, dehydrated, and cleared in methyl salicylate.

The problem is that any misalignment between the two objectives caused by moving an optically heterogeneous specimen in the *x*-, *y*-, or *z*-direction will cause a large reduction in signal, even in the absence of any absorptive dye. To avoid this, we have developed a computer-controlled, precision piezoelectric/mechanical system that allows precise positioning of the second objective lens by monitoring intensity changes in the captured image. Figure 8.7(B) shows two series of optical sections of a sea urchin embryo (*Strongylocentrotus purpuratus*) obtained in the transmitted, confocal mode using a laser scanning system. This set of images was obtained by realigning the folding optics after each focus change (4 µm total). Contrast in these images results primarily from absorption by the specimen summed over both passes, but there is also a small contribution from BSL and interference between the two beams. The effect of the BSL in the image can largely be removed by subtracting a pure BSL image from the absorption image.

Because the sensitivity for detecting absorptive tags is inherently low and because any optical misalignment caused by refractile organelles produces a signal reduction that can be confused with such absorption, transmitted confocal microscopy is unlikely to become an important imaging modality. However, this optical scheme can be used for forward-SHG detection in an epi-illumination setup.

With this basic transmitted optical system, a wide variety of interference contrast mechanisms can be implemented by adding the appropriate optical components into the back-focal plane of one or both objectives, or simply by using mirrors that cover only parts of these planes. Such images can, in principle, be collected in addition to, and independently of, any fluorescent signals (see Chapters 2, 9, and 30, *this volume*). For example, Cogswell (1994) demonstrated confocal imaging of both phase and amplitude objects. To optimize the optical conditions of both objectives, the specimen must be sandwiched between two coverslips instead of a microscope slide and a coverslip (Cheng *et al.*, 1994).

A bonus feature of this transmitted configuration is a small improvement in the signal strength when the microscope operates in epi-fluorescence mode. The folded optical path provides double excitation and, in addition, much of the fluorescent light captured by the lower objective lens is returned to the detector. Assuming that the dye is not close to singlet saturation and that the transmittance of the second objective is high, the system can increase fluorescence signal strength 2 to 3×. Although this approach may be of some use with disk-scanning microscopes where fluorescence image intensity is relatively low, problems related to maintaining alignment between the many beams used in such a system may restrict its use to prepared specimens that are embedded in a clearing medium. In addition, as the folded light path corresponds to operating in transmission fluorescence rather than epi-fluorescence, the barrier filter in front of the detector must be very efficient to exclude stray excitation light (see Chapter 3, *this volume*).

As harmonically generated signals propagate preferentially in the forward direction, the trans-detection configuration is the preferred detection layout. However, the double-pass method does permit simple, descanned SHG and THG detection when beam-

scanning. Sun and colleagues (2005) have demonstrated that certain biological specimens also generate backward SHG, meaning that conventional epi-detection can also be used.

Scattering and Reflection Contrast

Scattering includes Rayleigh, Mie, and Raman scattering. While the strongly wavelength-dependent Rayleigh scattering originates from molecules, Mie scattering primarily results from cellular structures such as organelles. On the other hand, because Raman scattering is a non-elastic event, the scattered photon either loses or gains energy from the vibrational state of the molecule involved, and consequently the scattered light carries information about the state of the molecule. When the structure is much larger than the wavelength of light and presents a smooth RI interface or metal surface, reflection results. Depending on the size and geometry of the feature in the specimen that causes it, the light signal that proceeds from the specimen toward the detector in an epi-illuminated, widefield, or confocal microscope is commonly either referred to as either BSL or reflected light.

The intensity of the Rayleigh-scattered light I varies inversely with the 4th power of the wavelength.

$$I = I_0 \frac{8\pi^4 N\alpha^2}{\lambda^4 R^2}(1+\cos^2\theta)$$

where N is the number of scatters, α is polarizability, and R is the distance from the scatterer.

Mie scattering is generated mainly by the organelles in the cell and is not strongly wavelength dependent, but the scattering intensity is proportional to the square of the ratio of the RI of the feature and the RI of the media. If scattered light is not a desired signal, it can be greatly reduced if the specimen is "cleared" by immersing it in an index-matched liquid. This allows one to image significantly deeper into the tissue (see Chapter 49, *this volume*).

When light is incident on a smooth interface separating materials with different RIs, such as the water/oil droplet, the reflected intensity depends on the incidence angle and the RI difference. In geometric optics, when light travels from one medium to another of different RI, the light separates into two components: the reflected ray and the refracted ray. The degree of reflection depends on the gradient of RI between the two media. The refracted ray changes its propagation angle (θ_r) with respect to the incident beam (θ_i) as described by Snell's law:

$$\frac{\sin\theta_i}{\sin\theta_r} = \eta_{21}$$

where constant η_{21} is the RI of the second medium relative to the first medium. It can be expressed in terms of the refractive indices of η_1 and η_2.

$$\eta_1 \sin\theta_1 = \eta_2 \sin\theta_r$$

If the incident angle (θ_i) is greater than the critical angle (θ_c), where

$$\sin\theta_c = \eta_{21}\ \eta_{21} < 1$$

then total reflection results. In reflected-light confocal microscopy, the reflectance (i.e., the ratio of illumination intensity to reflected intensity) of the specimen is one of the key factors determining signal strength. The reflectance is the ratio of the difference of the squares of the refractive indices of the two media.

$$\frac{I_{refl}}{I_0} = \left(\frac{\eta_1 - \eta_2}{\eta_1 + \eta_2}\right)^2$$

Therefore, the smaller the difference in RI between the two media, the lower the reflectance. In living biological specimens, the RIs of most cellular structures differ very little from that of the surrounding aqueous medium, and hence, structures inside biological specimens have much lower reflectance than most materials sciences specimens. For example, the reflectance of a gold-coated glass surface (a mirror or an integrated circuit chip) can be >95% and that of the metallic silver deposited in a Golgi-stained neuron may be −10%, but the typical reflectance of the surface of a maize leaf (surface cuticle interface with air) is ~0.03% and the reflectance of human bone imaged under a confocal microscope and that of living specimens, such as tissue culture cells, is even lower. Detection of reflection from a curved surface can produce image contrast related to the curvature and the NA of the objective lens used (Fig. 8.8). Despite the low reflectance, confocal images of tooth enamel prisms and Golgi-stained Purkinje cells have been obtained (Boyde, 1985). Watson (1989) demonstrated real-time imaging of an internal section of a tooth being abraded by a dental burr by using a tandem-scanning confocal microscope (TSM) operated in BSL mode.

When viewed with a multi-channel (or spectral) confocal microscope, colloidal-gold particles as small as 5 nm can be detected because they appear much brighter under green laser illumination than under blue or red. This is because the molecular resonance properties of gold particles cause them to Rayleigh scatter green light more strongly than other visible wavelengths (Born and Wolf, 1980). As a result, it is possible to ratio the images obtained from the blue and green channels to identify the colloidal gold specifically (Cogswell, 1994). This technique can be used to study the colloidal gold-labeled samples prior to fixation for EM study.

When light passes through matter, some of it is scattered in random directions with a small energy gain or loss due to Raman scattering. If the initial beam is sufficiently intense and very monochromatic, a threshold can be reached[1] beyond which light at the Raman frequencies is amplified and the output generally exhibits the characteristic of stimulated emission. Raman spectroscopy is a powerful analytical method in microscopy. As early as 1992, Sharonov and colleagues (1992) used it in confocal microscopy. Image contrast in a Raman confocal image can result either from intensity variations at a selected energy level or from variations in the Raman spectra obtained from different optical sections. In the latter case, the basic image unit in such an *xyk* image is referred to as "lambxel" (Cheng *et al.*, 1994).

Because light reflecting from inclined surfaces may be deflected away from the objective lens, BSL images of silver-impregnated nerve cells appear punctuate. Even though the dendrites are actually continuous structures, the silver grains with which they are decorated are not. Therefore, small "gaps" between nerve fibers seen in the confocal BSL images may not indicate a lack of continuity but only that the reflecting surface is tilted too steeply for the reflected light to reach the objective.

Golgi-stained Purkinje cells show strong contrast between the surface reflections from the silver-decorated cells and the weak scattering by the surrounding non-impregnated tissues. Golgi preparations are of interest primarily because the method stains only 1% to 5% of the neurons in the preparation (Barr and Kieman, 1988; Scheibel and Scheibel, 1970). This creates a clear image of the dendritic tree of a single neuron hundreds of micrometers in

[1] Something more likely to occur near the focus, where intensity is highest, a feature that gives the technique some z-resolution.

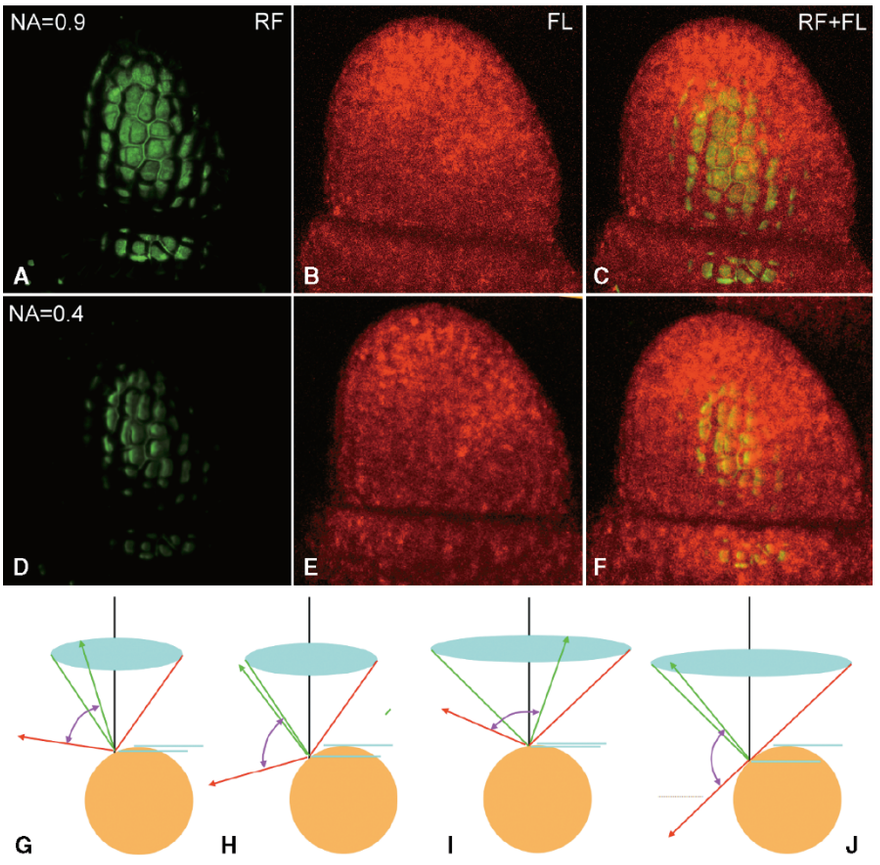

FIGURE 8.8. The effect of NA on the fraction of the light reflected from a sphere that is detected. A projection of confocal images made with reflected light (A) and autofluorescence (B), of the apical meristem of maize. (A–C) were made using an NA = 0.9 dry objective. (C) is a combined image. (D–F) The same, using an NA = 0.4 dry objective (magnification adjusted). Note that the region of detectable surface reflection is much smaller than that from which fluorescence can be detected and is lower with the low NA objective. (G–J) Diagrams that show how the NA and the height of the focus plane affects the fraction of a spherical surface from which reflected light can be collected by the objective lens (as defined by the red and green rays).

depth. If all the neurons stained, optical sectioning would be impossible because the high reflectivity would prevent light from penetrating much below the outer surface.

BSL images of living biological specimens present the same problems. Image contrast degrades as the objective lens focuses deeper into the tissue. Interfacial reflections from the various cellular components increasingly degrade the beam as it passes through more overlying cells. In addition, the deeper the microscope is focused into the specimen, the more heterogeneous the "medium" between the focal plane and the objective becomes, and the more that refraction produced by these inhomogeneities degrades the optical performance of the microscope. Figure 8.9 shows a BSL image of part of an amoebic pseudopod. The surface of the pseudopod, the mitochondria, vacuoles, and a number of other organelles and cytoplasmic crystals produce significant BSL. Chen and Cheng (1989) used the BSL mode to image the macronuclei of *Stentor coeruleus*.

Although the low reflectance of many living animal specimens makes is possible to see some distance into them, the low signal level that results complicates real-time BSL imaging of moving specimens. However, in plant cells, the interface reflections may be so strong that they bend the beam and produce "doubled" images in extended-focus (projection) views. This deflected illumination beam can also excite fluorophores to produce spurious fluorescent signals (Fig. 8.10, arrows).

When two reflective surfaces are in close proximity, interference fringes can occur. Although these fringes may be useful for measuring height, they also complicate image interpretation. Interference contrast can be used to study focal contacts (regions of close contact between the cell membrane with supporting substratum) in cultured animal cells. Figure 8.11 shows the interference fringes generated by the opposing surfaces of the plasma membrane of an amoeba and the cover glass.

In the materials sciences, Shinozald and colleagues (1991) used such interference fringes to study the delamination of a Cu thin film from an underlying polyimide substratum during a mechanical tensile test. This technique can also be used for detecting adhesion of transparent materials to the underlying support matrix. Figure 8.12 shows the delamination of a polyethylene film from glass in a micro-indenter test. Local detachment of the film from the underlying glass substratum results in pronounced interference fringes.

Figure 8.13 shows the surface of an ancient rice grain imaged by BSL confocal microscopy. The specimen is an artifact from an archeological site in southern Taiwan and contains mainly the carbonized skeleton of the endosperm. No trace of DNA was detectable in the grain. The double image of the surface actually represents separate images of the top and bottom surfaces of the cell wall (Fig. 8.13, *xz*- and *yz*-images). When imaging the interface of a dense block in a transparent medium, as shown in Figure 8.14, edge effects become prevalent. The vertical edge can be imaged in great depth but not the internal structures of the dense block. Figure 8.14(B) shows both the fluorescent and BS images of the edge of a maize stem (cross-section) mounted in water.

In disk-scanning confocal microscopes that utilize single-sided scanning, image contrast is reduced if light reflected by the disk surface is inadequately trapped. This increase in background signal level is particularly serious when the reflectance of the specimen is low. On-axis reflections of coherent light from optical surfaces are a serious problem when using a confocal microscope in the

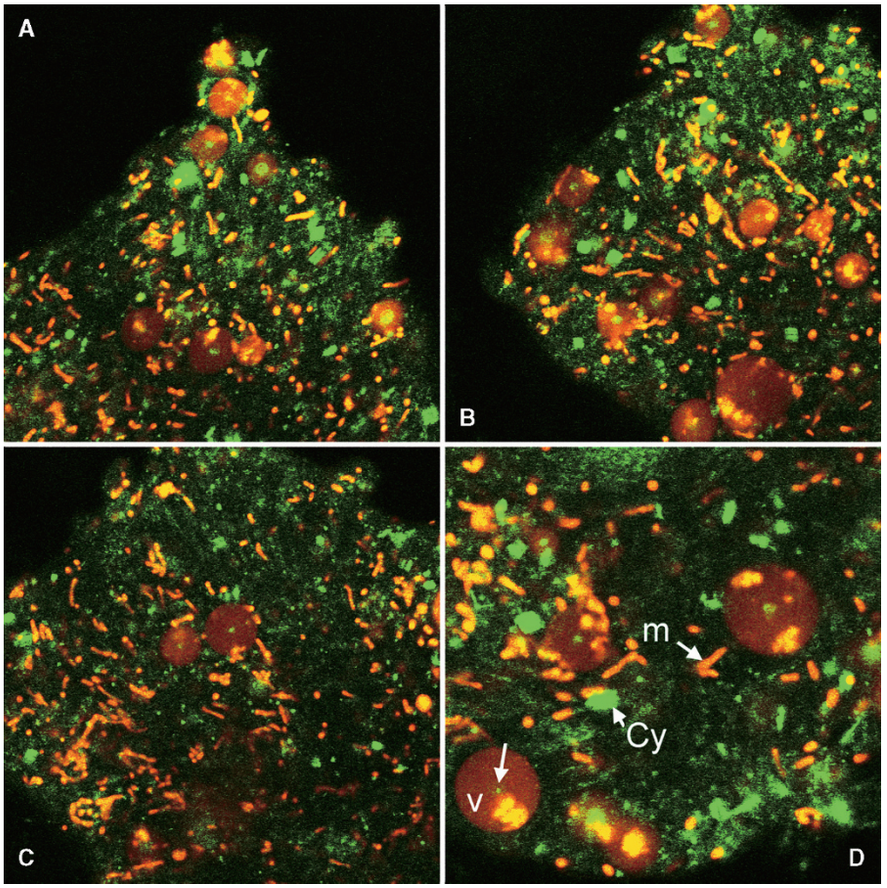

FIGURE 8.9. Two-channel confocal images of the pseudopod of an amoeba (*Chaos carolinense*) showing mitochrondria (m) and vacuoles in red fluorescence and backscattered light in green. The large, highly reflective structures are crystals (Cy) in the cytoplasm. A central scattering "core" (*arrow*) can be found in the spherical vacuoles (for an explanation, please see Fig. 8.19). (Images by Y. Deng, Z. Almshergi, and P.C. Cheng, Departments of Physiology and Biological Sciences, National University of Singapore.)

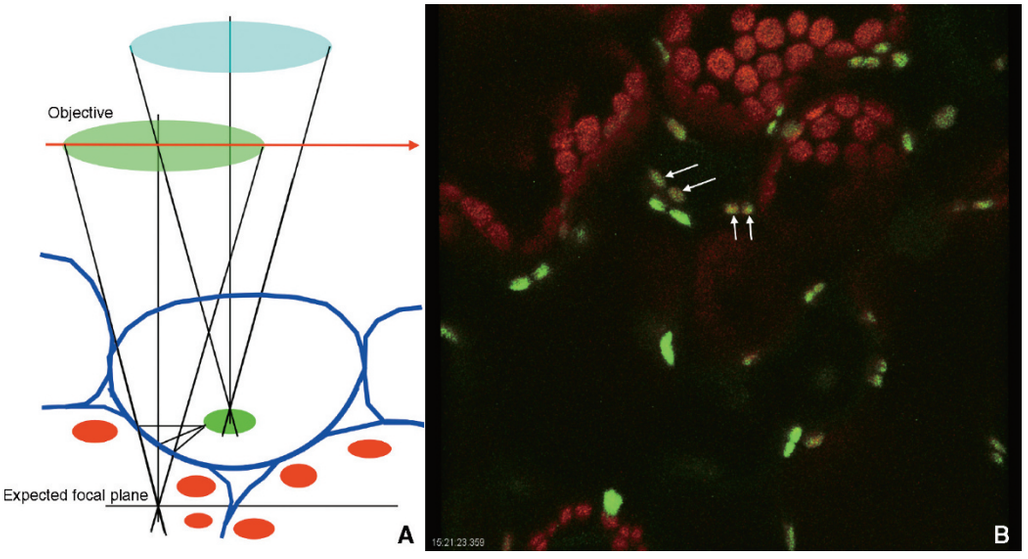

FIGURE 8.10. (A) Diagram of a possible situation that can generate a double image from a fluorescent organelle. In certain botanical specimens, the cytoplasm–cell membrane (cell wall) interface acts as an efficient reflective mirror, producing paired, mirror images of bright structures in an optical slice. In some cases, the position of the imaged organelle may be very different from the expected focal plane. (B) An extended focus (projection) view of an *A. thaliana* leaf. Note the double-imaged GFP organelles in the epidermal cells. The chloroplast-containing cells are mesophyll cells, situated below. (Image *courtesy of M. and D'A Weis, Agriculture Canada Laboratory, Summerland, BC.)

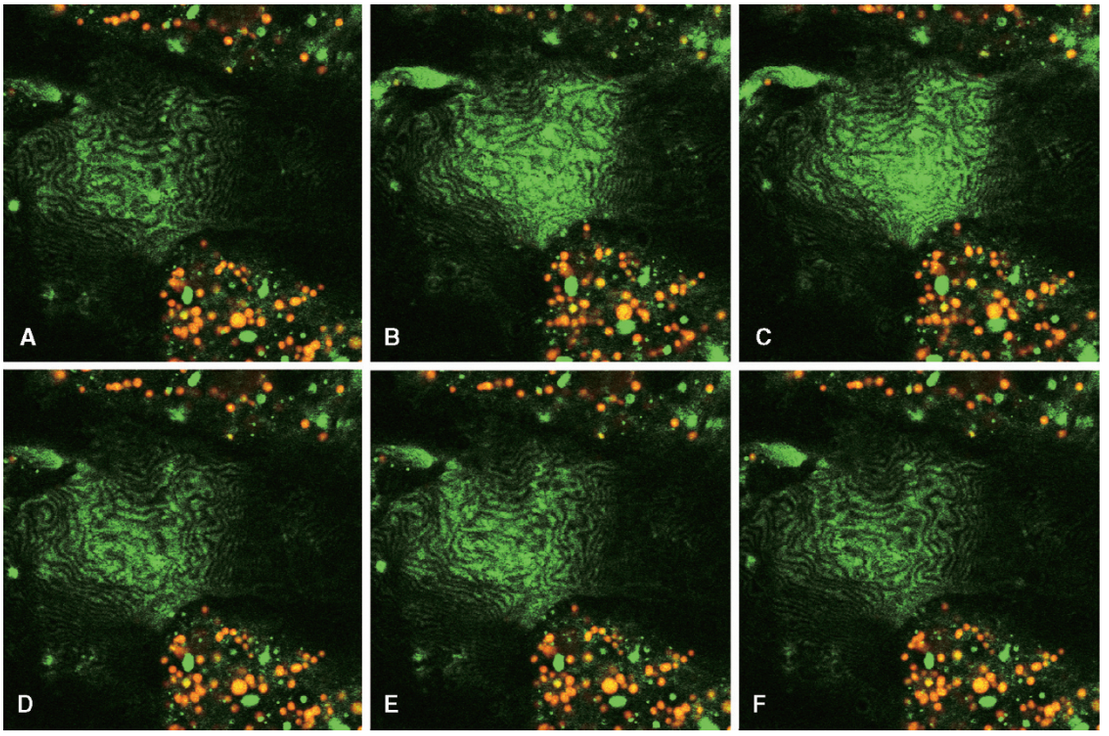

FIGURE 8.11. The separation between the plasma membrane of an amoeba and the coverslip can be monitored by the interference patterns generated by light reflected from these two surfaces. (A–F) time series showing movement of the plasma membrane. (*Green*, reflected/backscattered light; *red*, Mitotracker fluorescence.)

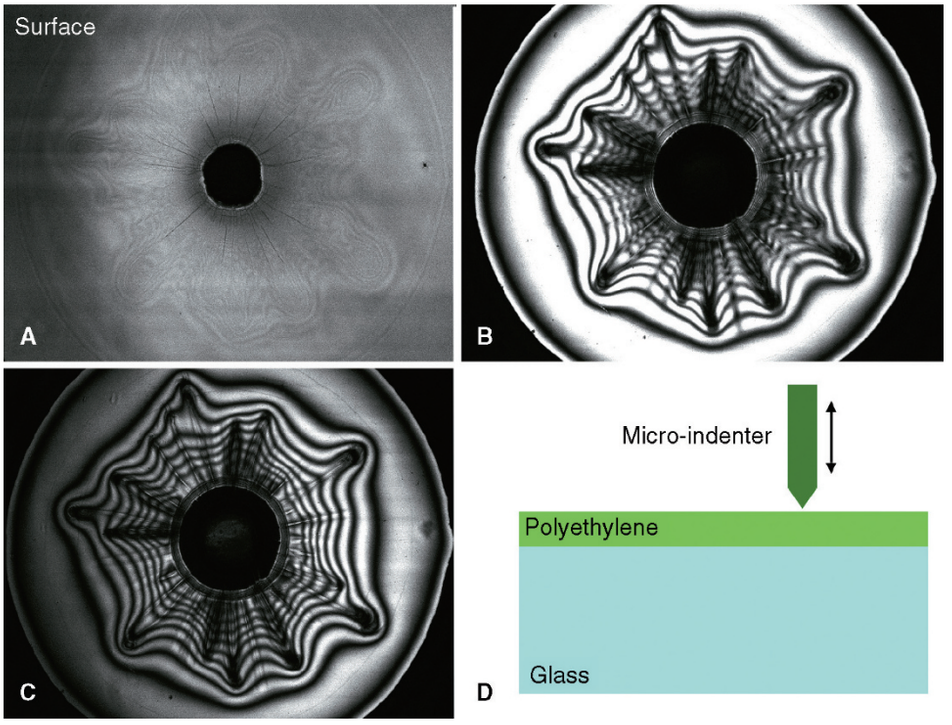

FIGURE 8.12. Delamination of plastic film from its substrate can be imaged by reflective confocal microscopy. (A) Focused near the surface of the polyethylene film, (B) and (C) focused near the plastic–glass interface. The interference patterns provide a good measure of the gap resulting from delamination. (D) Diagram of the experimental setup. A micro-indenter was used to deform the plastic, causing delamination. (Specimen courtesy of D.M. Shinozaki, Department of Mechanical Engineering, University of Western Ontario, London, Canada.)

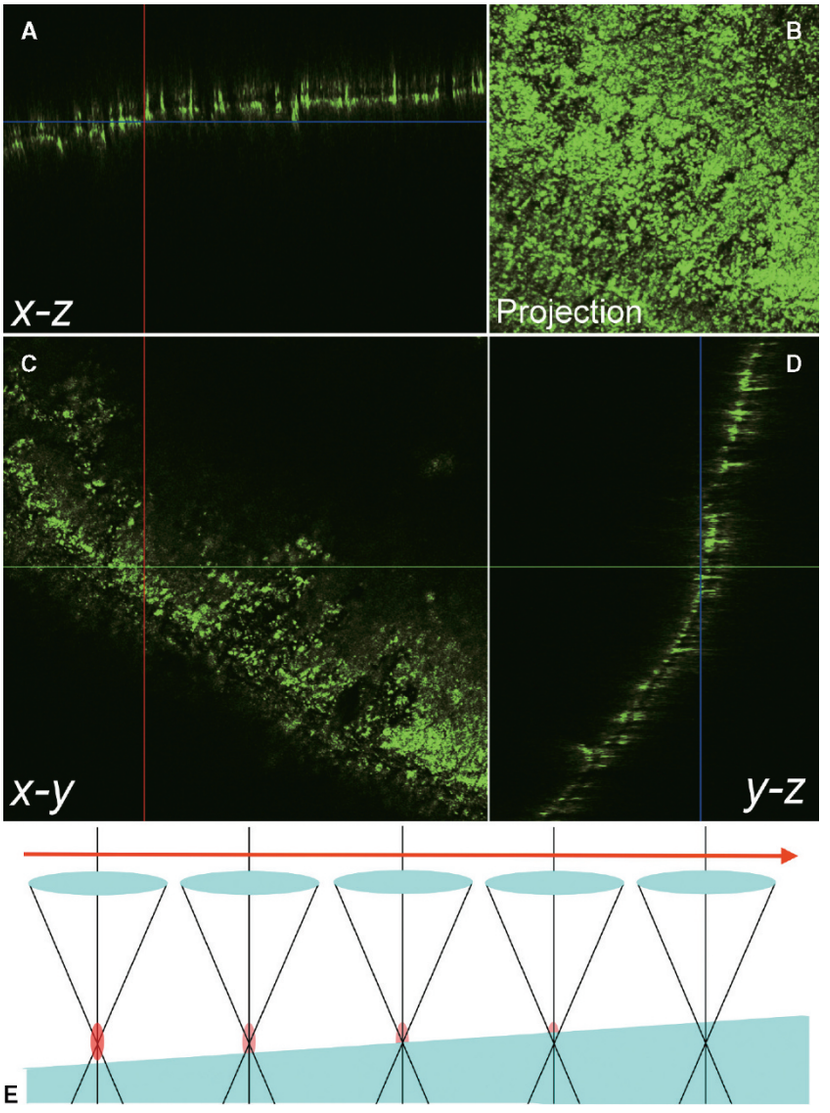

FIGURE 8.13. The surface of an ancient rice grain imaged by BSL confocal microscopy. The specimen is an artifact from a southern Taiwan archeological site and contains mainly the carbonized skeleton of the endosperm. (A) *xz* view, (B) extended focus view (projection view), (C) *xy* optical section, (D) *yz* view. Note the double-line in the *xz* and *yz* image. (E) Diagrammatic representation of the imaging condition. (Specimen kindly provided by Yue-Ie Caroline Hsing, Institute of Plant and Microbial Biology, Academia Sinica, Taipei, Taiwan.)

BSL mode. The result is a bright spot or a series of diffraction fringes in the center of the image (see Fig. 8.42, discussed later). Although this artifact can be avoided by panning the scanned area away from the optical axis, this approach sacrifices the field of view and degrades the image by using off-axis portions of the optical system in which the image is less well corrected (see Chapter 11, *this volume*).

In the single-sided confocal microscopes constructed by Kino (Xiao *et al.*, 1988) and by us (Cheng *et al.*, 1989), the light reflected from the surface of the spinning disk and from optical surfaces is removed by using a Glan–Taylor-type polarizer to achieve high polarization extinction (10^{-5}) of the illuminating laser beam, and adding a 1/4-wavelength retardation plate to the optical path just above the objective to convert the linearly polarized illuminating beam to circularly polarized light. With an analyzer placed just in front of the detector, this arrangement removes most unwanted reflections although there is still a small amount of reflection from the front surface of the objective lens.

Of greater concern is the fact that on-axis reflections from optical elements, or from the surface of the coverslip or the slide, can interrupt mode-locked operation of ultrafast lasers. This situation can be avoided by inserting a Faraday rotator and 1/4-wave plate into the illumination beam to prevent the reflected beam from re-entering the laser cavity (see also the discussion of Antiflex techniques in Figs. 2.7 and 10.5, *this volume*).

Phase Contrast

Because the human eye [or the charge-coupled device (CCD) camera] is sensitive only to changes in amplitude, phase variations produced by the specimen must be converted by the optical system into amplitude variations for them to become visible. For example, phase contrast and differential interference contrast (DIC) convert specimen-induced phase shifts of the illuminating light into amplitude contrast at the final image plane. Most biological specimens are 3D phase objects consisting of many compartments, each with a different RI. Apart from generating contrast, these structures also distort and shift the wavefront of the illuminating beam, resulting in complex interference patterns. Both phase and DIC are frequently used in conjunction with confocal microscopy to obtain the general morphology of the specimen. Because DIC has good *z* resolution, 3D digital image restoration of DIC image stacks is now commercially available (AutoQuant, Troy, NY; see also Chapters 2 and 24, *this volume*).

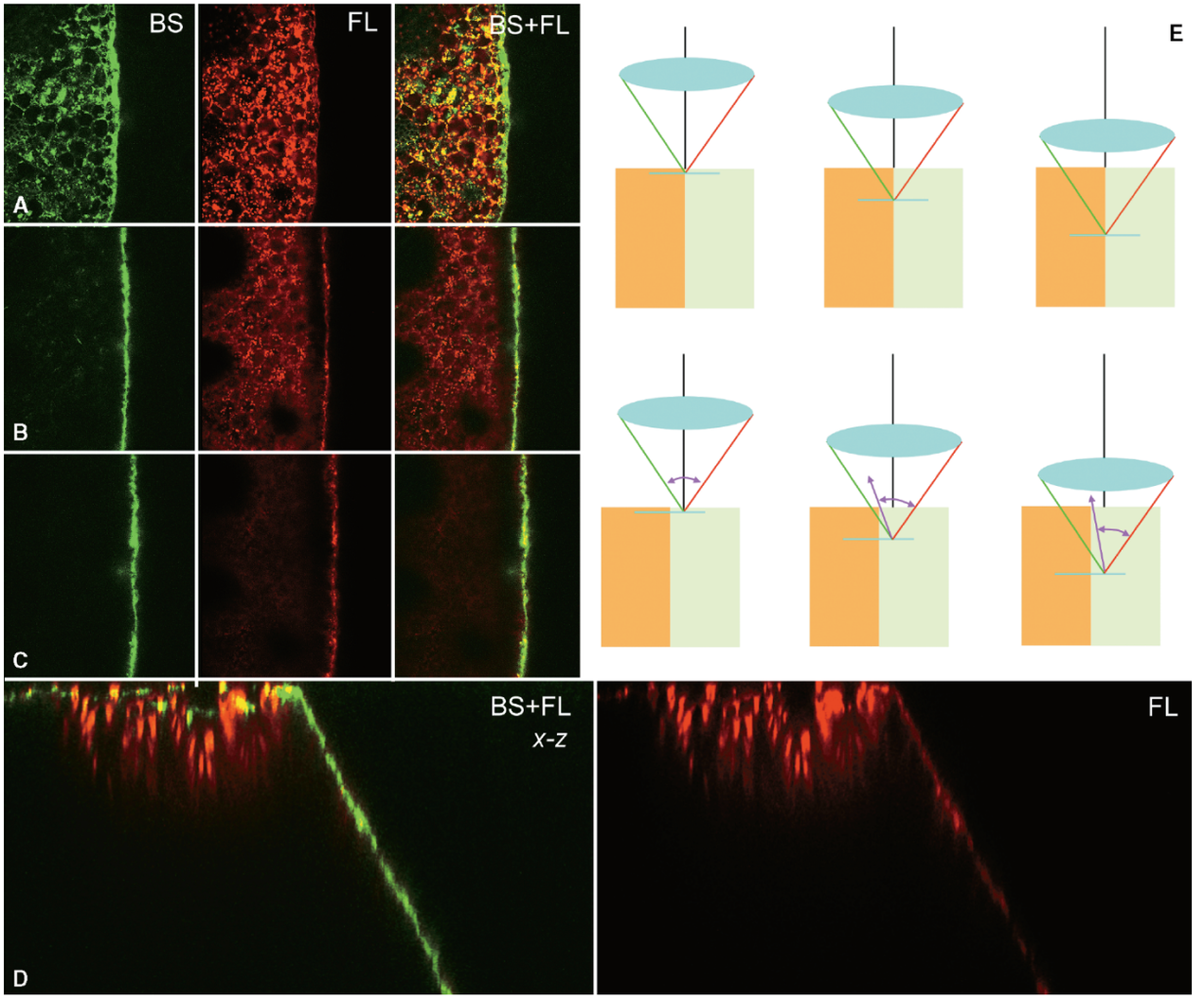

FIGURE 8.14. Edge effect. (A, B, C) Optical cross-sections (*xy*) of the edge of a maize stem at various depths. (D) *xz* section of the image stack showing the highlighted edge. Green, BS; red, autofluorescence (FL). (E) Diagram of the imaging situation. (Note the edge of the maize stem is actually tilted with respect to the optical axis although the diagram shows a vertical edge.)

Fluorescence Contrast

When one images emission signals, such as those produced by fluorescence microscopy, for a given ΔI, one can increase the contrast by lowering $\bar{I}$. In a typical epi-fluorescence microscopy, the background intensity from scattered illuminating light is removed by the dichroic beam-splitter and the barrier filter (see Chapter 3, *this volume*). In the absence of diffuse staining, this darkfield optical system produces a very low $\bar{I}$. This increases the contrast between the background and very weakly fluorescing structures, a feature that has ensured the popularity of this technique for the past 40 years.

The factors affecting the detectability of fluorescence from a voxel are the intensity of incident radiation, the intensity of the fluorescence (itself a function of the concentration of the fluorochrome, its absorption cross-section and its quantum yield (QY) at a given excitation wavelength), self-absorption within the voxel and between the voxel and objective, and the effective NA of the objective. Additional background signal may reach the detector because of imperfections in the dichroic elements and overlap between the absorption and emission spectra of the dyes involved (see Chapter 36, *this volume*).

In multi-photon fluorescence microscopy, the axial and transverse-contrast is the result of the 3D energy gradient at the focal point, the concentration and nonlinear QY of fluorophores, and background signal level under multi-photon excitation. Readers are kindly referred to Chapters 16, 28, and 40 for a detailed discussion of fluorescence imaging.

Because of its exquisite sensitivity and specificity, fluorescence microscopy is an extremely important tool in the biological sciences. In widefield fluorescence microscopy, the detected image data includes signal from both in-focus and out-of-focus subvolumes. This often produces an image that has excessive haze and lacks contrast. As this haze or flare is proportional to the thickness and stain density of the specimen, conventional, widefield epi-fluorescence works best when imaging thin specimens such as tissue culture cells. In confocal imaging, the signals from out-of-focus features are almost completely removed, resulting in an image with exceptionally high contrast (Fig. 8.15; Wijaendts van Resandt *et al.*, 1984; White *et al.*, 1987, Sheppard, 1993). In addition, modern

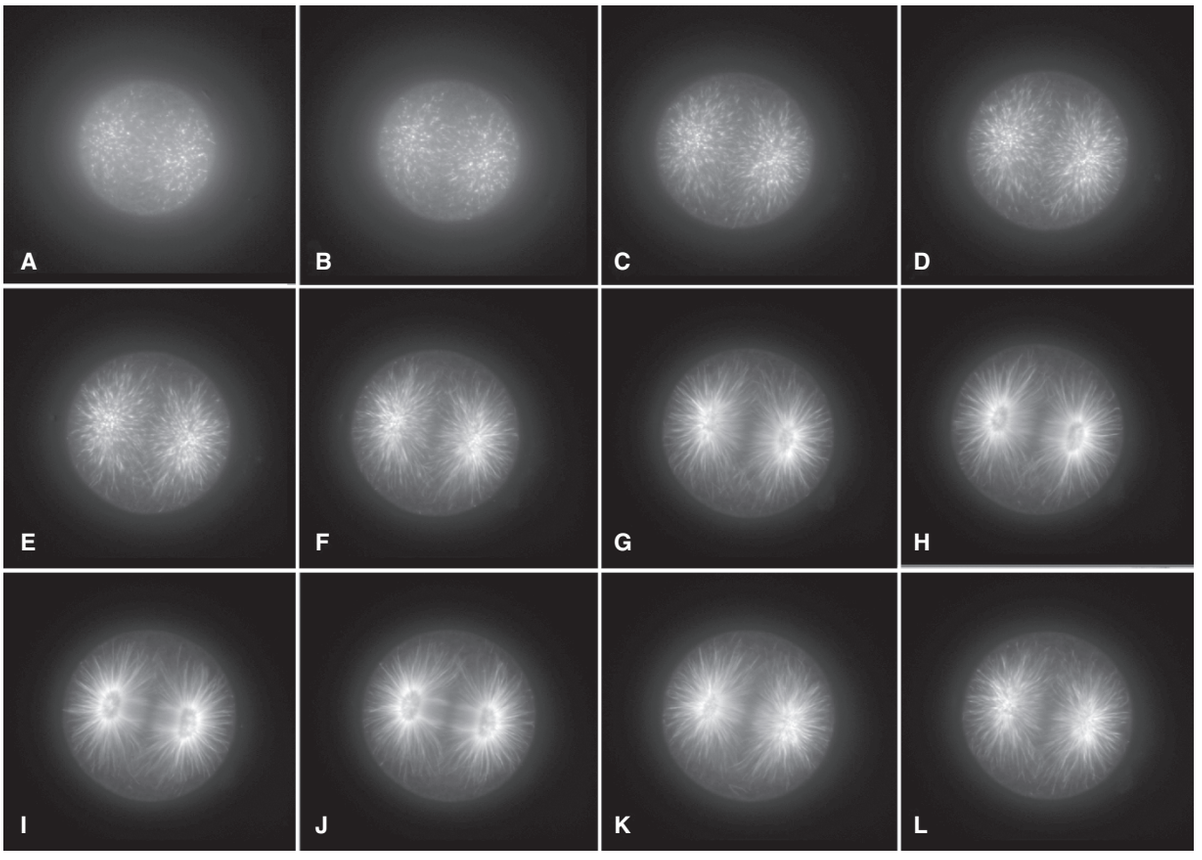

FIGURE 8.15. Series of confocal optical sections of the first mitotic division of a sea urchin embryo in which the microtubules have been labeled with a fluorescent dye.

3D image processing and restoration can further improve the S/N and contrast parameters of the image (see Fig. 8.40 in the Deconvolution section below).

Contrast Related to Excitation Wavelength Change

Biological specimens often naturally contain a large number of fluorescent molecules that produce autofluorescence. Because each fluorescent species has a unique absorption and emission spectra as well as a set QY, the total autofluorescence spectrum can vary with the excitation wavelength. Figure 21.13 shows the changes in the fluorescence spectra obtained from *Canna*, produced by using different excitation wavelengths from 350 nm to 514 nm. Figure 8.16 demonstrates this effect on the root tip of *Arabidopsis thaliana*. Although the signal levels are normalized in the 515 nm detection window, the fluorescence excited at 477 nm (yellow label) produces far less signal longer than 547 nm than does that excited using either 458 nm or 488 nm. The false-color images in Figure 8.16 clearly demonstrate the differences in signal level when the root tip is excited by various wavelengths.

When attempting to detect an exogenous fluorophore, one can often reduce the background level by picking exactly the right excitation wavelength. Therefore, to determine the optimal excitation and emission bandwidths, one must know the excitation spectrum of both the background autofluorescence and the tagged fluorescent probe(s). Figure 8.17 shows how images obtained in different emission bands can vary in appearance and contrast. The emission spectrum shown in Figure 8.16 indicated the presence of BSL and fluorescence from GFP and chlorophylls (Chl). Figure 8.18 is an extended-focus fluorescence image of an alga showing how using different emission filters [green bandpass (G) and red longpass (R)] changes the appearance of a chloroplast.

Negative Contrast

Small, isolated, non-fluorescent structures can be imaged with fluorescence confocal microscopy by filling the surrounding medium with a fluorescent solution. This dye-excluding technique was originally used in the study of polyethylene crystallites in xylene and can also be used to outline small crystal deposits and the extracellular compartment in biological specimens. Because dextrans are relatively inert and exhibit low toxicity, they are ideal markers to probe either extracellular or intracellular compartments. In the material sciences, dye-filling techniques are frequently used to provide contrast when studying micro-cavities (Harridose *et al.*, 1991; Shinozaki *et al.*, 1991; Cheng and Kriete, 1995).

Negative contrast can also be used in a number of biological applications. Figure 8.19 shows that the vacuoles in cells of the peony flower petal are sufficiently autofluorescent to reveal cytoplasmic strands traversing them as dark threads penetrating this fluorescent sea. After acquisition, the fluorescence image can be inverted for 3D reconstruction.

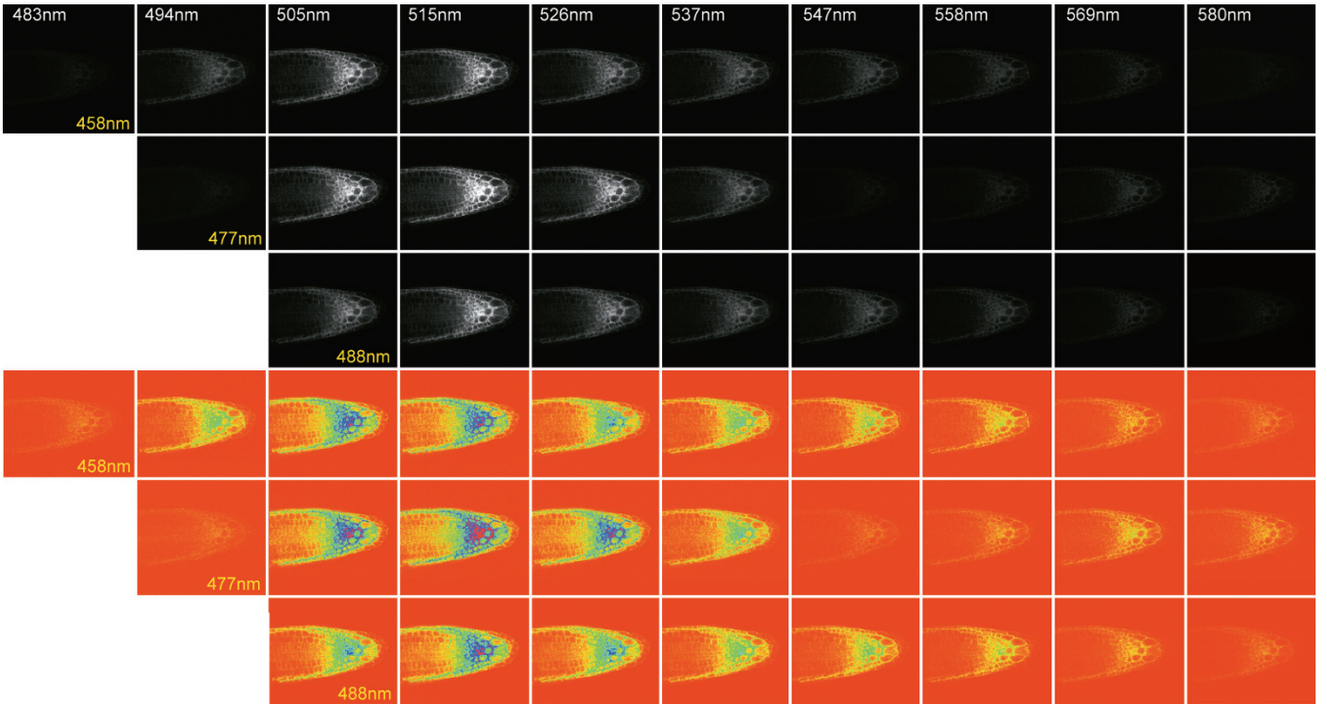

FIGURE 8.16. GFP in the root tip of *A. thaliana*, showing image contrast variation in response to different excitation wavelengths. For each excitation wavelength (*yellow labeling*) at 458 nm, 477 nm, and 488 nm, a series of spectral sections was obtained at 10 nm intervals using a Zeiss LSM510 Meta confocal microscope with the channel gain adjusted for normalized spectral response. The GFP emission peaks at 505 to 515 nm, and shows little variation between the three excitation wavelengths. However, the autofluorescence image (i.e., that at wavelengths >547 nm) shows significant variations at the different excitation wavelengths. The three color rows show the same images in false color to emphasize low-intensity signals. (Images obtained at the 2005 International Course on 3D Microscopy of Living Cells at the University of British Columbia, Vancouver, Canada.)

Figure 8.20(A) shows the fluorescence spectra (excited at different wavelengths) of a zebrafish expressing green fluorescent protein (GFP) and DsRed in its liver and pancreas. Using these spectra, we can understand the contrast and relative signal strength that will be produced when particular excitation wavelengths and filters are used. Figure 8.20(B) shows how the ratio of GFP signal to DsRed signal varies as a function of filter bandwidth. When the total fluorescence emission spectrum represents the sum of the overlapping spectra of a number of different types of fluorescent molecule (a situation typical of autofluorescence), the contrast may be improved by carefully selecting the excitation and detection wavelengths and bandwidths. The differences in photobleaching dynamics among different fluorophores may cause the contrast between two channels to vary during the course of a time-series image stack. Figure 8.21(A) shows the photobleaching spectra of a zebrafish expressing GFP (512 nm) and autofluorescence. In this case, both GFP and the autofluorescent species in the sample exhibit similar bleaching dynamics, resulting in a nearly constant intensity ratio (contrast) over the time course of the study [Fig. 8.21(B)]. Figure 8.22 shows an extended focus view of a zebrafish specimen showing green fluorescence from the pancreas and red fluorescence from the liver. In Figure 8.22(A) one can see that the liver is bisected into two lobes by the pigment cells [Fig. 8.22(B)]. This self-shadowing phenomenon is commonly observed in confocal optical sections [Fig. 8.22(C,D)].

Special Concerns in Ultraviolet and Near-Infrared Range Confocal Microscopy

A micrograph is a plot of the intensity of some signal versus position. Changes in this signal represent contrast. But what if there is an error in the position? If an optical system focuses two wavelengths from the same location on the object into two different locations in the image, then we have created some contrast that should not exist. This can happen if the optical system is not achromatic.

Although most objective lenses are properly corrected for chromatic errors in the visible spectrum, it is wise to check their performance (Fig. 8.23). Normally, the wavelength difference between the illumination and the detection only becomes a serious concern in epi-fluorescence confocal microscopy when one wavelength is outside the visible range. When the excitation wavelength is in the UV, one must use specially designed UV objective lenses that are both chromatically corrected and also transparent for both the excitation and emission wavelengths (Wells *et al.*, 1990; Cheng *et al.*, 1994). Similar conditions apply when detecting IR fluorescence.

The situation is a bit different in multi-photon fluorescence and harmonic generation microscopy where the fluorescence or harmonic signal intensity is proportional to the square of the illumination intensity. Assuming the fluorescence is not near saturation,

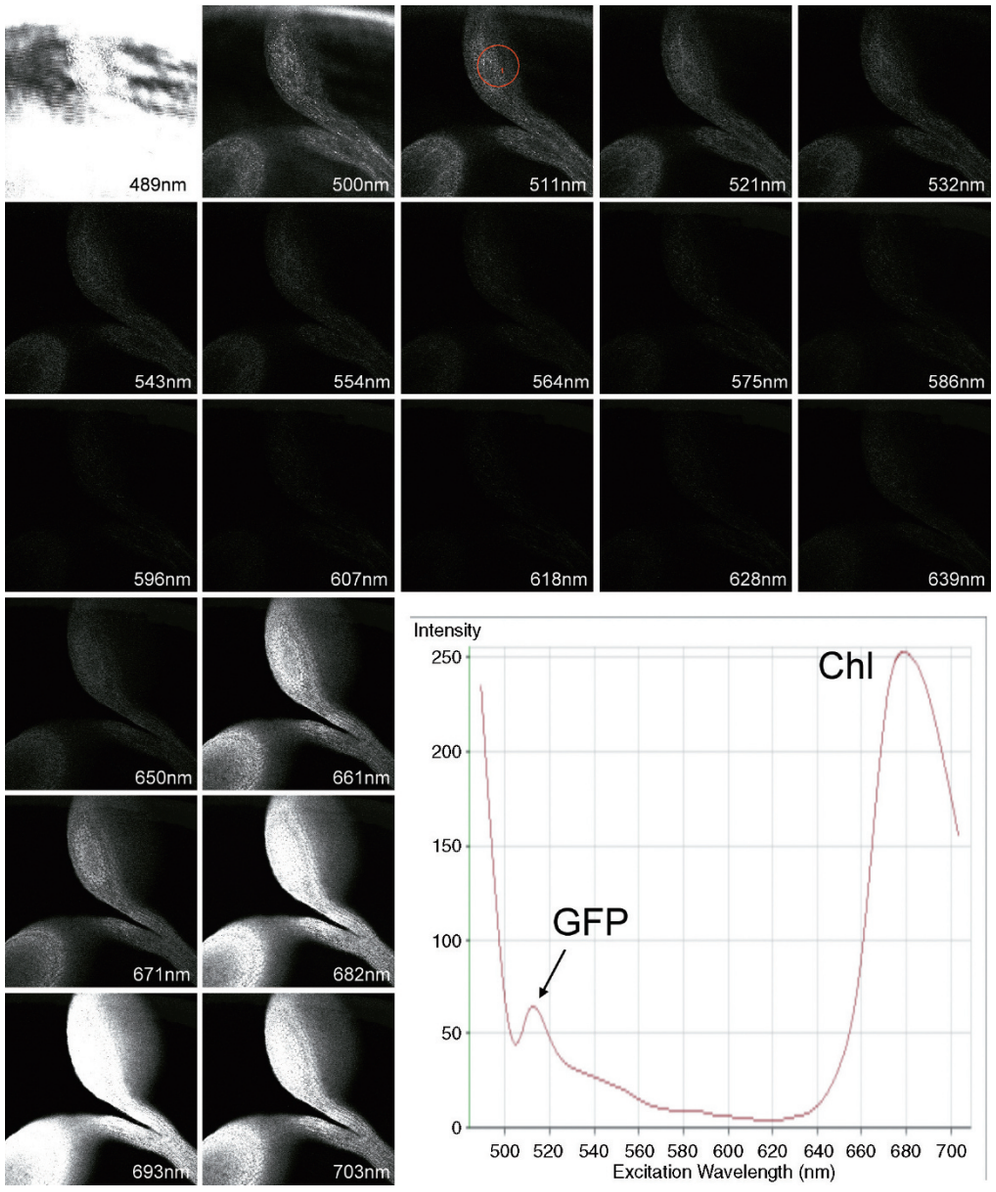

FIGURE 8.17. Spectral confocal image of a young seedling of *A. thaliana* showing GFP and autofluorescence from several chlorophylls. The specimen was excited at 488 nm. The spectrum was obtained from the circled region. The 489 nm image (saturated) represents reflections and scattering of the specimen and cover glass. Based on the spectrum, the 511 nm signal results from GFP while the other "green" fluorescence is the autofluorescence background. The image contrast for the chlorophyll autofluorescence depends on the wavelength of the detecting band (650 nm–703 nm). (Images obtained with a Zeiss 510 Meta. Specimen kindly provided by Shu-Hsing Wu, Institute of Plant and Microbial Biology, Academia Sinica, Taipei, Taiwan.)

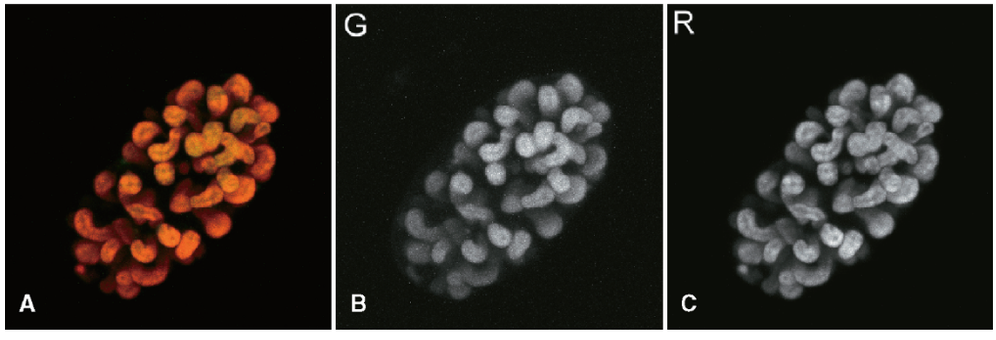

FIGURE 8.18. Autofluorescent image of the chloroplast of an alga. (A) Two-channel false-color image, (B) green channel (em: 540 nm bandpass), and (C) red channel (em: long-pass >600 nm). Note the difference in image contrast between (B) and (C).

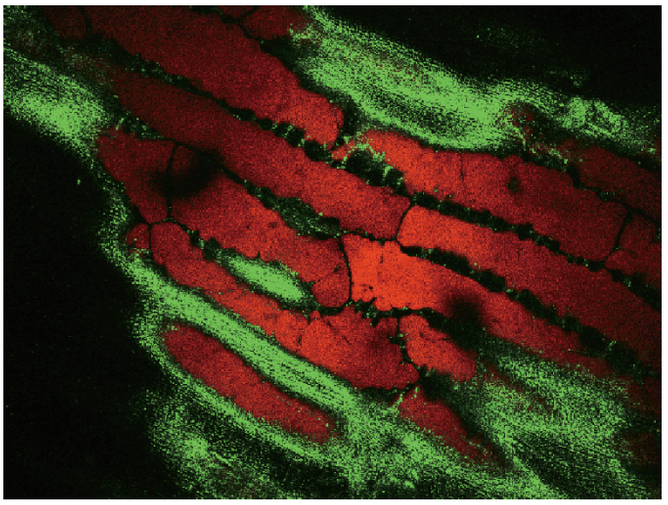

FIGURE 8.19. Two-channel confocal image of a peony petal. The strong autofluorescence of compounds in the vacuoles (*red*) allows one to image the fine (dark) cytoplasmic strands that traverse them, in negative contrast.

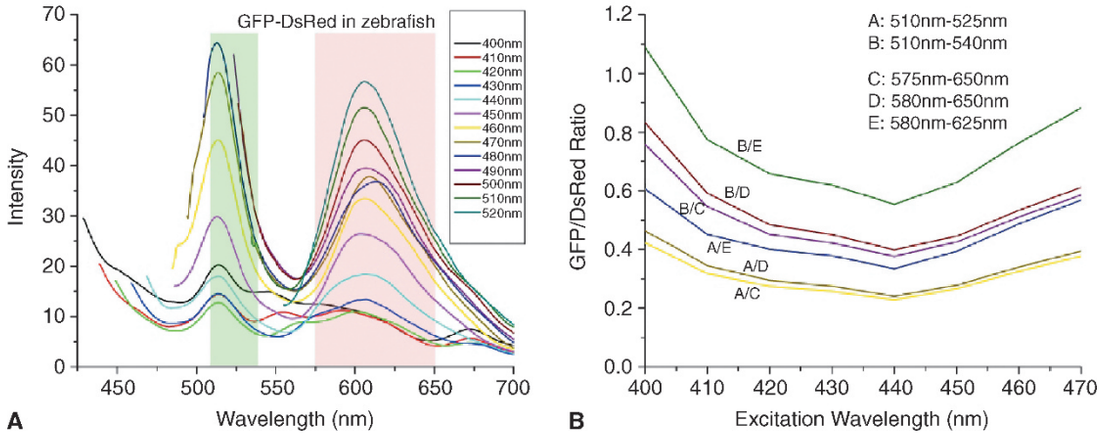

FIGURE 8.20. Emission spectra of GFP and DsRed in zebrafish (pancreas and liver, respectively) when excited at different wavelengths (ranging from 400 nm to 520 nm). Two hypotheical bandpass filters (green and pink bands) were used to separate the emission for imaging. In (B), the contrast ratio of these two channels are compared as a function of filter bandwidth.

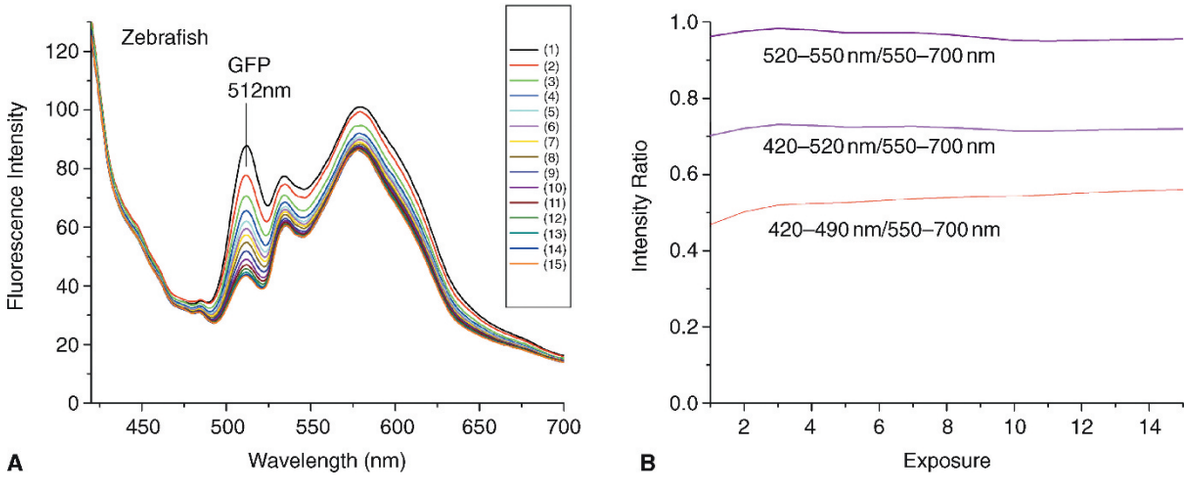

FIGURE 8.21. (A) Emission spectra of GFP (pancreas) and autofluorescence in zebrafish when excited using wavelengths from 400 nm to 520 nm. (B) Contrast ratios of the two channels when using filters having different passbands.

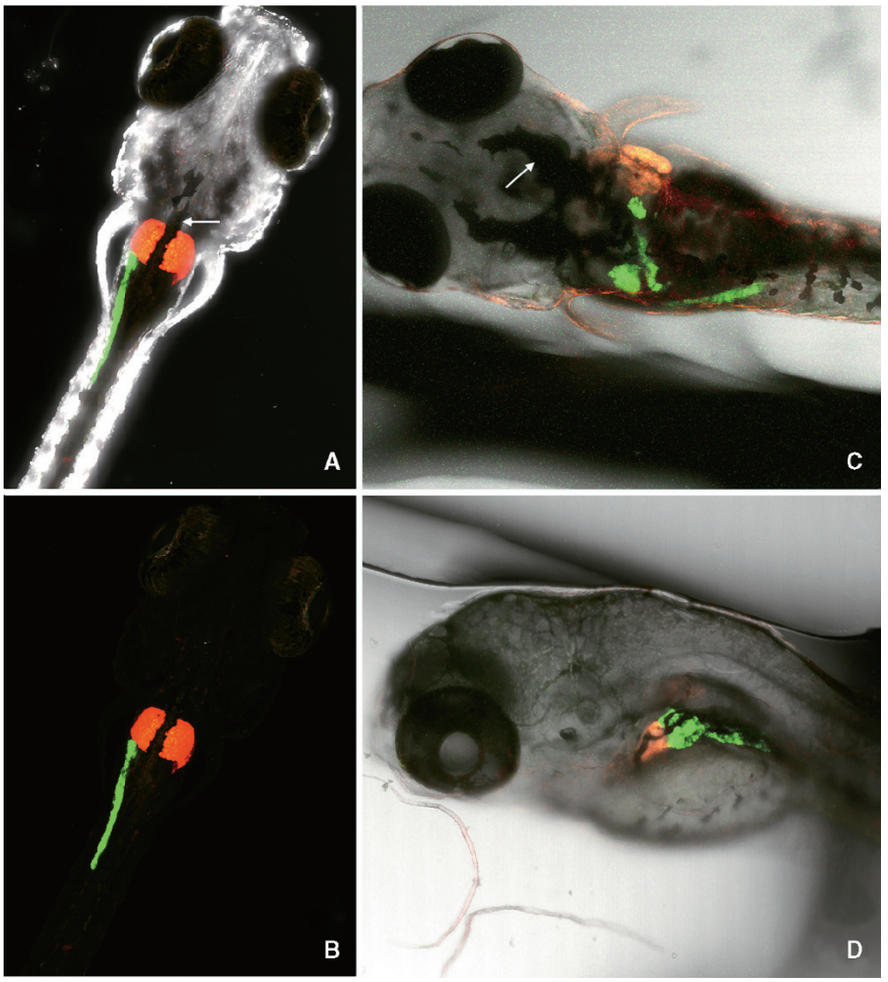

FIGURE 8.22. (A) Two-channel confocal projection images of zebrafish embryos, with a gray, non-confocal transmission image overlay, showing pancreas (GFP), liver (DsRed), and pigment cell (*arrow*). (B) The fluorescence images only. Note the liver is bisected into two lobes by the high absorption of the overlying pigment cells. (C) Embryo at a later stage, from above (D) imaging from the side can reduce the masking effect of the dorsally located pigment cells.

nonlinear signal generation is limited to the vicinity of the focal spot, and non-decanned detection can be used. In this case, chromatic correction from the excitation to the emission wavelength is superfluous because signal is only emitted from the focal region and therefore need not be focused. However, if one wishes to detect simultaneously several flurophores with large differences in QY, the fluorescence emission volume can be significantly different for each fluorophore.

If one uses a beam-scanning confocal unit with a detection pinhole to limit the size of the detection sub-volume, one must use an objective corrected for both the excitation and emission wavelengths but one can adjust the size and alignment of the pinholes for each detection channel to ensure that all signals are obtained from the same sub-volume. Such adjustments are particularly important in co-localization studies. Because the refractive index of the specimen (or medium) varies with wavelength, operation outside the waveband for which the objective is corrected can produce RI mismatches that can introduce spherical as well as chromatic aberration (Fig. 8.23).

Total Internal Reflection Contrast

The distance separating the flat surface of a glass plate (such as a coverslip) and a cellular structure having an RI higher than that of water and can be measured using total internal reflection microscopy (TIRM). Changes in this distance as small as 1 nm can be detected (Prieve and Walz, 1993). When a structure settles near a glass/water interface at which total internal reflection is occurring, some of the evanescent wave will be scattered by the structure, as diagrammed in Figure 8.24(A). This situation is called "frustrated" total internal reflection. Because of the non-uniform illumination of the water by the evanescent wave, the amount of light scattered by the structure is exquisitely sensitive to its proximity to the interface. This has been exploited to delineate focal contacts between cells and their substrates (Paddock, 1989).

When a scattering object is illuminated by an evanescent wave, the intensity of scattered light is a measure of the separation distance. The penetration depth (β^{-1}) of the evanescent wave is:

$$\beta = \frac{4\pi}{\lambda}\sqrt{(n_1 \sin\theta_i)^2 - n_2^2}$$

where λ is the wavelength of the incident light, η_1 and η_2 are the RIs of the coverslip and the fluid containing the particle, and θ_i is the angle of incidence of the illumination in the plate. The intensity of the light scattered by the cell, I, decays with the intensity of the evanescent wave. The scattered intensity $I(x)$ varies with the separation, x, as:

$$I(x) \approx I_0 e^{-\beta x}$$

Typically β^{-1} is about 100 nm when a glass coverslip is used as the "plate" and water is used for the bathing medium of a cellular "particle," having an RI of from 1.4 to 1.5 (proteins and lipids). Because of the exponential relationship, a very small change in x produces a measurable change in intensity. In a typical

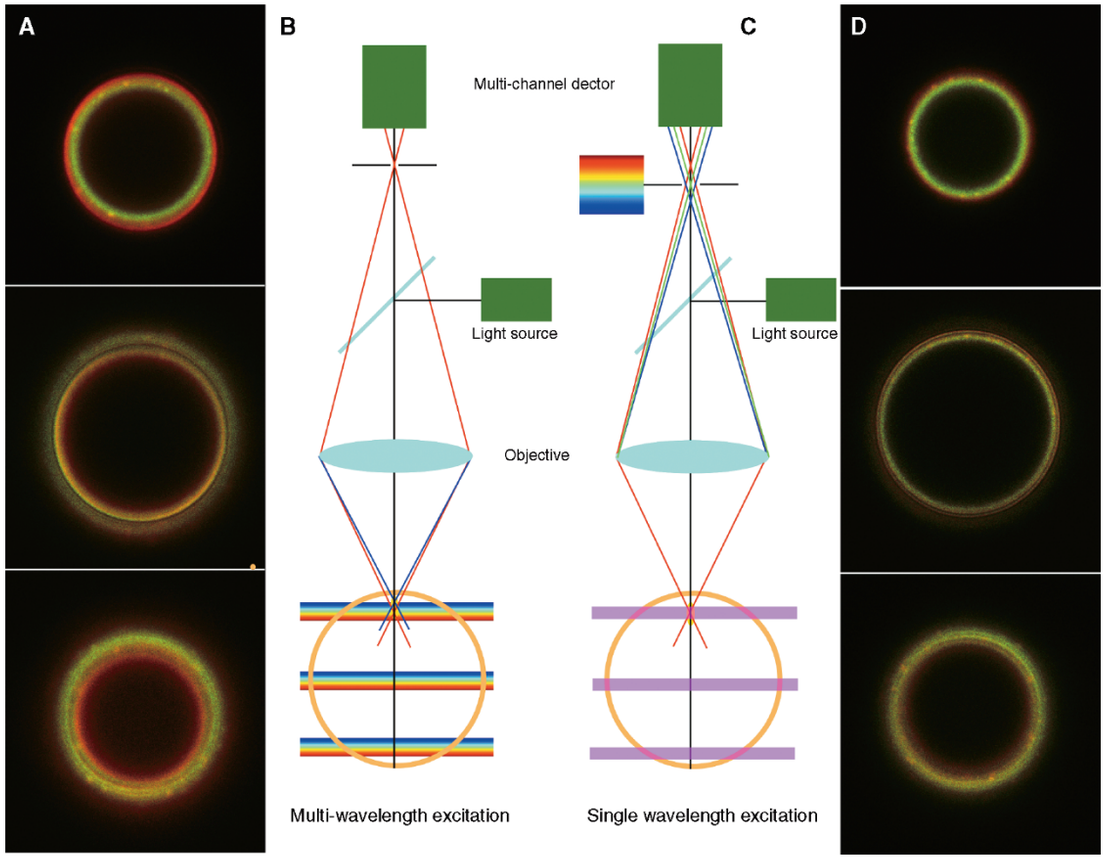

FIGURE 8.23. Chromatic aberration. (A) Optical sections of a latex bead with its shell labeled with fluorescent dyes (Tetra-spec, Molecular Probes). The image was obtained with two excitation wavelengths and recorded in two fluorescent channels. The separation of the "rings" in the images made at the three excitation wavelengths demonstrates that chromatic aberration is present. Note that, at the northern hemisphere, the red ring is outside the green ring, but that the order changes in the southern hemisphere. Although there is also significant chromatic separation at the equator, it is difficult to visualize in a single optical section because the aberrated rings are all about the same size. (B) Diagram of the imaging situation for (A). If only one excitation wavelength is used (C). Chromatic aberration primarily produces only misfocus at the detecting pinhole, resulting in signal loss of the "out-of-focus" rays. (D) The resulting images show less co-localization error. (Images obtained on a Leica confocal microscope with objective lens corrector collar intentionally set wrongly. M. Weis and P.C. Cheng, Agriculture Canada, Summerland, British Columbia, Canada, and State University of New York at Buffalo.)

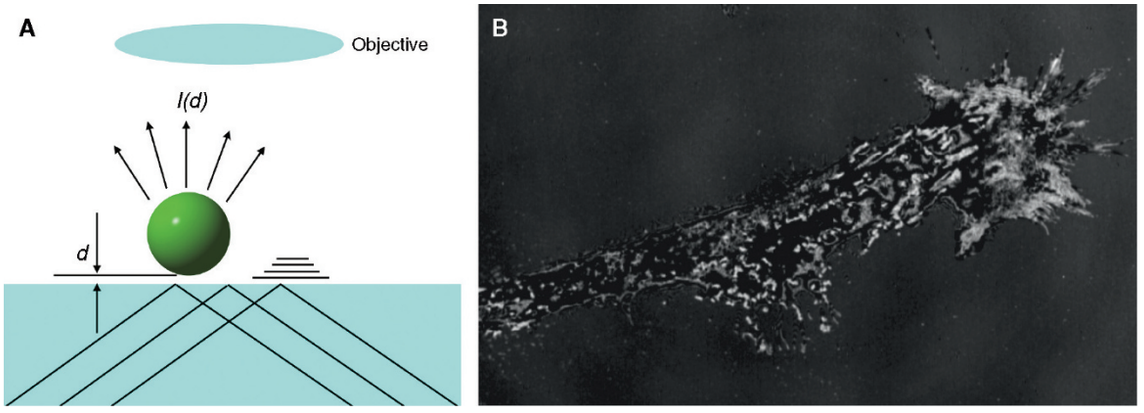

FIGURE 8.24. Total internal reflection microscopy (TIRM). (A) An evanescent wave generated at the glass/water surface can be scattered by particles near the surface. The scattering intensity I_d is a function of the distance between the surface and the particle. (B) TIRM image of a tissue-culture cell adhered to a coverslip.

biological imaging setup, $\eta_1 = 1.5$ (glass slide), and $\eta_2 = 1.33$ for the aqueous solution bathing the cell, a 1% change in signal intensity represents a 1 nm change in distance (x). It is important to note that the equation for $I(x)$ holds for all separations including the contact situation ($x = 0$). Figure 8.24(B) shows a TIRM image of a tissue-culture cell attached to a glass coverslip surface. The image intensity is a function of the separation between the cell membrane and the coverglass. Although interpreting TIRM images obtained from 3D scattering objects is often difficult (Van Labeke *et al.*, 1995; Carminati and Greffet, 1995a,b), recently, Carney and Schotland (2001) derived a theoretical foundation for three-dimensional TIRM.

Harmonic Generation Contrast

Recently, a number of new imaging modalities based on nonlinear optical phenomena have been developed (Cheng *et al*., 2001, 2002, 2003; Chu *et al*., 2001, 2003; Cheng *et al*., 2002). From the power series equation above, one can see that the second- and third-order nonlinear susceptibility, $\chi(2)$ and $\chi(3)$ (respectively) determine the contrast formation mechanism in nonlinear microscopy. Second harmonic generation can be considered to be an interaction involving the exchange of photons between the various frequency components of the electromagnetic field. In SHG, two photons of frequency ω are destroyed and, simultaneously, one photon of frequency 2ω (exactly) is created in a single, quantum mechanical process. As SHG is sensitive to the relative orientation between the polarization of the incident light and the symmetry condition of the material, the SHG signal can be used to provide information about crystal orientation and perfection, molecular structure, and regions where the centro-symmetry breaks down, such as surfaces and optical interfaces. It can also be induced either by structures that are organized on the sub-micron level or by a large, local residual electric field (e.g., a membrane potential).

Third harmonic generation involves three photons of frequency ω that are destroyed to create one photon of frequency 3ω. A nonlinear contribution to the polarization at the frequency of the incident field leads to a nonlinear contribution to the RI experienced by a wave at frequency ω. This is known as the Kerr effect.

Barad demonstrated that imaging with the third harmonic is possible and is especially suitable for imaging structures in transparent specimens with low intrinsic contrast. It is sensitive to changes in the nonlinear optical properties of the specimen such as interfaces between media of differing RI (Barad *et al.*, 1997).

Because harmonic generation and the Kerr effect involve only virtual state transitions that are related to the imaginary part of the nonlinear susceptibilities, no energy is deposited in the specimen and no damage can be produced. However, interactions involving real-level transitions, such as multi-photon absorption (that may lead to the generation of fluorescence, 2PF) do involve energy deposition and can induce photochemical responses such as photodamage or photo-induced polymerization. It is important to point out that both nonlinear absorption (fluorescence) and harmonic generation can occur simultaneously in the same specimen. Figure 8.25 shows a section of a maize leaf just below the epidermal cell using different excitation polarizations (THG, blue; SHG, green;

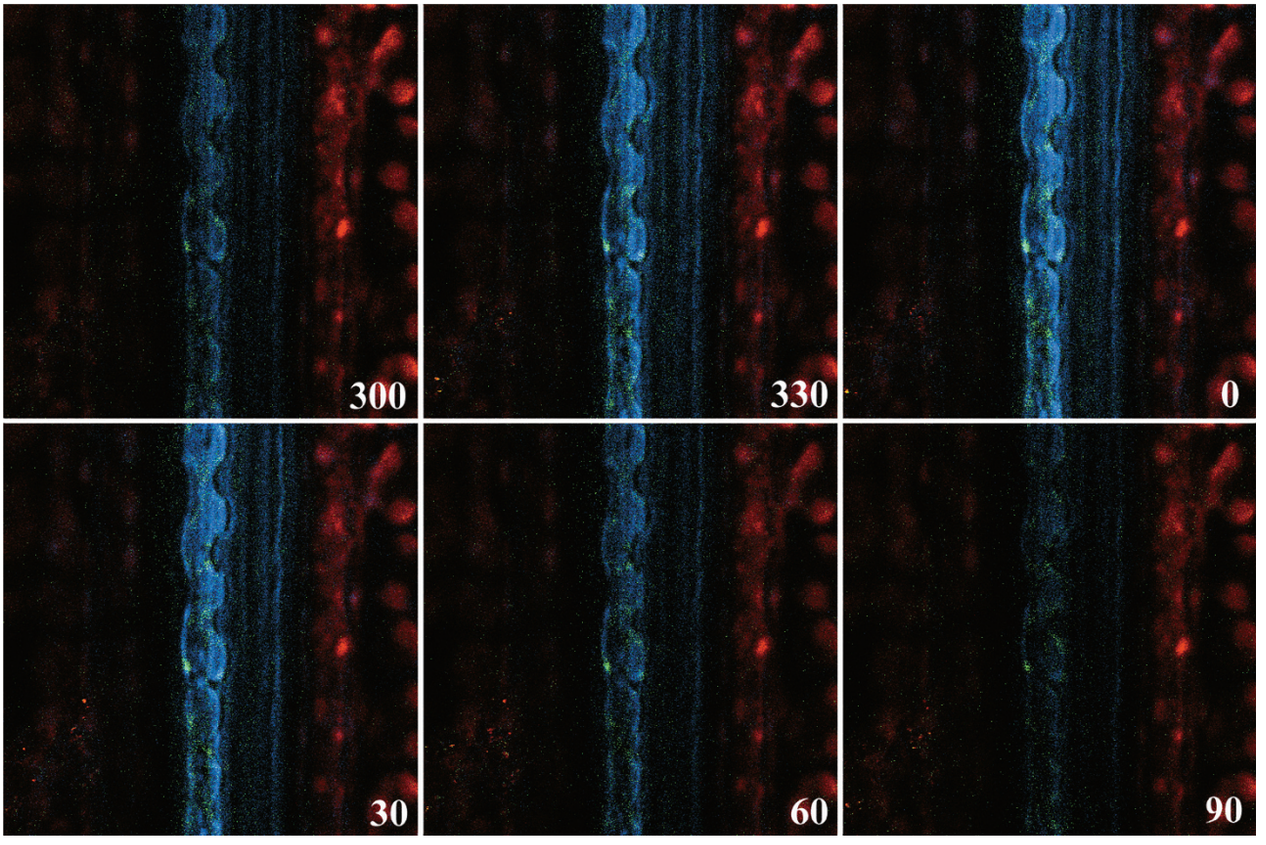

FIGURE 8.25. Nonlinear optical section of a maize leaf just below the epidermal cells at different illumination polarization (330°–90°). Note that, although there are few changes in two-photon fluorescence (red), there are significant changes in the THG signal intensity (blue). The optical section was obtained just tangential to the lower surface of silica cells, therefore, only high THG is observed from the interface. Very weak SHG (green) is detected from the silica cell at this optical section.

2PF, red). For a detailed discussion of these topics, the reader is kindly referred to Chapters 38, 39, and 40.

GEOMETRIC CONTRAST

z-Contrast in Confocal Microscopy

One of the basic properties of the confocal microscope is its ability to use a confocal aperture to reject out-of-focus signal. Therefore, confocal images are acquired from a narrow slice of the specimen. This optical sectioning capability gives the basic optical contrast mechanism of the confocal microscope and is commonly referred to as the *z*-contrast (axial contrast).

One can use this contrast mechanism when examining integrated circuits with reflected light confocal microscopy (Fig. 8.26). Although some image contrast results from differences in surface reflectivity and/or roughness, most of the contrast between adjacent circuit structures is due to the variation in the height of the surface. The surface topography of such specimens can be obtained by plotting the maximum intensity profile from a confocal *z*-stack.

The tilt of structural surfaces within a specimen also affects the reflection signal strength (Fig. 8.27). If the surface tilt is so high that no light reflects directly into the objective, then this part of the surface appears dark (or absent) in the image while a surface perpendicular to the optical axis will give a maximum signal. This type of image contrast is highly dependent on the NA of the objective: high-NA objectives reduce the amount of "surface angle" contrast (Fig. 8.8). On the other hand, such contrast can be increased if the detector is placed not directly behind the pinhole but in the diffraction plane of an auxiliary lens focused on the pinhole plane. A four-segment detector in this position gives independent signals proportional to the four possible different surface tilt directions (Fig. 8.28). Figure 8.29 shows a series of optical sections (reflective, RL; backscattered, BS; fluorescence, FL) of a fluorescent latex bead in water. The surface curvature determined the signal strength of the reflective signal. The center reflective core (arrow) in the bead is an artifact due to a lensing effect. When imaging a specimen consisting high absorbance features, such as a cross-section through the vasculature bundle of plant stem, the "effective" NA of the objective lens is limited by the fact that the surrounding secondary wall obscures the high-NA rays, resulting in a "pipe effect" (Fig. 8.30). As a result, the transverse and axial resolution decreases as one images deeper into this part of the tissue.

The field curvature of the objective lens can create artificial *z*-contrast when imaging a flat specimen because the spherical focus plane intersects only a ring-like area of the flat surface (Cheng and Kriete, 1994).

Total Internal Refraction Fluorescence Contrast

A light beam, incident on an interface separating regions of different RI, will be totally reflected if the incident angle exceeds a critical angle, θ_c. While "all" the light is reflected in the classic sense, quantum mechanics requires that a portion of the radiation penetrates into the distal phase. This radiation is called the evanescent wave and its strength decays exponentially.

Therefore, if a fluorescent structure is located in the second medium near the interface, a fluorescence signal can be excited and detected from it. The signal level is determined by the exponential decay function of the evanescent wave and by the QY and concentration of the fluorophore. This process creates a very thin optical section near the RI interface. The fluorescence intensity I_F is:

$$I_F(x) = QY[con] \cdot I_0 e^{-\beta x}$$

where QY is the quantum yield of a fluorophore, $[con]$ is its concentration, I_0 is the incident light intensity, and x is the separation distance between the dye molecule and the RI interface.

Figure 8.30 shows that total internal refraction fluorescence contrast (TIRF) can be used for measuring the $[Ca^{++}]$ in the subcellular cleft using the Fluo-3/Fura Red ratiometric system [Fig. 8.31(A)]. The calcium image in Figure 8.31(B) is superimposed on a TIRM image that shows the contact points of the cell from Figure 8.24. Figure 8.32 shows the cortical microtubule assembly near to the coverslip in a Vero cell. Figure 8.33 shows the

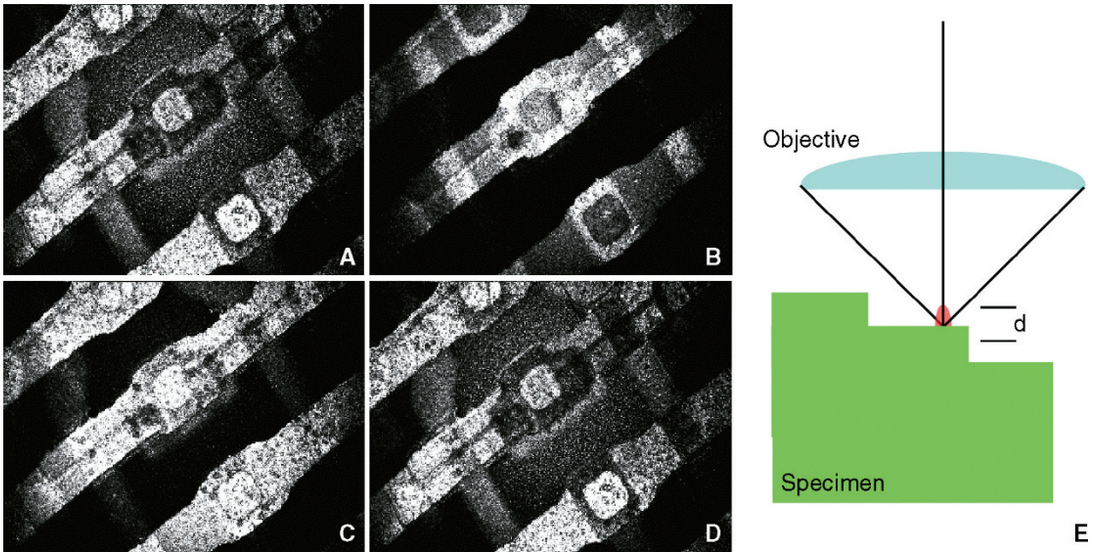

FIGURE 8.26. (A–D) Reflected-light confocal images of an integrated circuit at different focus levels. The image contrast is primarily the result of variations in the signal being focused through the pinhole between in-focus and out-of-focus structures. (E) Diagram representing confocal imaging of a stepped structure in which the steps are thicker than the thickness of the imaging plane (*shaded bar*).

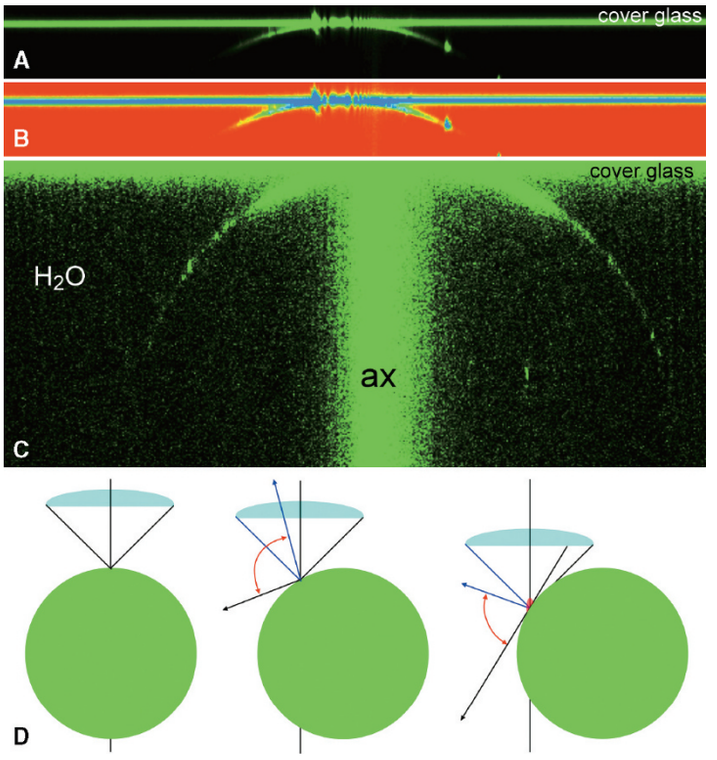

FIGURE 8.27. Reflected-light image of a glass bead, immersed in water and placed just under a cover glass. The bead was placed in the center of the microscope field, almost on the optical axis. (A) *xz* view shows the intensity "ripples" on the reflection signal from the coverslip surface caused by interference between the light reflected by the surface of the coverslip and that from the bead. (B) False color representation of (A); note the intensity fall-off from the "north pole" towards equator. (C) Same data with a higher detector gain setting to amplify weakly scattering signals such as the axial reflection (ax) from the microscope optics that is consequently visible at all *z*-positions. The surface of the sphere can be visualized down to ~30 degree north of the equator. (D) Diagram representing the relevant reflections.

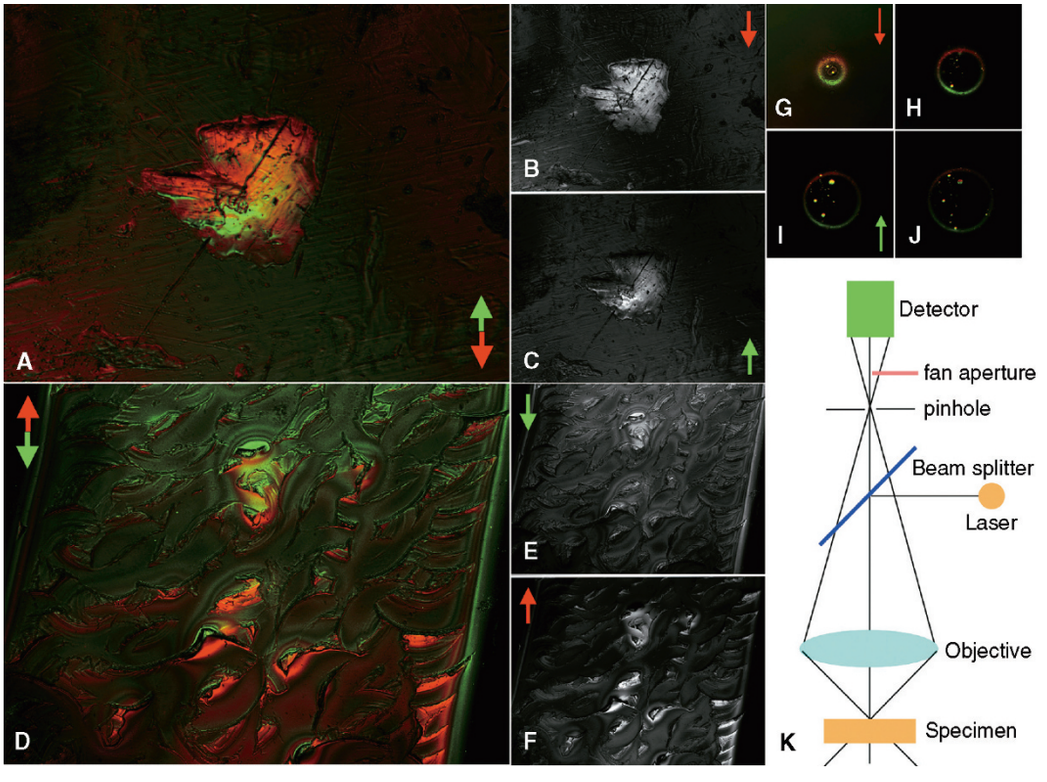

FIGURE 8.28. Surface orientation detection using reflected light imaging. (A) Color-coded surface orientation image of the surface features on a Singporian coin (*green and red arrows* show the orientation of surfaces). (B) and (C) are the individual images of the two surface orientations shown in (A). (D) Color-coded surface orientation image of a milled plastic surface showing cutting marks. (E, F) Corresponding orientation images shown in (D). (G–J) Color-coded surface orientation image of a glass bead. (K) Diagram of the microscope setup. Note how the use of a "fan aperture" obstructs signals from specific orientations. These effects were produced by introducing a two-position blade to obscure part of the "fan" of light behind the pinhole.

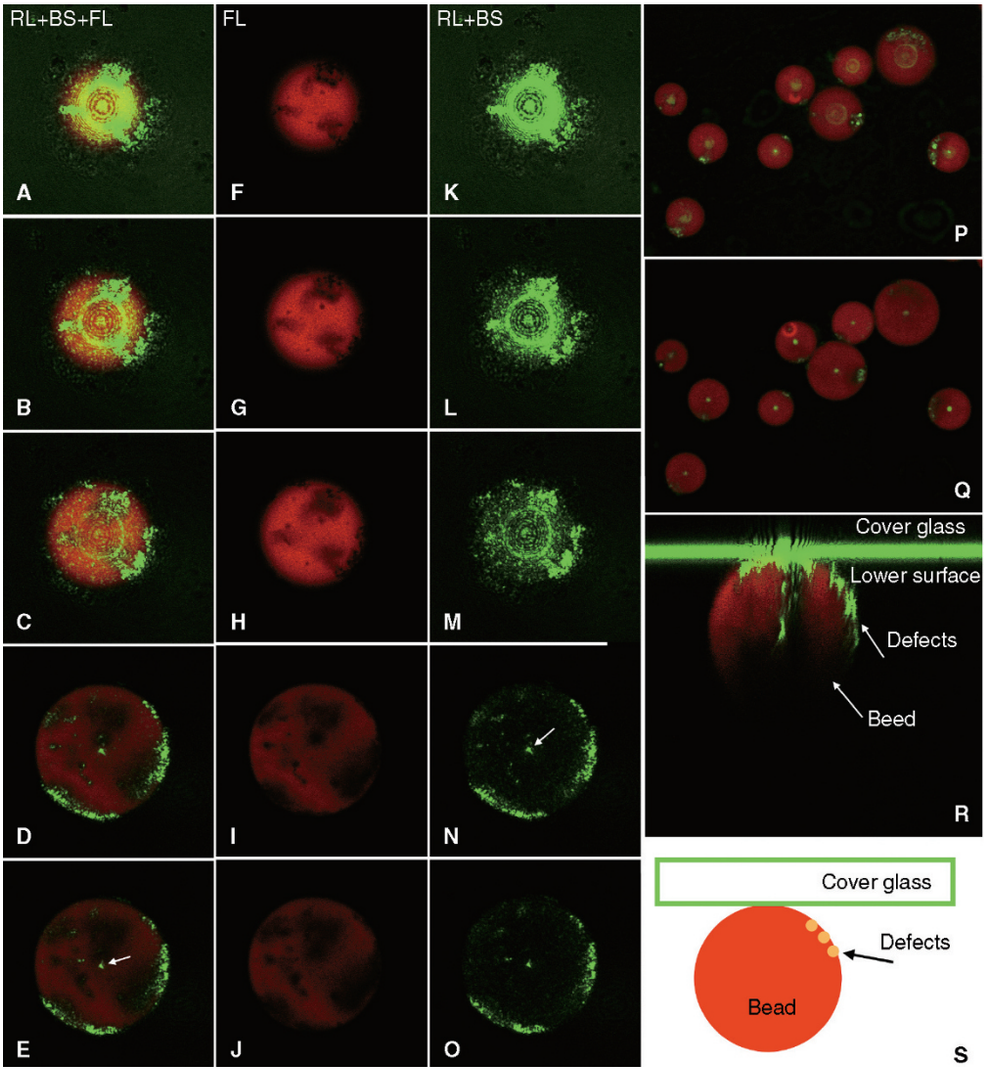

FIGURE 8.29. Confocal serial optical sections (A–E) of an 8 μm latex bead in water in fluorescence (F–J) and BSL (K–O) modes. (A–E) are combined images of fluorescence and BSL images. Note the axial reflection from the center of the bead and the "core" (*arrow*). The latex bead contains numerous "defects" that produce significant backscattered signal at various positions. (P, Q) Low magification optical sections of the beads showing the scatter "core" artifacts. (R) *xz* section of the bead shown in (A–E); (S) Diagrammatic representation of the imaging situation.

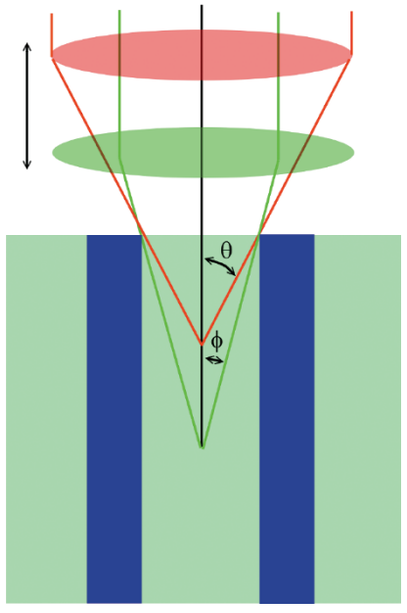

FIGURE 8.30. The "light piping" effect. When imaging features inside a highly absorbing tube-like structure (such as a vascular bundle in plants), the effective NA (or detection solid angle) decreases as the imaged plane moves deeper into the tissue (from θ to ϕ). This not only lowers the transverse and axial resolution of the microscope, but also decreases the signal intensity.

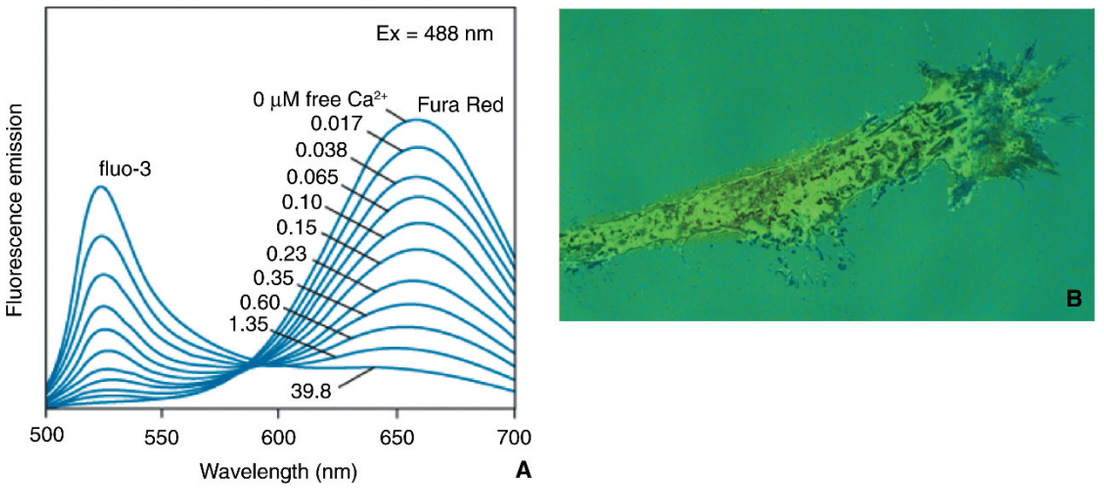

FIGURE 8.31. (A) The Fluo-3 and Fura Red indicator dye system allows ratiometric (Ca^{++}) determination using 488 nm excitation and detection at 520 nm and 660 nm. (B) Fluo-3/Fura Red used in TIRF to determine the (Ca^{++}) in the extracellular space between the cell membrane and the substrate.

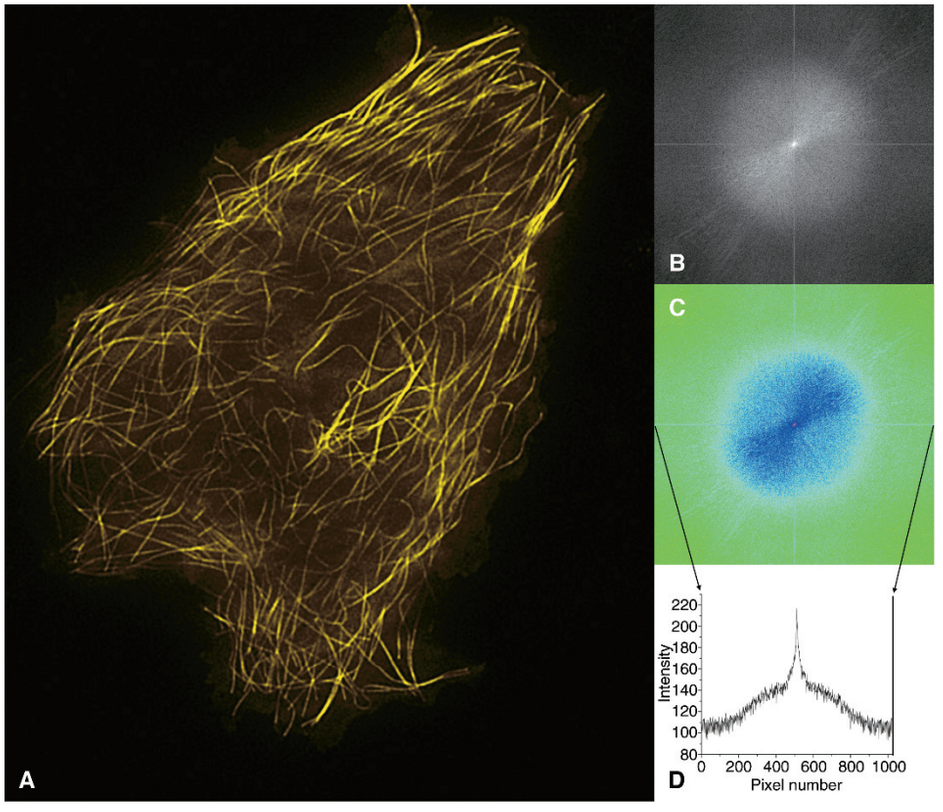

FIGURE 8.32. (A) TIRF micrograph of Vero cells transfected with EB3-GFP, a construct that marks microtubule plus ends, obtained with an Olympus TIRF microscope using an 60×/NA 1.42 oil-immersion objective and 488 nm excitation. (B) A fast Fourier transform (FFT) of the TIRF image; (C) false-color LUT of (B); (D) an intensity plot made horizontally across the diffraction pattern. (Images obtained at the 2005 International Course on 3D Microscopy of Living Cells at the University of British Columbia, Vancouver, Canada.)

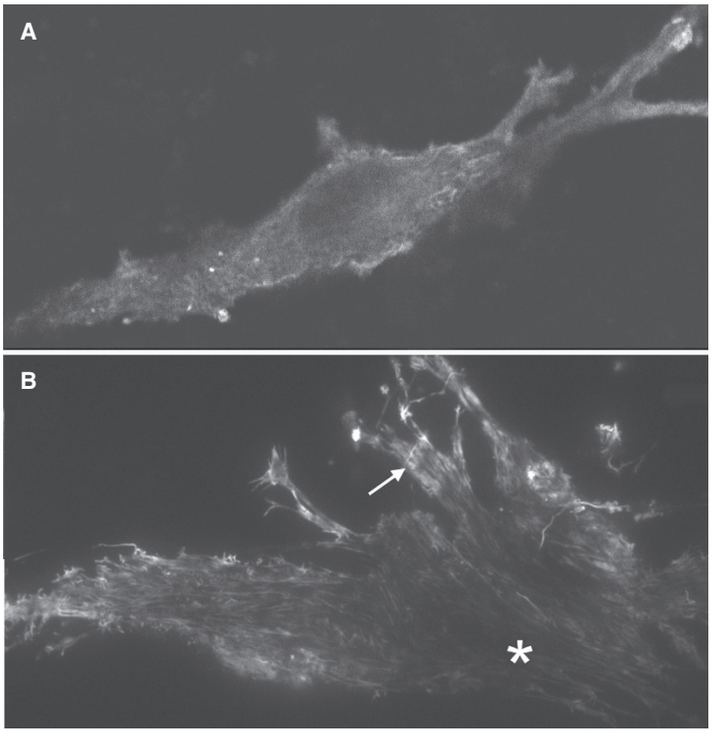

FIGURE 8.33. Comparison of confocal and TIRF Images of C2C12 cells transfected with GFP–MusculoTIRM, a novel TIRM family member specifically expressed only in skeletal and cardiac muscle cells. (A) Confocal image, collected with an Olympus Fluoview 1000 (60× NA 1.2/w objective) and deconvolved using AutoQuant AutoDeburr software. (B) TIRF image collected with Olympus TIRF system (60× NA 1.45/oil objective). Note the filamentous distribution near the plasma membrane is much clearer, and the trafficking of small particles can be observed better in the TIRF images. (Image courtesy of Zui Pan, Department of Physiology and Biophysics, UMDNJ-RWJMS, Piscataway, NJ. Image was taken at the 10th International Course on 3D Microscopy of Living Cells held at University of British Columbia, BC, Canada, 2005.)

comparison of confocal [Fig. 8.33(A)] and TIRF [Fig. 8.33(B)]. Images of C2C12 cells transfected with GFP–MusculoTIRM (a novel TIRM family member only specifically expressed in skeletal and cardiac muscle cells).

In TIRF imaging, whenever a high-RI cellular structure (e.g., an oil droplet) is in intimate contact with the coverglass, the incident ray will propagate into the droplet and become far-field illumination. "Leaked" light produced in this way can increase the background signal dramatically. In addition, TIRF excitation can occur not only at the defined glass–water interface, but also in a conventional epi-fluorescent microscopy wherever structural interfaces occur that have the proper RI and orientation to satisfy the TIRF condition. Consequently, most recorded fluorescence images are "contaminated" by a small but variable TIRF component.

Fluorescence Resonant Energy Transfer

Fluorescence resonance energy transfer (FRET) occurs when energy passes from one excited molecule (the donor) to a second molecule (the acceptor) because the emission spectra of the former overlaps the excitation spectra of the latter. However, the efficiency of this transfer is only significant if the two molecules are very close to each other (1–10 nm). As the efficiency of this energy transfer (E) varies inversely with the sixth power of the distance (r) between the donor and the acceptor, the ratio of the fluorescence intensity of the donor compared to that of the receptor is a measure of distance between them. Therefore, FRET can be a sensitive nonlinear measurement of inter-fluorophore distance, r, or of the rate of energy transfer,

$$E = R_0^6/(R_0^6 + r^6)$$

where E is the energy transfer efficiency and r is the distance between donor and acceptor. This leads to

$$E = 1 - (I_{DA}/I_D)$$

where I_D and I_{DA} is the intensity of the signal from the donor in the absence of, and the presence of, the acceptor, respectively.

The Förster distance R_0 is the distance, r, at which half the excitation energy of the donor is transferred to the acceptor while the other half is dissipated by all other processes, including light emission.

$$r = R_0\{(1/E) - 1\}^{1/6}$$

$$R_0 = 0.211\{K^2 n^{-4} Q_D J(\lambda)\}^{1/6}$$

where Q_D is the quantum yield for the donor, K_2 is a factor describing the relative dipole orientation between the two molecules, and $J(\lambda)$ is the overlap integral that accounts for the degree of spectral overlap between the donor emission and the acceptor absorption

$$J(\lambda) = \frac{\int_0^\infty f_D(\lambda)\varepsilon_A(\lambda)\lambda^4 d\lambda}{\int_0^\infty f_D(\lambda) d\lambda}$$

where $f_F(\lambda)$ is the corrected fluorescence intensity of the donor wavelength in the range λ and $\lambda + d\lambda$, with the total intensity normalized to unity, $\varepsilon_A(\lambda)$ is the extinction coefficient of the acceptor at λ, and is measured in units of $M^{-1}cm^{-1}$ (see also Chapter 45, *this volume*).

Figure 8.34 shows an intensity-based 2p-FRET data analysis that was used to localize the dimerization of C/EBPα proteins in the nuclei of GHFT1-5 cells. Figure 8.35 shows tissue FRET in traumatic axonal injury using BAD/Alexa 488 as the donor and Bcl-xL/Alexa 555 as the acceptor. The image demonstrates energy transfer consistent with BAD-Bcl-xL heterodimerization.

When the acceptor is bleached, the lifetime of the donor molecule increases because there are now fewer paths for excited donor molecules to lose their energy. Figure 8.36 combines FRET and fluorescence lifetime microscopy (FLIM, see below and also Chapter 27, *this volume*) to localize interacting protein molecules.

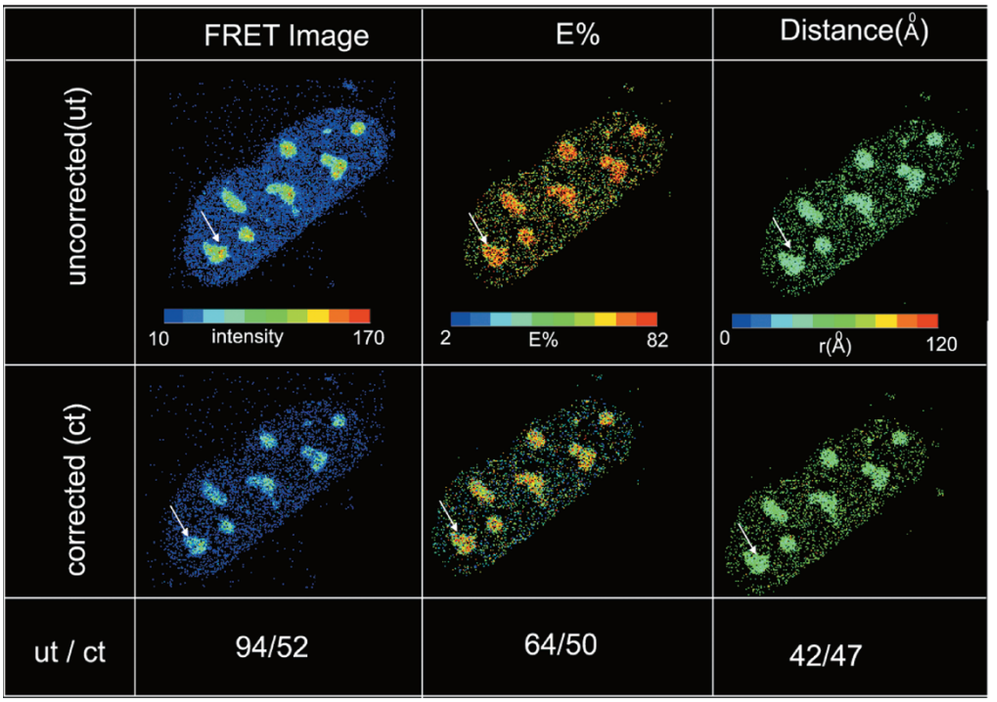

FIGURE 8.34. Intensity-based, quantitative 2p-FRET data analysis to localize the association of C/EBPα proteins in the nuclei of GHFT1–5 cells. Seven images were acquired using a Bio-Rad Radiance 2100 confocal/multiphoton microscopy as the data input for "precision-FRET" (PFRET, http://www.circusoft.com) imaging. The color bars clearly demonstrate the presence of acceptor and donor spectral bleedthrough (SBT) requiring correction. The top panel shows the uncorrected FRET, *E%*, and distance images and their respective color bars. The bottom panel shows the two-dimensional distribution of corrected FRET, *E%*, and the distance (*r*) images. For the protein complex marked with an arrow, the energy transfer efficiency, *E*, is 64% before correction and 50% after correction for Donor, and Acceptor spectral bleedthrough. The color image helps to identify the 2D distribution of distance between interacting protein molecules. (Images courtesy of A. Periasamy, University of Virginia, Charlottesville, Virginia.)

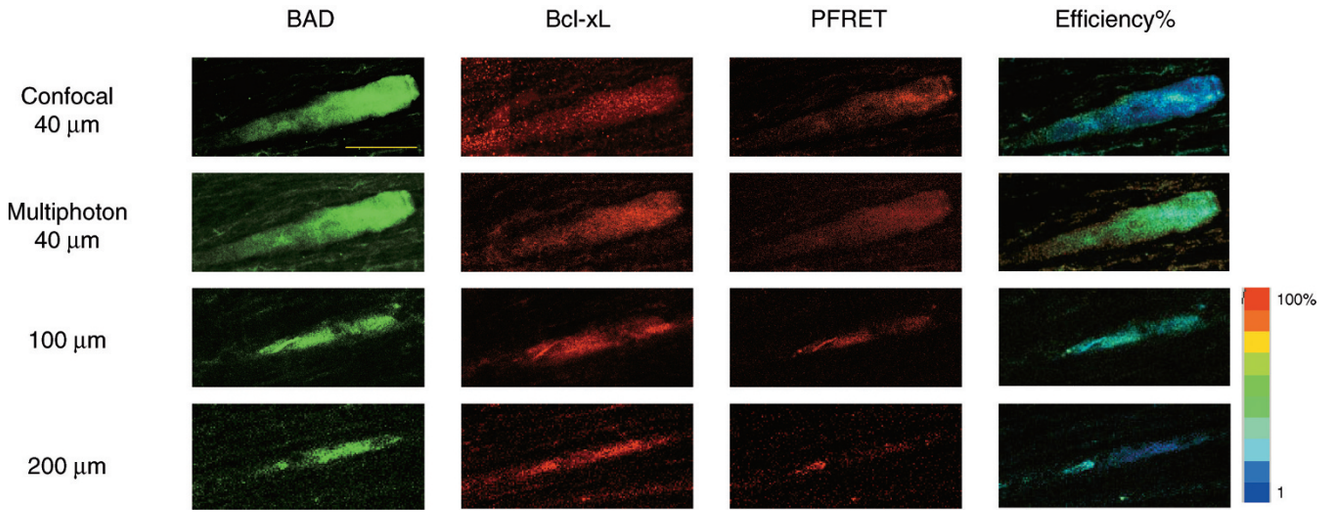

FIGURE 8.35. Tissue FRET in traumatic axonal injury. Six hours postinjury, the tissue was labeled with BAD/Alexa 488 (donor) and Bcl-xL/Alexa 555 (acceptor). These results show energy transfer consistent with BAD-Bcl-xL heterodimerization. The same tissue was used for both confocal-FRET and 2p-FRET imaging using a Bio-Rad Radiance 2100 confocal/multi-photon microscope. Although confocal "precision-FRET" (PFRET, http://www.circusoft.com) imaging was confined to the outer 40 µm of the specimen by low signal levels, 2p (or multi-photon) PFRET images provided useful data up to 200 µm into the tissue. This difference can be attributed to higher concentrations of the fluorophore deep inside the tissue and also to the fact that visible FRET signals scatter in the tissue and can only be detected with a non-descanned detector. Bar, 10 µm; 20× MIMM NA 0.75; Confocal-exD 488nm, emD 528/30, exA 543, emA 590/70; 2-photon-exD 790, exA 730. (Images courtesy of A. Periasamy, University of Virginia, Charlottesville, Virginia.)

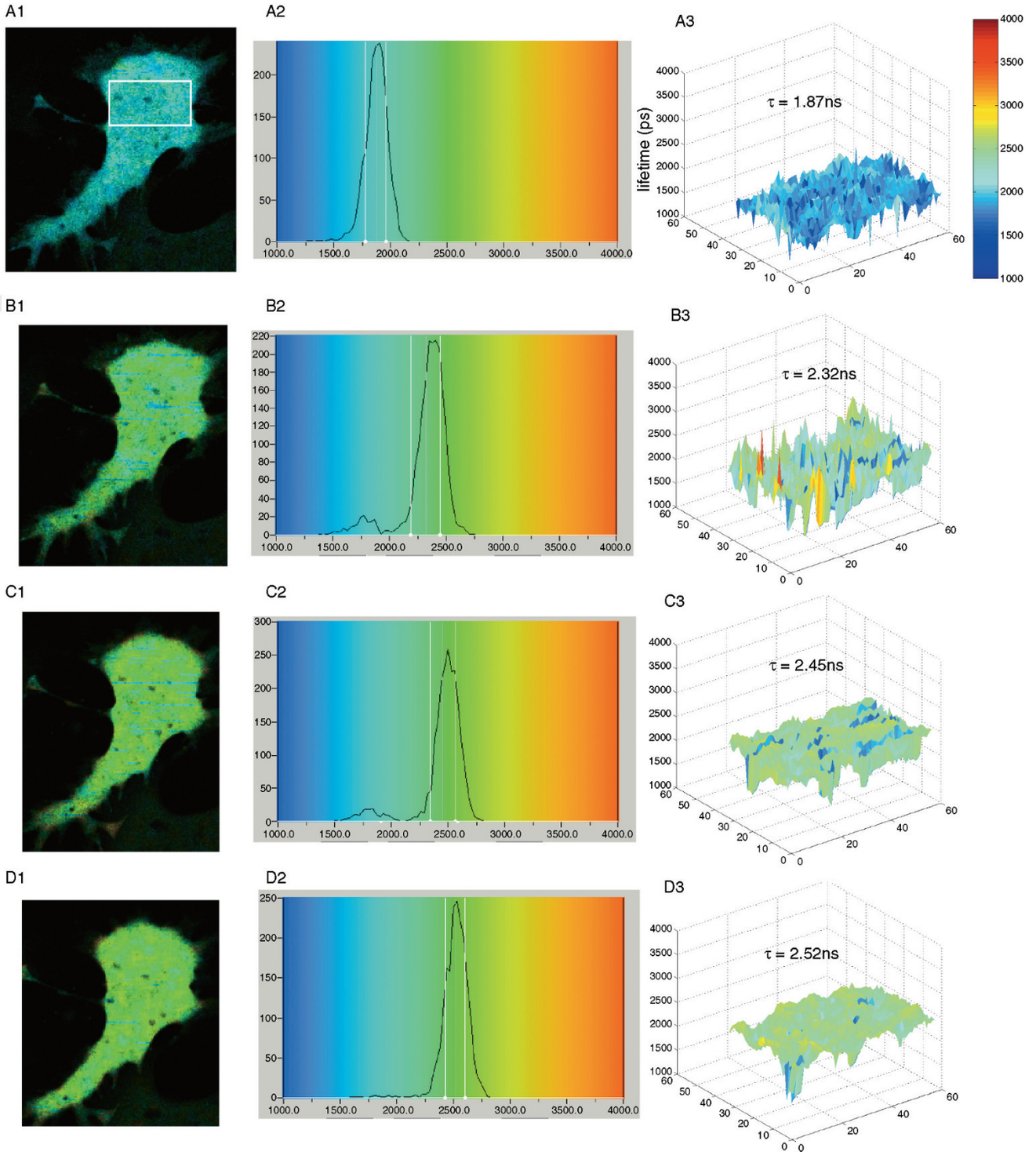

FIGURE 8.36. FRET-FLIM microscopy to localize interacting protein molecules. Images of cells expressing a FRET test molecule (eCFP coupled directly to eYFP through a 15 amino acid linker: eCFP-15aa-eYFP) were acquired and analyzed using time-correlated single-photon counting FRET-FLIM microscopy (TPSPC, Becker-Hickl, Berlin, Germany). The mean lifetime of the selected ROI was 1.87 ns in the presence of acceptor (A1 and A2) but the lifetime returned to 2.52 ns, the natural lifetime of eCFP (D1 and D2) after photobleaching of the acceptor molecule with 514 nm light, demonstrating that FRET had been occurring. As is illustrated in the 2D (A2–D2) and 3D (A3–D3) lifetime distribution, the average lifetime of the donor molecule steadily increases as more acceptor molecules are bleached. (Images courtesy of A. Periasamy, University of Virginia, Charlottesville, Virginia.)

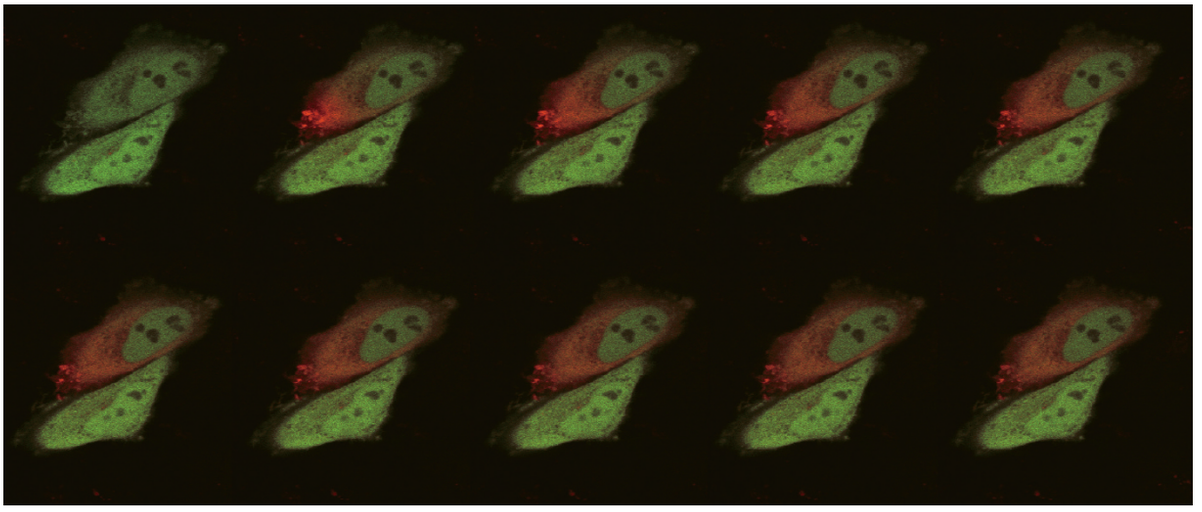

FIGURE 8.37. Fluorescence recovery after photobleaching (FRAP). Photobleaching of the fluorescent protein Kaede causes it to emit in the red, rather than the green. After bleaching between the first two images, the red fluorophores are slowly replaced by green ones.

Images of cells expressing a FRET test molecule (eCFP coupled directly to eYFP through a 15 amino acid linker: eCFP-15aa-eYFP) were acquired and analyzed using TCSPC (Becker-Hickl, Berlin, Germany) FRET-FLIM microscopy. The fact that the mean lifetime of the selected region of interest (ROI) was 1.87 ns in the presence of acceptor (A1 and A2), but returned to 2.52 ns, the "natural" lifetime of eCFP after the acceptor molecule was photobleached using 514 nm light (D1 and D2) shows that FRET had been occurring. This increase is illustrated in 2D (A2–D2) and 3D (A3–D3) lifetime distributions (Chen *et al.*, 2003).

Fluorescence Recovery After Photobleaching (FRAP and FLIP)

Fluorescence recovery after photobleaching (FRAP) has been used in biological research for more than three decades following the pioneering work of Webb (1976), who used it to study the lateral movement of Ach receptors in cell membranes. In this technique, a small region of interest is selectively photobleached with a high-intensity laser, and one then uses a low-intensity beam to monitor the recovery of the fluorescence intensity as unbleached molecules move back into the bleached region. The movement of the molecules can result from simple diffusion, from binding/dissociation, and/or from active transport, etc.

Analysis of the fluorescence recovery can be used to determine kinetic parameters of tagged proteins or other molecules, including their diffusion coefficients, pool fraction, transport rates, or binding/dissociation from other molecules.

In a typical FRAP experiment, the fluorescence in the region of interest is measured just before, ideally also during, and also after photobleaching. Figure 8.37 shows a pair of cells expressing the fluorescent protein Kaede, which changes its emission from green to red in response to photodamage. The sequence of eight images allows one to see the upper cell be "bleached" and then to follow the replacement of the damaged, "red" Kaede with undamaged green-emitting molecules.

From such images one may plot a recovery curve. Depending on the complexity of the interactions of the molecule of interest, the curve may have different shapes. From a simple, single exponential curve one can calculate the mobile fraction, R:

$$R = \frac{(F_\infty - F_0)}{(F_i - F_0)}$$

The $t_{1/2}$ is the time required for the fluorescence to recover half the way between the fluorescence level after bleaching (F_0) and that at the plateau level (F_∞). Although measuring the $t_{1/2}$ allows one to compare diffusion rates under different conditions, one must correct for the fact that the data-acquisition scans used to monitor fluorescence recovery may also produce some bleaching.

In the image, the difference between the bleached area and the surrounding un-bleached area provides bleaching contrast and this can be seen by simple image subtraction.

Following similar reasoning, one can monitor the continuity of cellular compartments with a technique called fluorescence loss in photobleaching (FLIP). In FLIP, a small region within a fluorescent cell is continuously photobleached while one images the whole cell. Over time, any cellular compartments connected to the area being bleached will gradually lose fluorescence as mobile molecules move into the bleached area, while the fluorescence in unconnected regions will be unaffected. In addition, FLIP can be used to assess whether the tagged molecules move freely between particular cellular compartments or if they undergo interactions that impede their motion. FLIP can also be used to reveal faint fluorescence in unconnected compartments that is obscured by bright fluorescence in the component being bleached.

A typical method for doing FRAP with a single-beam confocal or multi-photon microscope is to scan a small region of interest using a high-intensity illumination,[2] then use a low magnification setting and low beam power to scan a larger area. Some modern confocal microscopes, such as the Olympus Fluoview1000, are equipped with dual scanners: one for bleaching (and photoactivation), and the other for imaging. The FRAP data are typically either presented in *xyt* format or condensed into an intensity versus time plot (Reits and Neefjes, 2001; Patterson and Lippincott-Schwartz, 2002).

[2] Be careful not to use such a high power density that nonlinear damage mechanisms bias the outcome. See Chapters 38 and 49, *this volume*, for details.

STRUCTURAL CONTRAST

Harmonic Generation Contrast

At high illumination intensity, biological specimens exhibit a number of nonlinear optical responses; these include the emission of multi-photon fluorescence, nonlinear absorption that can lead to photodamage, and other photochemical responses (see Chapters 21 and 28, *this volume*). In addition, a number of biological structures, such as collagen fibers and plant cell walls, exhibit biophotonic properties capable of generating a SHG signal. Frequently, structures of this type are also birefringent.

The SHG signal provides information about features of the object that are composed of nano-scale crystalline structures that destroy optical centro-symmetry. On the other hand, optical interfaces in a cell or tissue provide the conditions needed to generate THG. Therefore, the THG signal represents optical interfaces such as those found at the cell membrane or at the surfaces of organelles. For a detailed discussion on harmonic signal generation, readers are kindly referred to Chapter 40.

Birefringence Contrast

A number of biological structures, including many of those important to cell motility, organization, and division, are birefringent. For example, microtubules, thin filaments, and myofibrils are all birefringent and can therefore be studied by using polarization microscopy (Fig. 8.38; also see Fig. 8.3, a set of polarization images of the collagen fiber orientation in an artificial 3D substrate used in tissue engineering). Conventional polarization microscopy uses two crossed polarizers above and below the specimen to achieved background extinction and make birefringent material appear as shades of gray on a black background. However, because obtaining a full understanding of the birefringence properties of the specimen using traditional polarization microscopy requires that the specimen be mounted on a centerable rotation stage, the technique was seldom used in biology. More recently, developments in liquid crystal technology have made it possible to implement dynamic polarization microscopy without mechanically rotating the specimen (Shribak and Oldenbourg, 2003). Liquid-crystal components permit one to change the orientation of polarizers, compensators, and analyzers rapidly and electronically, and to record three images, each made with the polarizing components in a different orientation, and then display a processed image in which the brightness of each pixel is proportional to the local retardance while its color codes the orientation of the structure (Oldenbourg, 2004). Figure 8.39 demonstrates variations in the retardance and orientation of the cell wall in plant tissues.

This technology has been used extensively in the study of the microtubule dynamics that drive cell movement. In addition, the technique has been used to identify the position and orientation of the first-division, mitotic apparatus in *in vitro* fertilization (IVF) procedures involving both human and endangered species (see Figs. 40.19 and 40.20, *this volume*).

Both the retardance and orientation of the birefringent structure can be calculated by simple algorithms from a set of three images obtained under different polarization conditions.

DERIVED CONTRAST (SYNTHETIC CONTRAST)

A combination of intrinsic and extrinsic factors can generate "synthetic" contrast. For example, images can show structural or spectral variations within a cell as a function of time, or indicate membrane potential or pH (ratio imaging). If fluorochrome-conjugated antibodies or fluorescent dyes are used to chemically tag specific molecules, these will fluoresce when the specimen is excited by a suitable light source, and create extrinsic contrast because the contrast depends on the binding specificity of fluorescent probes. This probe specificity is frequently used in conjunction with pulse-chase experiments to elucidate time-dependent events (in fact, such pulse-chase experiments can be considered another contrast mechanism).

To obtain a good confocal image, one must selectively combine extrinsic and intrinsic factors to emphasize the "image" signal and decrease the "background" signal. This can be done by improving the performance of the optics and by using special optical contrast methods. However, the prime factor determining the usefulness of an image is almost always the preparation of the specimen (Chapter 18, *this volume*). Because commercially available, multi-channel

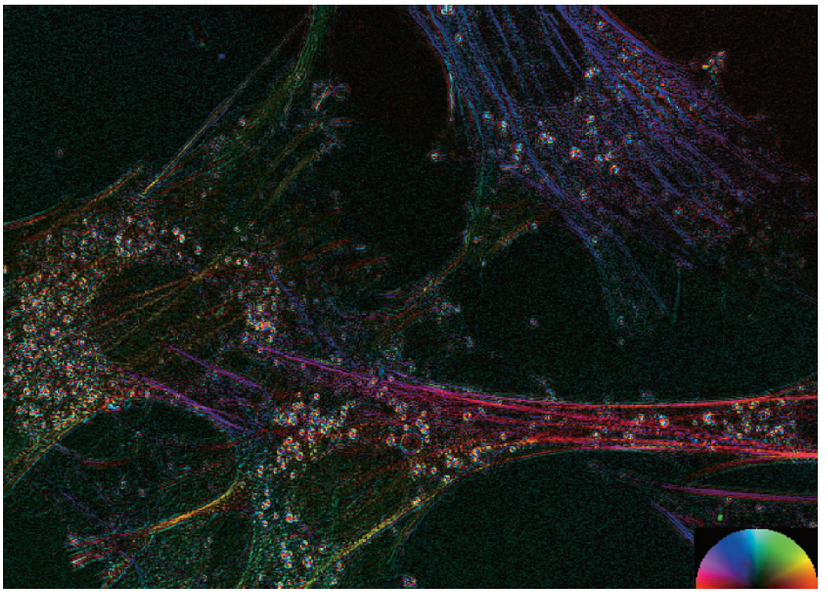

FIGURE 8.38. Polarization micrograph showing the orientation of cytoskeletal structures in a tissue-culture cell.

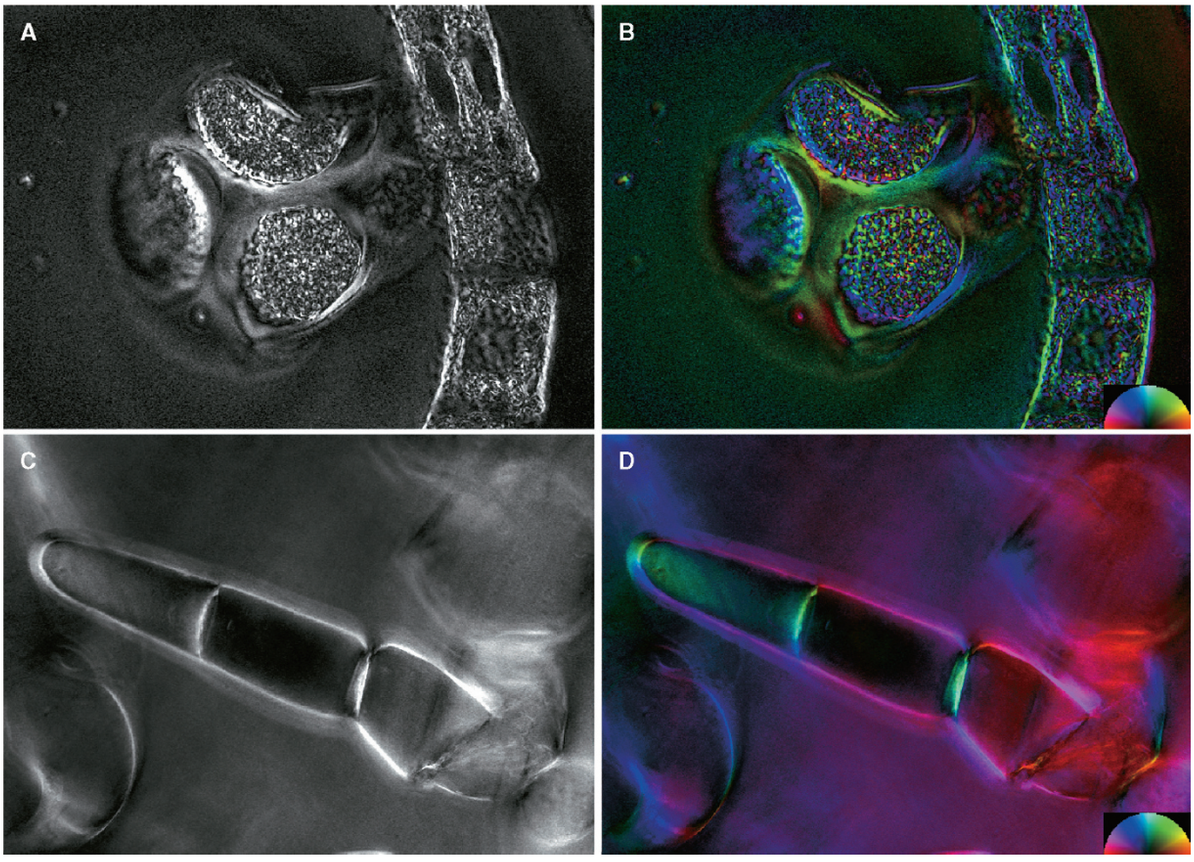

FIGURE 8.39. Birefringence images of developing microspores in *Cymbopetalum baillonii* (A, B) and in the cell wall of tobacco suspension-culture cells (C, D). (A) and (C) show retardance, (B) and (D) are color-coded for orientation. (Images courtesy of Chih-Hua Tsou and Hsing Yue-Ie Caroline of the Institute of Plant and Microbial Biology, Academia Sinica, Taipei, Taiwan.)

confocal microscopes can form images based on the detection of BSL and epi-fluorescence signals, we will discuss the various factors that affect the contrast of these images in more detail.

Ratiometric

In most fluorescence microscopy experiments, the intensity recorded in any pixel is proportional to the absorption cross-section, QY and concentration of the dye, and the size of the volume in the specimen recorded by this measurement (i.e., its *x*-, *y*-, *z*-resolution). These techniques depend on the fact that the spectral characteristics (absorption cross-section, QY), of some fluorophores (or combination of fluorophores) may change in response to the ionic or pH environment. However, these measurements can only be qualitative unless one can normalize for the concentration of the dye. As the concentration is difficult to control, it is often more convenient to normalize this number by making a ratio of two different measurements of the same molecules. Although the classic example involves the Ca^{++} indicator dyes, Indo-1 or Fura-2, other types of ratiometric imaging are also used to detecting ionic or pH changes in cells (see Chapters 16 and 42, *this volume*). By using a standard titration curve and ratioing the intensity of images obtained at two wavelengths, one can assign false colors in the resulting image to represent the actual ion concentrations or pH values. Figure 8.31 shows a typical fluorophore combination (Fluo3 and Fluro-red) used for detecting the Ca^{++} concentration (see also Fig. 21.33, *this volume*). Extensions of this technique can be applied to other situations; for example, in a photodamage experiment, images obtained at different time points can be ratioed to provide a contrast that shows the photodamage dynamics of various cellular compartments.

Deconvolution

In a widefield optical microscope, energy emitted by a point source is captured by the objective lens and imaged as a blurred set of diffraction fringes known as the point spread function (PSF). Thus, any image obtained from a microscope, $o(x, y, z)$, is actually the **convolution** of the function describing the actual light intensity distribution inside the original specimen in 3D $i(x, y, z)$ with the PSF $p(x, y, z)$,

$$o(x, y, z) = i(x, y, z) \otimes p(x, y, z)$$

Therefore, the PSF is the function that redistributes the original energy distribution from the specimen into the imaging space (Chapter 21, *this volume*). In the absence of noise, the mathematical operation of **deconvolution** reverses this process, creating a new 3D image data set that more closely approximates the structures of the specimen. It can increase the image contrast, reduce the effect of Poisson noise, and also decrease the effect of out-of-focus signals (Holmes and Cheng, 2005). Although in general, successful use of iterative deconvolution to improve 3D microscopical data requires that one know the PSF, so-called "blind" techniques can also be successful, as is explained in Chapter 24. However,

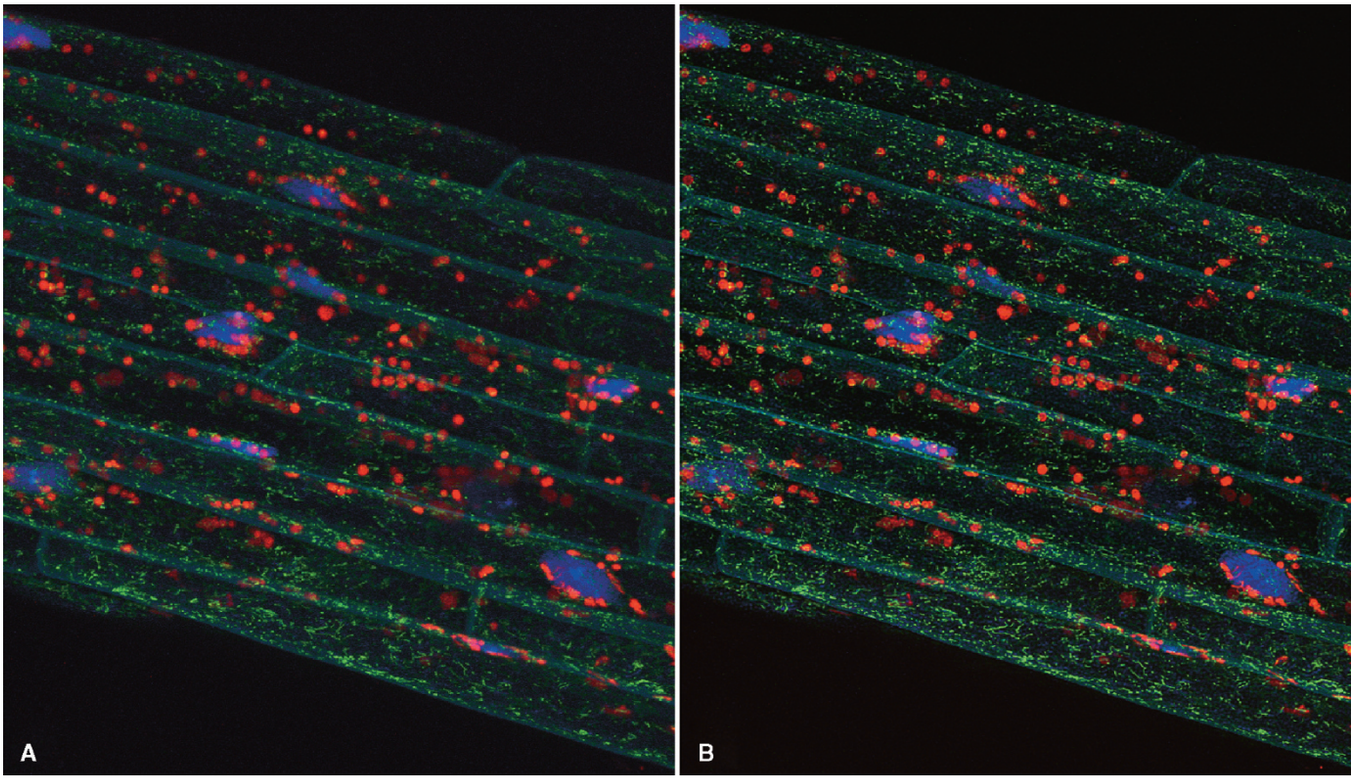

FIGURE 8.40. (A) Three-channel confocal microscopy of a 5-day-old, stable, transgenic seedling of *Arabidopsis thaliana*, simultaneously expressing four different recombinant proteins, ECFP-Gal4, EGFP-BDCaM53, EYFP-CoxIV, and DsRed2-RecA. ECFP-Gal4 accumulates in the nucleus and EGFP-BDCaM53 in the plasma membrane, EYFP-CoxIV accumulates in mitochondria and DsRed2-RecA in plastids. ECFP and EGFP can be excited and collected in a single channel because, as they are expressed in two distinct structures — namely, nucleus and plasma membrane — they are unlikely to be confused. (B) The same data, after blind deconvolution. (Images kindly provided by Naohiro Kato, Department of Biological Sciences, Louisiana State University, Baton Rouge, Louisiana, and obtained at the 2005 International Course on 3D Microscopy of Living Cells held at University of British Columbia, Vancouver, Canada.)

iterative techniques require that one be able to describe image quality in a mathematical and measurable fashion so that the results from one iteration can be compared with the previous one. For a detailed discussion on deconvolution operation, readers are kindly referred to Chapters 22, 23, 24, and 25.

The practical effect of deconvolution on contrast is that, on a basic level, deconvolution of confocal data acts as a nonlinear filter, something that reduces image contrast somewhat but also adaptively averages the signal over a large number of voxels, effectively eliminating the "single-pixel" noise features produced by Poisson noise (Fig. 8.40).

Movement Contrast (Subtraction of Previous Image)

Organelle movements within the cytoplasm or any other movements of the object can be emphasized and tracked by sequentially subtracting from each other images in a time series. For instance, subtracting an image of a culture cell obtained at time A from one obtained at time B can reveal small movements of organelles and/or the cytoskeleton; on the other hand, converting three consecutive time-sequenced images into RGB format can also effectively display structural movement (Fig. 8.41). This display technique emphasizes those structures that have moved between the two sampling times. Clearly, in order to obtain useful and reliable movement contrast, it is important that the sampling interval is small enough to faithfully record the movement. Otherwise, subtracting the resulting images can produce only nonsense.

Image movement due to specimen drift or a change in the water level of a water-immersion setup is a common problem. It is important to keep the specimen immobile while not exerting external forces that can deform it. Figure 8.42 shows a number of methods for holding the specimen and a simple apparatus to maintain immersion water levels for a prolonged period.

Spectral Unmixing and Color Reassignment

Using spectral unmixing techniques, one can characterize a pixel or an image region based on its spectral signature. Although such pixels may appear similar in RGB color to the naked eye [Fig. 8.43(A)], they may in fact have very different spectral signatures that only become visible when each one is assigned to a specific color. For example, Figure 8.43(B) shows a RGB image of a histological section of mouse intestine, stained with Syto Blue [Fig. 8.43(C)], Alexa Fluor 488 [Fig. 8.43(D)], Alexa Fluor 594 [Fig. 8.43(E)], and Alexa Fluor 647 [Fig. 8.43(F)], and also containing a significant amount of autofluorescence [Fig. 8.43(G)]. One can use spectral unmixing to separate the signals from the four fluorescent probes and the autofluorescence, and then generate a synthetic false-color image based on these four spectral categories. For other examples of spectral unmixing, see Figures 36.17 and 21.20.

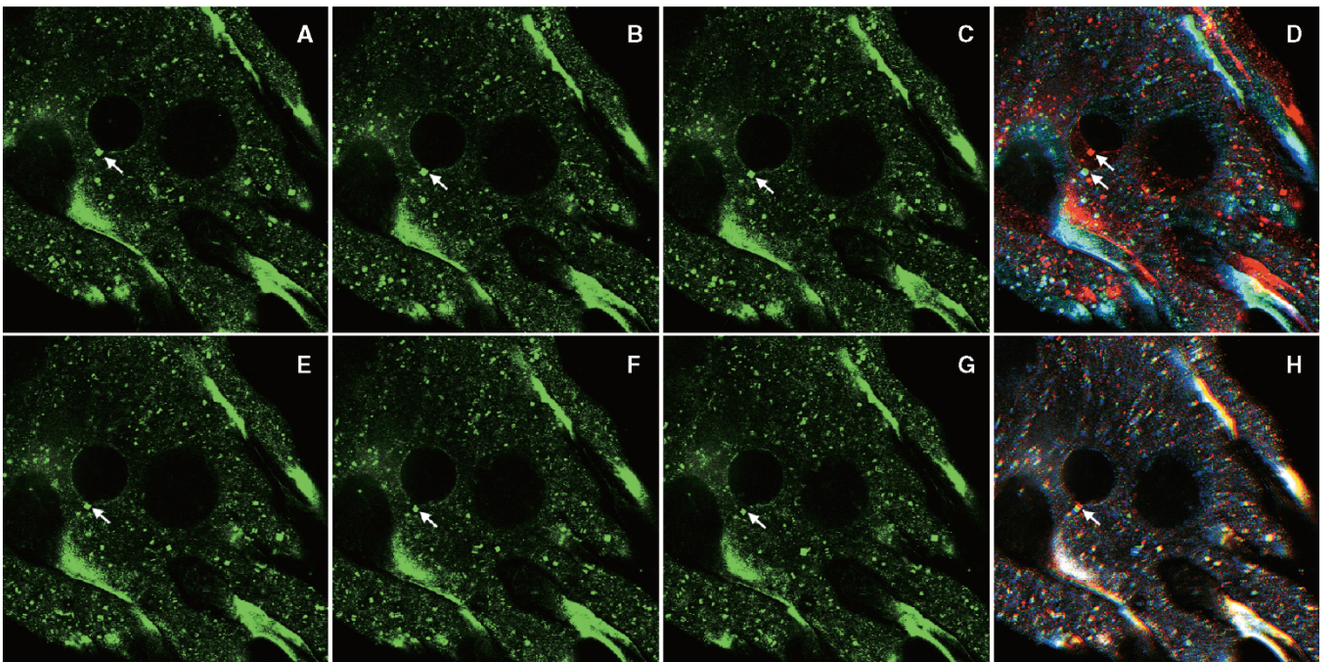

FIGURE 8.41. A time-lapse series of confocal optical sections was made using backscattered light to show movement of an amoeboid pseudopod. (A, B, C) and (E, F, G) are two time sequences of the pseudopod showing highly reflective crystals (*arrow*) and the plasma membrane. Note the scatter signal from the vacuole membrane. (D and H) are RGB merged images of (A, B, C) and (E, F, G), respectively, showing the organelle movement. The time interval is approximately 0.5 s.

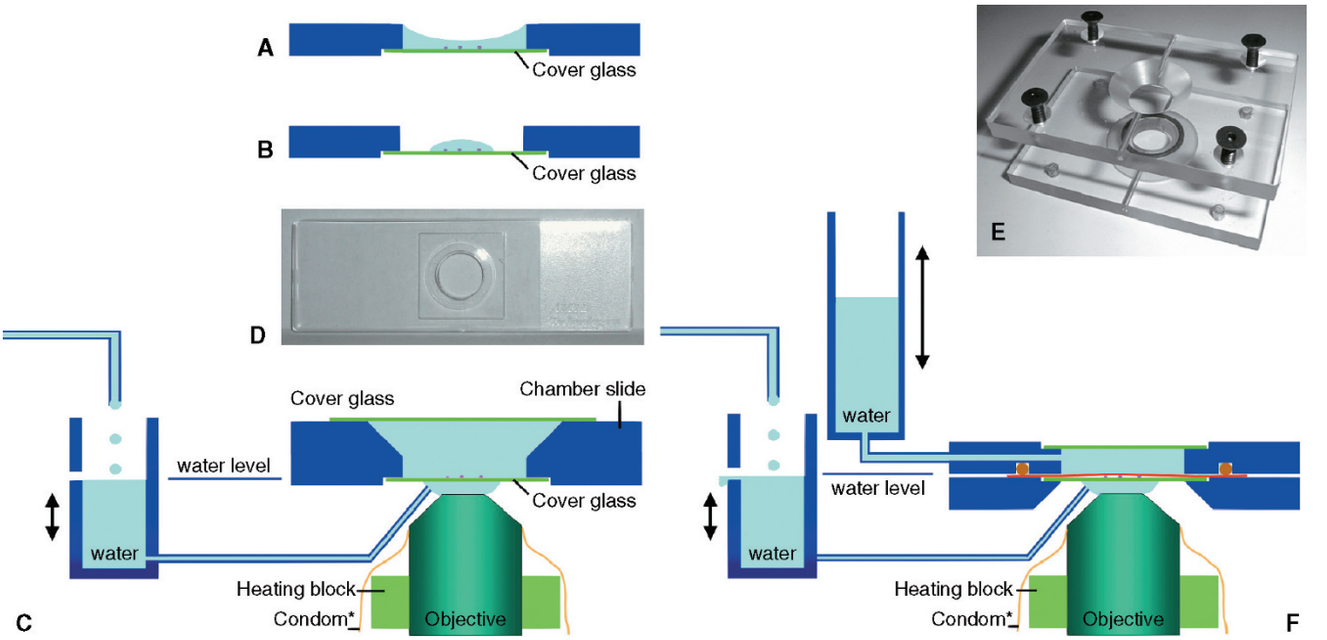

FIGURE 8.42. Various specimen chambers to handle small specimens. (A) and (B) chamber constructed using a slide with a center hole (C), the bottom of which is covered with a cover glass; the chamber can either be filled with liquid (A) or one can use a drop of medium (B) to create reflective meniscus, although this may introduce unwanted reflections. However, if an upper cover glass is used, the liquid meniscus problem is resolved (D). To prevent the immersion water from drying out (when using a water immersion objective), a water reservoir with overflow is used. By careful adjustment of the position of the overflow outlet, one can maintain the water level at the objective. A non-lubricated condom with its tip cut off is used to dress the objective lens to prevent water damage. (E) A specially made specimen chamber to handle small tissues (Cheng *et al.*, 1999). (F) Detailed diagram of the chamber shown in (E). The chamber consists of two compartments, the upper chamber connected to a water reservoir, maintaining a specific pressure on the red membrane (typically 10 µm Mylar), and this film then presses the small tissue fragment against the lower cover glass.

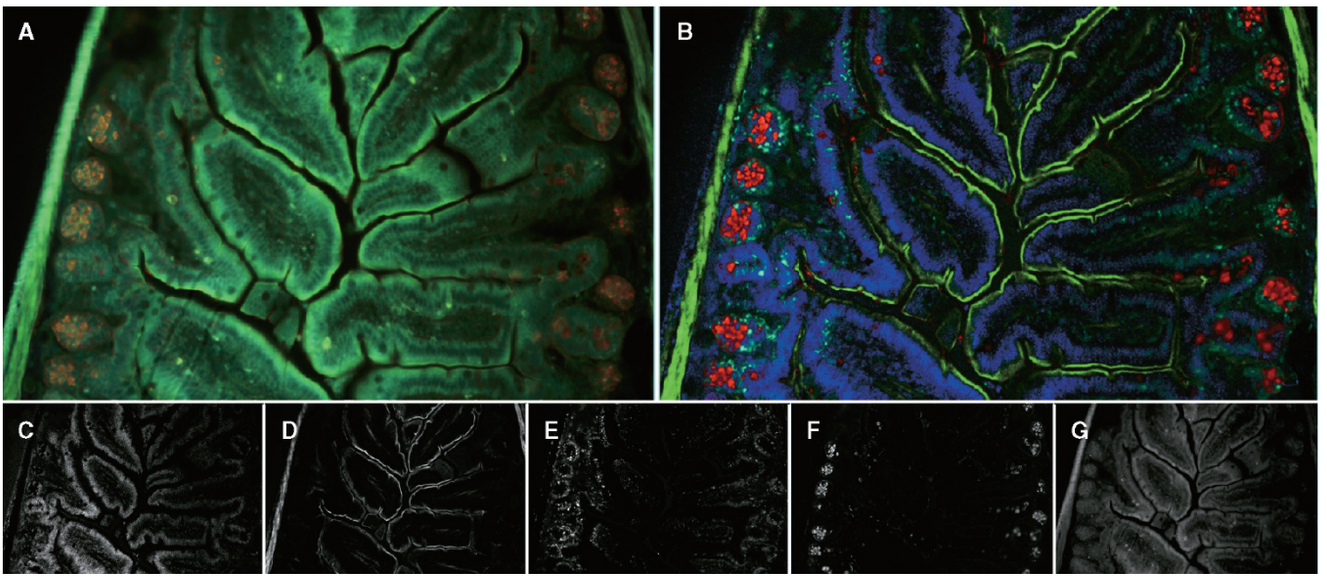

FIGURE 8.43. Mouse intestine specimen, labeled with Sytox Blue and Alexa Fluor 488, 594, and 647. (A) Conventional three-color image (B) composite of four component images extracted from the same data by "spectral unmixing." (C) Sytox Blue, (D) Alexa Fluor 488, (E) Alexa Fluor 594, (F) Alexa Fluor 647, and (G) autofluorescence. (The images were obtained using the Nuance imaging system of Cambridge Research Inc. (Cambridge, MA). Image courtesy of CRI.)

Effects of the Specimen: Spherical Aberration and Optical Heterogeneity

Although substantially transparent, biological specimens are seldom optically ideal. More often they are heterogeneous in structure, absorption, RI, and thickness. Because the specimen is part of the optical system, this heterogeneity can be particularly serious in a confocal microscope where each point is, in effect, imaged twice.

We can divide these effects into two categories: those that arise because the average RI of most biological specimens is not that for which the objective was designed and those caused by the fact the cells actually do not have one RI but many (i.e., they are optically lumpy and the lumps often have different RIs).

The first problem leads to spherical aberration, a topic that is discussed in many other chapters, particularly Chapter 20. Although, in general, spherical aberration can be avoided by scrupulous adherence to the recommendations of the manufacturer with regard to the RI and thickness of all layers between the objective and the focus plane, this is not always easy to do. Water objectives assume that the specimen is made of water and, as this is not true of living cells,[3] some degree of spherical aberration is usually present in images of living specimens. Indeed, spherical aberration is usually the main reason why the signal level drops as the focus plane moves into the specimen (Fig. 8.44).

Figure 8.45 clarifies the connection between reduced resolution and lower signal level. A dry objective was used to bleach planes into a piece of fluorescent plastic. Because the objective was designed to provide full spherical correction only on the far side of a 170 μm coverslip, the best resolution (and highest light intensity) is found when the focus plane is some distance into the plastic. This figure confirms that the zone with the sharpest images [as seen in Fig. 8.45(B)] coincides with that having the highest signal [Fig. 8.45(C)]. Figure 8.46 drives the point home: *xy* images made of the same specimen, after it had been cut and polished to show the planes in edge view, show that the planes bleached in the "good" zone were indeed thinner than their neighbors and have the correct spacing. It is important to point out that the RI mismatch of the plastic specimen and the immersion medium (1.52) results in a change in the effective focal length that varies with focus plane position. This causes the spacing **between** the bleached planes to vary as a function of the depth.

On the horizon is a better solution: a stand-alone, motorized, computer-controlled spherical-aberration corrector is now available (Intelligent Imaging, Denver, CO) and one can imagine the day when a device with similar capabilities may become a standard microscope accessory.

However, such a device cannot correct for the optical problems caused by the optical heterogeneity of the specimen itself (see Figs. 2.3–2.5). As with the BSL imaging, reflection, refraction, and scattering of the illuminating beam by structures situated between the focal plane and objective lens produce a spot that is larger than it would have been if the optics were only limited by diffraction and this reduces the intensity of the exciting radiation reaching the fluorescent dye in each voxel being sampled.[4] This loss of excitation reduces the fluorescence yield from the focal spot in the specimen. Furthermore, the emitted fluorescent light will be attenuated by the same factors on its return to the detector pinhole. Whether these obstructing structures are the upper portion of the structure under study or something of little interest, this self-shadowing can significantly reduce the image contrast by lowering the signal strength. It is particularly pronounced when observing densely packed specimens. For example, Figure 8.47 shows a confocal autofluorescence image of the chloroplast of *Closterium*. This algal

[3] This is, after all, why cells produce phase contrast.

[4] In fact, the BSL signal level is a good measure of how much the ideal optical situation has been disturbed. It is not unexpected that tissues with particularly good transparency, such as the cornea, also give very low BSL signals.

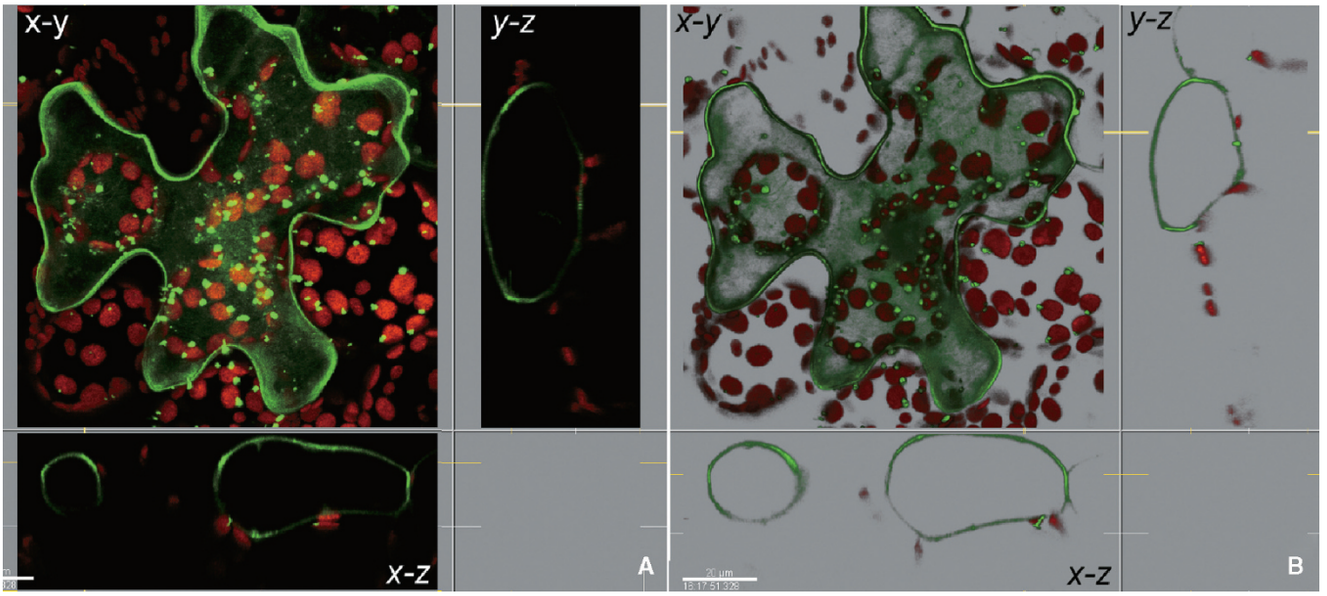

FIGURE 8.44. (A) Two-channel confocal image of epidermal cells and mesophyll cells of *A. thaliana*. The epidermal cell is GFP labeled. Note the intensity degradation in the deeper part of the tissue evident in the *xz* and *yz* sections. (B) Segmentation and α-blending can improve the visualization of the epidermal cell where it is in contact with the mesophyll cells (using Imaris software). Both *xy* projections have had top surface removed. (Image courtesy of Michael Weis, Yu Xiang, and D'Ann Rochon, Agriculture and Agri-Food Canada, PARC, Summerland, BC, Canada.)

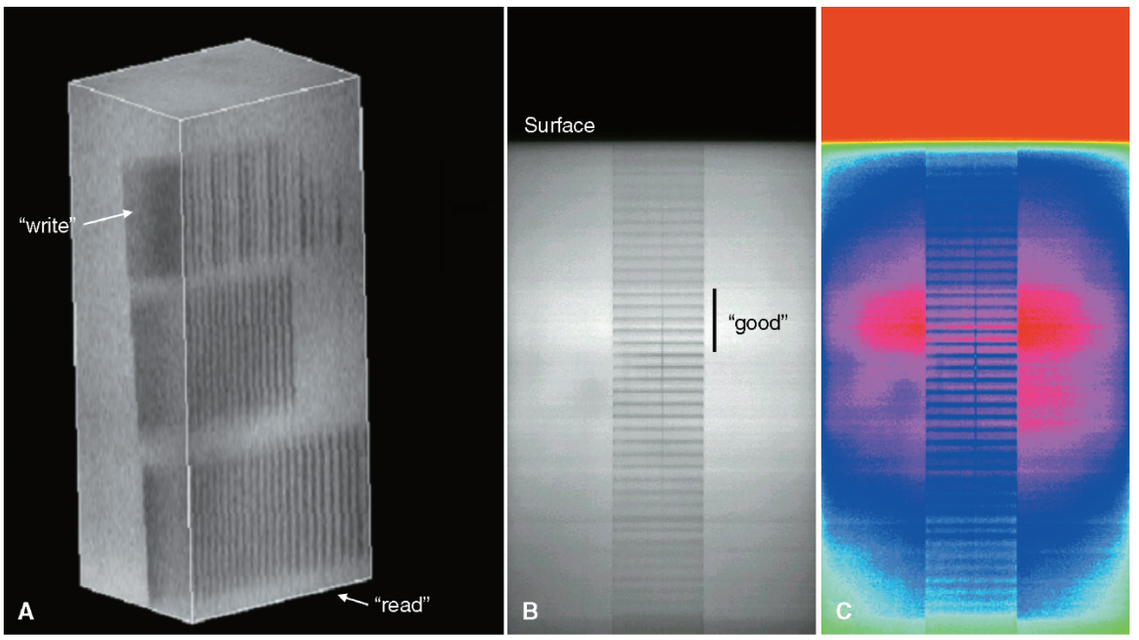

FIGURE 8.45. Two-photon bleach planes were written with equal spacing and equal intensity into a piece of fluorescent plastic (Chroma Scientific, Brattleboro, VT). After high-intensity writing, the block was re-scanned at a lower intensity to obtain an image of the photobleached pattern (A). Due to a mismatch between the RI of the plastic and the design condtions of the objective, the signal level and sharpness of the image varies significantly as a function of depth into the specimen. The best response is in the upper mid-range of the image labelled "good." At this depth, the spherical aberration caused by using this "dry" lens without a coverslip is almost compensated for by the thickness of the overlying plastic. As a result, this zone gives the best *z*-resolution (i.e., the sharpest photobleached planes) and also the highest signal intensity (B). (C) is a false-color version of (B). Although the spacing between the bleached planes seems to remain constant, this is only because, as both writing and imaging were done by the same setup, errors caused by SA-induced focal-length change cancel out (see Figs. 8.40 and 8.45).

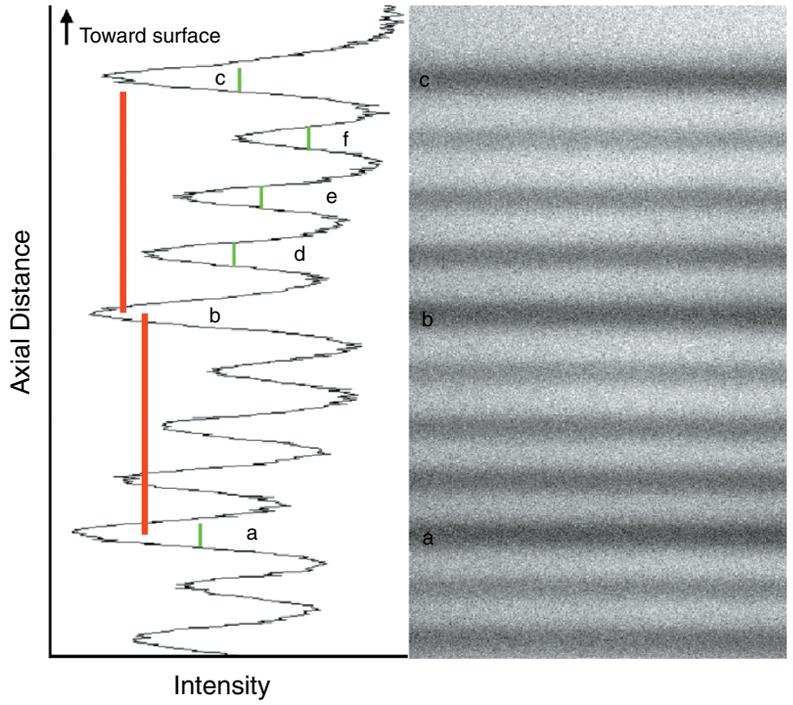

FIGURE 8.46. Two-photon bleach planes (equal *z*-spacing but with four different photobleaching intensities) were written into a fluorescent plastic block. After writing, the block was turned 90° and the surface trimmed with the glass knife on an ultramicrotome to expose the edges of the bleached planes. In a fluorescent image of this cut surface, one can see that the spacing of the bleached planes is not constant. At different depths the spacing varies because the focal length of the objective lens changes as the RI of the material between it and the focus plane changes. Compare the peak-to-peak distances between a-b and a-c, *red bars*). The FWHM of the bleached planes (i.e., the *z*-resolution) also varies (*green bars*).

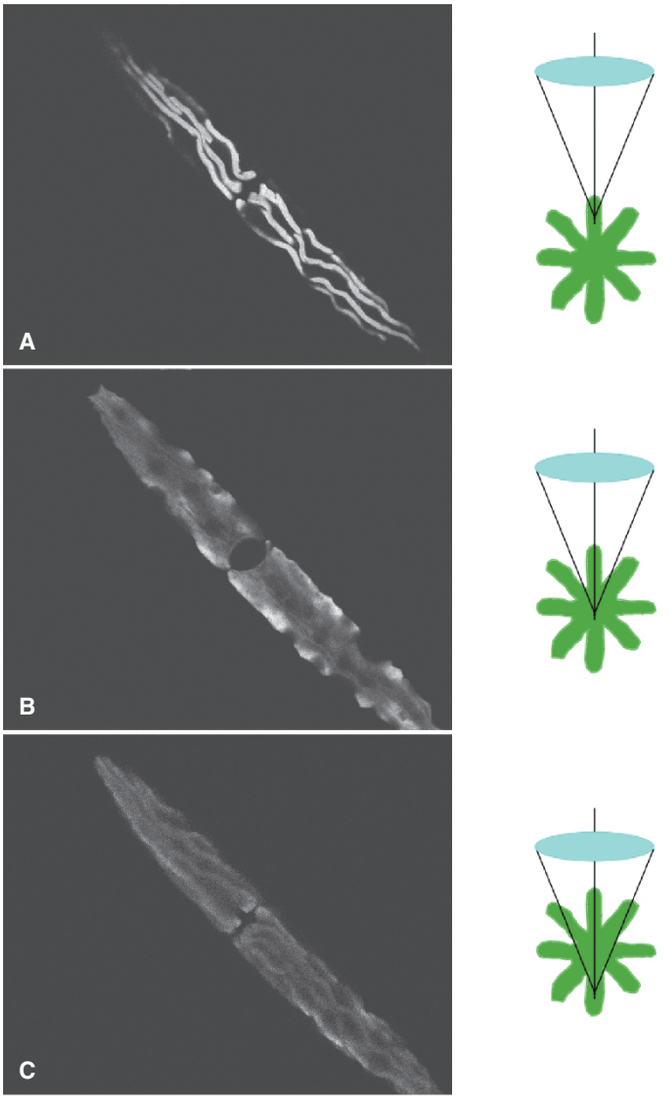

FIGURE 8.47. Self-shadowing phenomenon in epi-fluorescent mode. As the specimen attenuates both the excitation and the detected fluorescence, intensity is lower for structures located in deeper parts of the specimen. This phenomenon is particularly pronounced when the specimen is very densely stained or pigmented. (A, B, C) Epi-fluorescent confocal images of a living alga, *Closterium*. Three images were obtained under the same conditions. (A) Optical section showing chlorophyll autofluorescence near the top of the specimen, (B) from the middle of the specimen (35 µm from the top of the surface) and (C) from the bottom of the specimen (70 µm from the top of the surface). Note the reduction of the fluorescent signal (particularly in the center of the specimen where there is maximum shading).

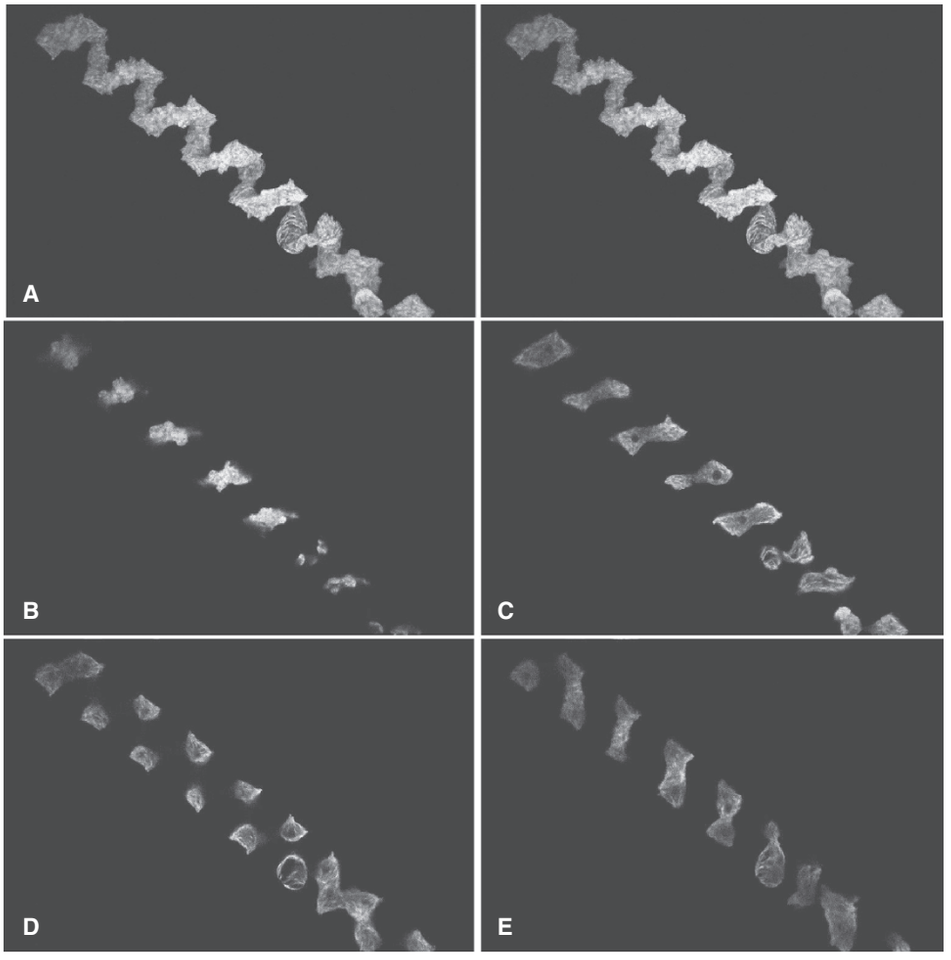

FIGURE 8.48. (A) A stereo-pair showing an epi-fluorescent confocal image of an algal cell (*Spirogyra*) with a loosely packed, autofluorescent spiral chloroplast. (B) Epi-fluorescent confocal image obtained from the top surface of the autofluorescent algal chloroplast. (C, D, E) Optical sections at various depths (20 μm, 40 μm, and 60 μm, respectively). Because of the loose packing of the chloroplasts, self-shadowing is much less than in Figure 8.41.

cell contains two chloroplasts with fin-like laminar projections that shield the lower portion of the chloroplast from excitation light [Fig. 8.46(C)]. Therefore, the images of the lower optical sections show a significant reduction in signal strength. In contrast, Figure 8.48 shows a similar auto-fluorescence image of *Spirogyra* where, because the spiral arrangement of the chloroplast minimizes self-shadowing, there is no significant drop in signal strength from the lower sections.

This self-shadowing phenomenon becomes particularly noticeable when imaging a spherical structure such as a pollen grain. Figure 8.49 is a demonstration of self-shadowing in a fluorescent latex bead. Note that both fluorescent and BS signals diminish toward the lower part of the bead. Figure 8.50 shows a mesophyll protoplast of *A. thaliana*; note the lower part of the cell cannot be imaged successively. Self-shadowing commonly occurs when imaging fixed plant tissue, as these frequently appear brown as a result of natural tannins or from the oxidized products of fixation. The absorption producing the coloration can significantly reduce the signal intensity and limit the effective optical section depth. It can often be removed by treating the tissue for 10 to 20 h in Stockwell's solution (Johansen, 1940).

Figure 8.51 shows that what should be a constant signal from a uniform fluorescent plastic is distorted by the presence of overlying material, in this case either a fluorescent 4 μm latex bead or a cell. Figure 8.52 shows that even the position at which a feature is recorded can be modified by the presence of such material (compare with and without a coverslip). In two-photon fluorescent microscopy, transparent objects that are embedded in the matrix can have similar effects (Fig. 8.53), but generally speaking, vertical shadowing is more severe with lenses of low NA than those of higher NA (Fig. 8.54) (Cheng and Cheng, 2001; Cheng *et al.*, 2002).

As biological materials such as proteins have a significantly higher absorption coefficient in the UV region than in visible light, a visually transparent specimen may pose a serious self-shadowing problem when imaged with a UV confocal microscope (Fig. 8.21 and Chapter 27, *this volume*). In contrast to tissue sections, it is important to note that, because of the absorbance and deflections produced by structures located between the lens and the focus plane, the optical sections obtained from confocal or nonlinear microscopy should not be considered to be uniformly sampled. It is important to remember this when the images are statistically analyzed.

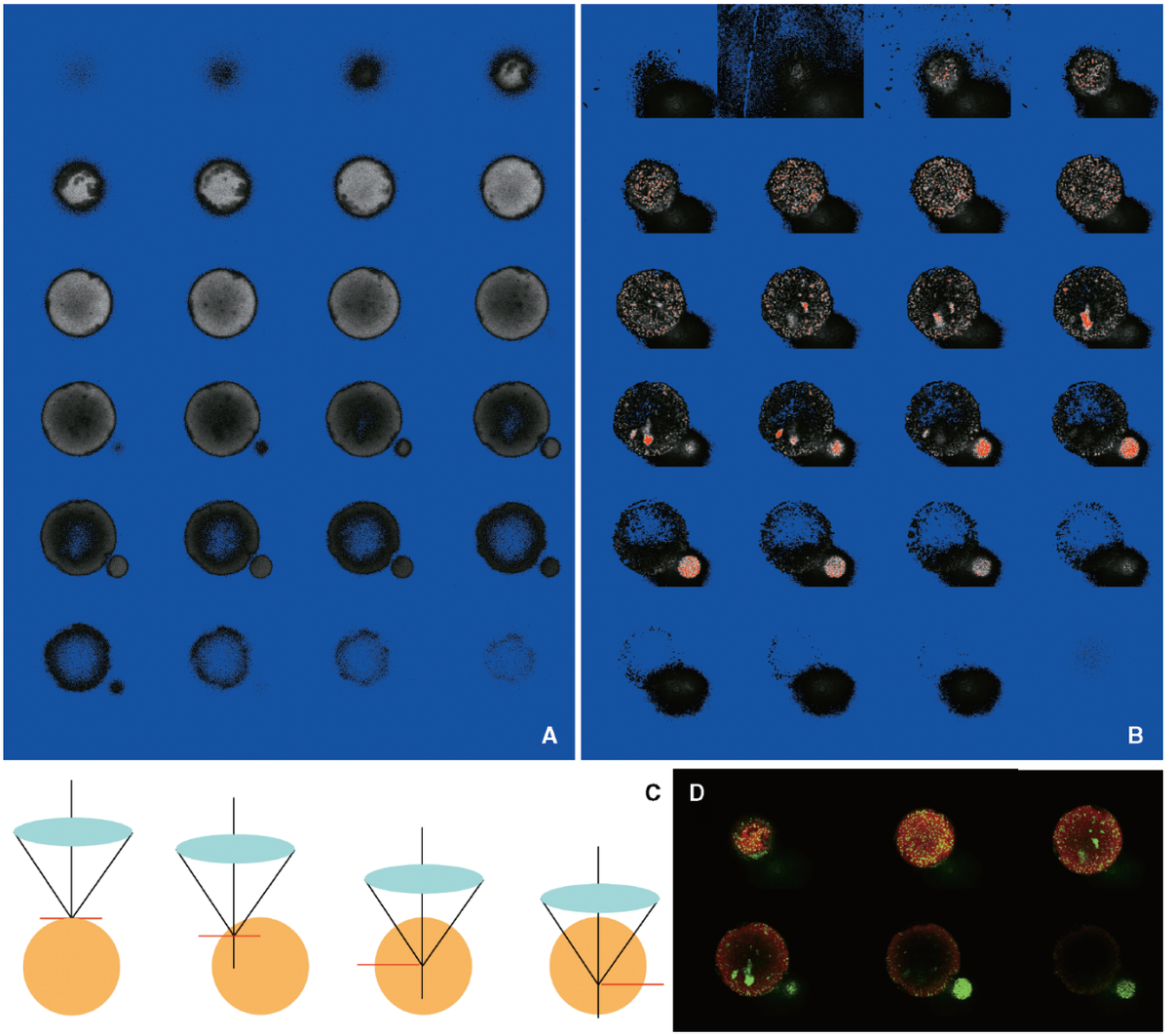

FIGURE 8.49. Fluorescence and BSL images of a latex bead. (A) Optical sections from the north hemisphere to the south hemisphere (in an upright microscope). Note the fluorescence intensity decreases as the section moves towards the southern hemisphere. The fluorescence intensity from the center of the bead also diminishes due to self-absorption of both excitation and emission light. (B) BSL image of the same bead shown in (A). The bead contains numerous "defects" that act as strong scattering centers. The color lookup table (LUT) for (A) and (B) are set as blue = 0 and 255 = red; this LUT allows one to see the base-line and saturation intensity regions in a printed document. (C) Diagrammatic representation of the geometry of the optical section series. (D) Two-channel optical sections of selective views of (A) and corresponding views in (B): green, BS image; red, fluorescent image.

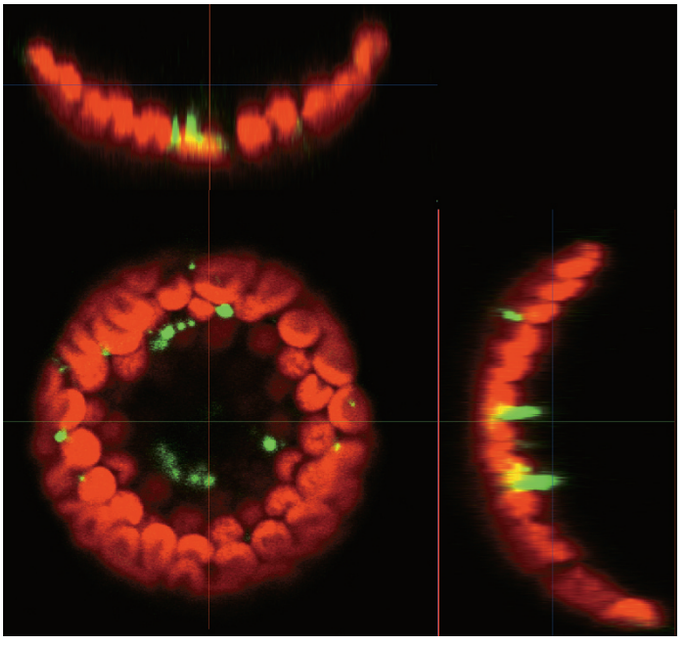

FIGURE 8.50. Confocal (*xy*) and *xz*, *yz* optical sections of a mesophyll protoplasts (*A. thaliana*) with pHBT95s::*AtTLP3*-GFP construct. Note that only half of the cell can be imaged as the self-shadowing is serious in this chloroplast-packed plant cell. (Image courtesy of Chih-Fu Yang and Jei-Fu Shaw, Institute of Plant and Microbial Biology, Academia Sinica, Taipei, Taiwan.)

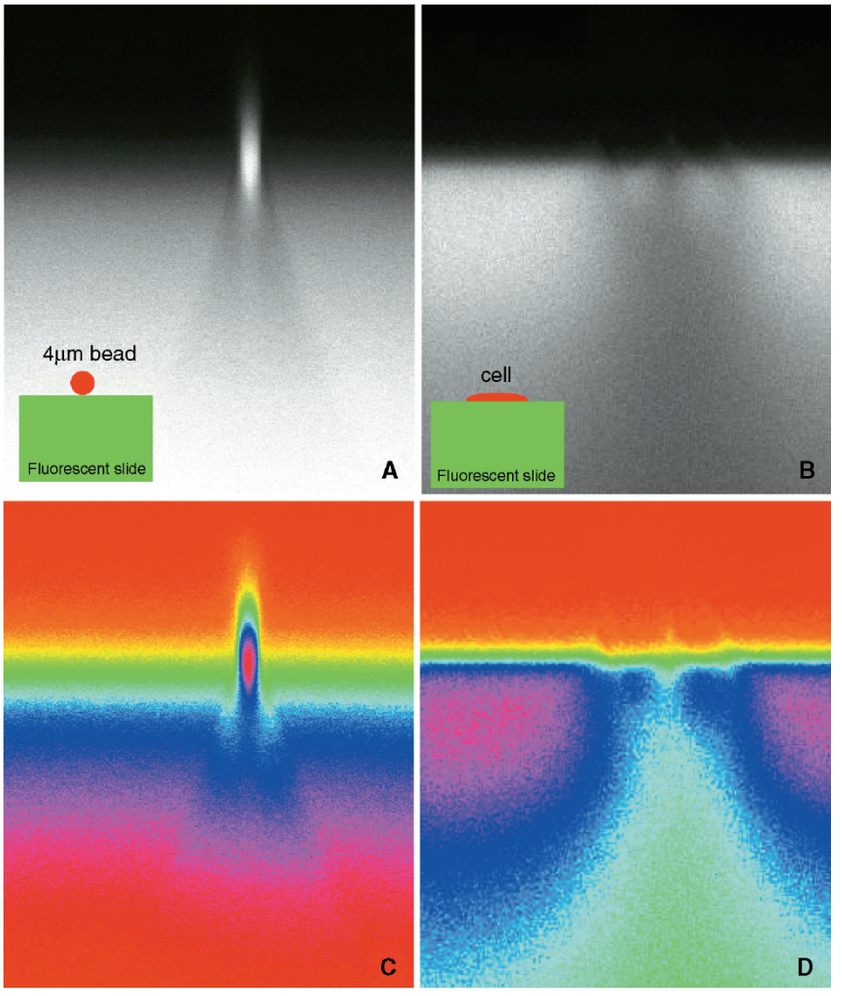

FIGURE 8.51. The effect of a latex bead and a cultured cell on the subsequent optical sections. A 4μm latex bead casts a shadow on the surface of a fluorescent slide (A), as does a cultured CHO cell (B). The inserts diagram the imaging situation in (A) and (B), respectively. (D) and (E) are false color versions of (A) and (B) that emphasize how surface structures can distort the image of the flat, plastic surface and also reduce the signal levels from locations below them.

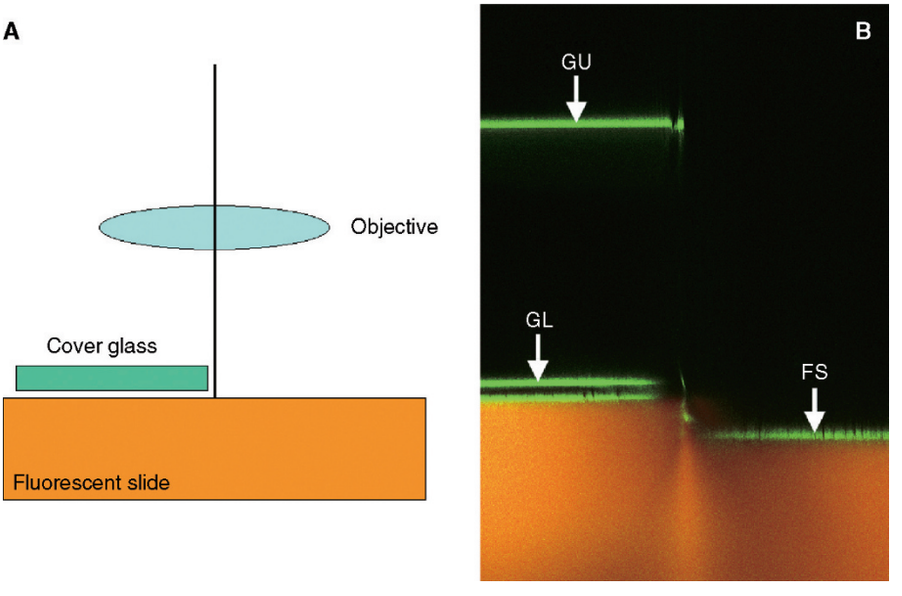

FIGURE 8.52. The effect of a coverslip on the focus position. (A) Diagram showing the imaging setup, (B) the upper and lower surfaces of the coverslip and the surface of the fluorescent plastic shows a strong reflective signal (*green*) and the fluorescent slide shows intense fluorescence (*orange*). Note the shift in focal position between the coverslip-covered and non-covered regions. The edge of the coverslip also casts a strong shadow into the plastic slide.

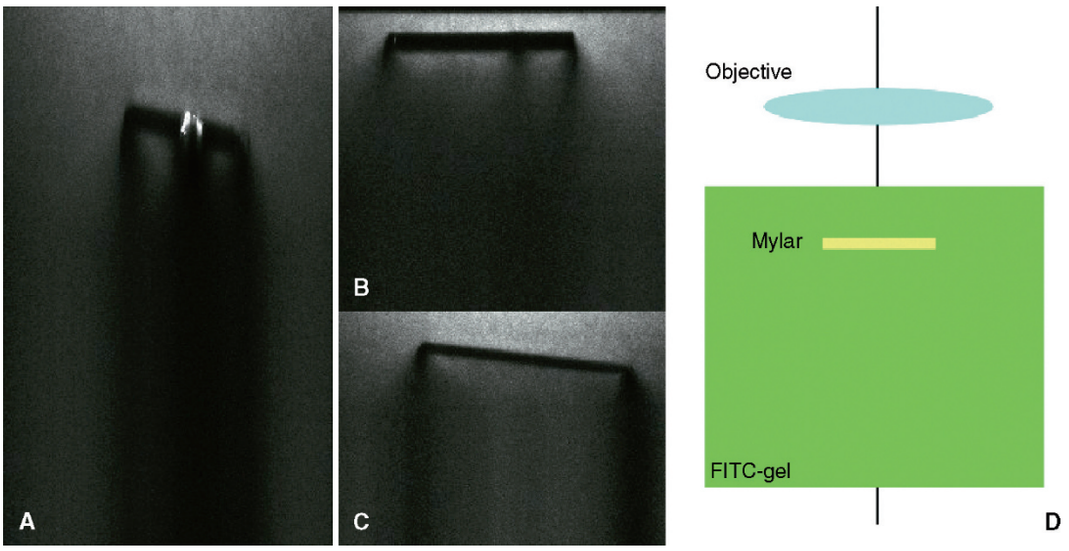

FIGURE 8.53. Self-shadowing due to RI mismatch. Minute pieces of transparent Mylar flakes suspended in a water-based FITC gel (FITC added to "Glitter," a type of cosmetic). (A–C) *xz* views of the fluorescent gel with Mylar flakes. Note the intensitity degradation under the Mylar flake, in particular near the edges. The white spots in the Mylar flake are caused by optical breakdown due to the high illumination intensity used (see also Chapter 38, *this volume*). All images are two-photon fluorescent images excited at 780 nm. (D) Diagram of the imaging situation.

Mounting Medium Selection

There is a general misconception that the confocal microscope is capable of obtaining optical sections as deep into a tissue as the working distance of the objective permits. This is seldom true, particularly if an oil-immersion lens is used to image living tissue immersed in water (Chapter 20, *this volume*, discusses this in depth). Figure 8.55 shows the degree of image degradation that can occur between optical sections obtained from the top and bottom of a glass bead. The top section is just beneath the coverslip and the bottom section is approximately 70 µm below the coverslip.

This sort of degradation is not only caused by specimens as atypical as glass beads. Figure 8.56 shows that image degradation can occur between optical sections obtained from the top and bottom of a sea urchin embryo. The top section is just beneath the coverslip and the bottom section is approximately 70 µm below the coverslip. Although this embryo had been cleared in glycerol and is very transparent, the loss of image definition is obvious in the lower section. For a detailed discussion of the media commonly used to mount plant tissue, see Cheng and colleagues (1994) and Chapter 21, and for animal tissue, see Chapter 17.

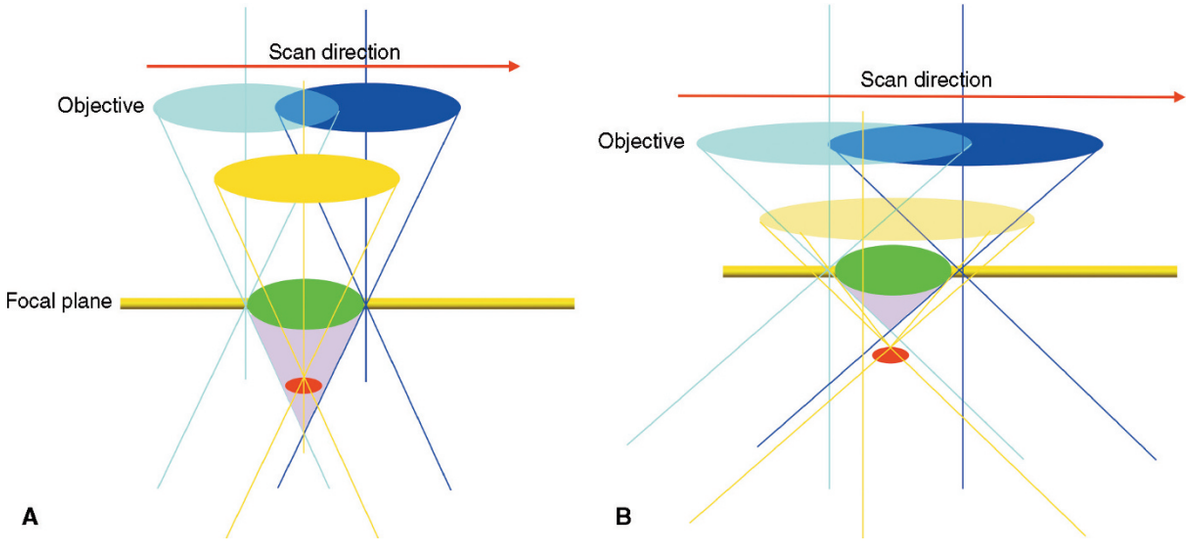

FIGURE 8.54. The effect of the NA of the objective lens on self-shadowing. (A) A small object (*red*) is included in the shadow (*magenta*) of the green object when a low-NA objective lens is used (scanning from light blue position to the dark blue position). The optical section is indicated by the yellow bar. When the objective is focused on the surface of the red object (by the yellow lens), the detecting solid-angle of the objective is not large enough to detect the fluorescence emitted. However, (B) the red object can be detected if a high NA objective is used (the yellow rays define the detectable cone of light).

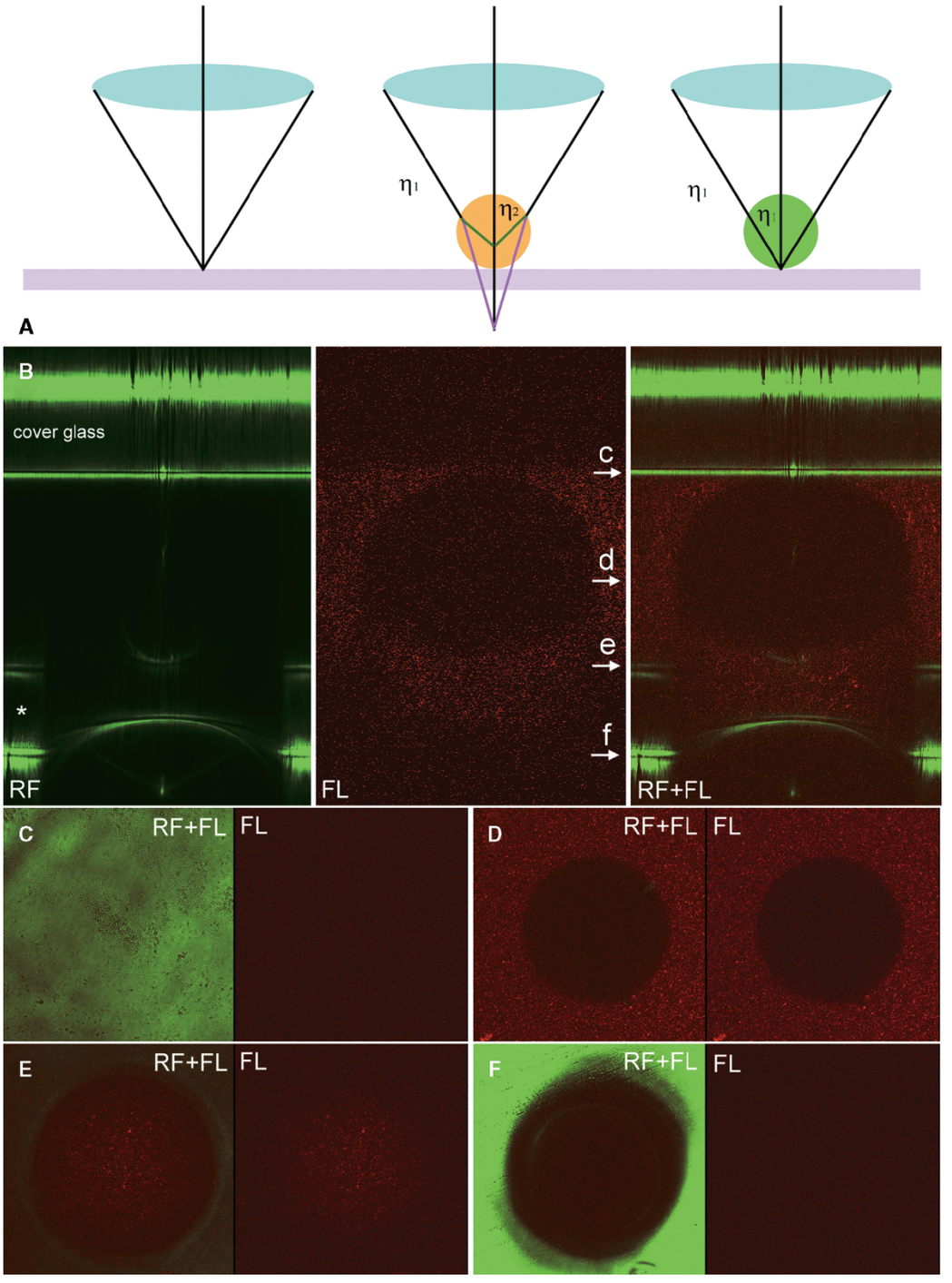

FIGURE 8.55. (A) Diagram showing the effects of a spherical structure situated between the objective lens and focal plane. (Left) The objective is focused onto a cover glass surface. (Middle) The focus plane of the objective is deviated if a spherical structure with an RI (η) different from that of the surrounding medium (η_1) is introduced into the optical path. The focus plane moves upward when $\eta > \eta_1$ (*green rays*) or downward when $\eta_- < \eta_1$ (*red rays*). (Right) When the refractive index of the spherical structure is the same as the surrounding medium (η_1), the focal plane of the objective remains on the mirror surface. (C) *xz* section showing the effect of the glass bead on the image of the lower cover glass surfaces. As an air objective lens corrected for 170 µm cover glass thickness was used, the image just below the top cover glass has the best resolution. (C–E) Series of confocal images of the surface of a cover glass on which a glass sphere ($\eta = 1.53$) was suspended in water ($\eta = 1.33$) with a trace of red fluorescent dye. [Green, reflective (RF); red, fluorescence (FL).] If the glass sphere is suspended in immersion oil ($\eta = 1.53$), the RIs of the glass bead and "mounting medium" now match, the glass surface under the glass bead remains in focus with the surrounding glass surface.

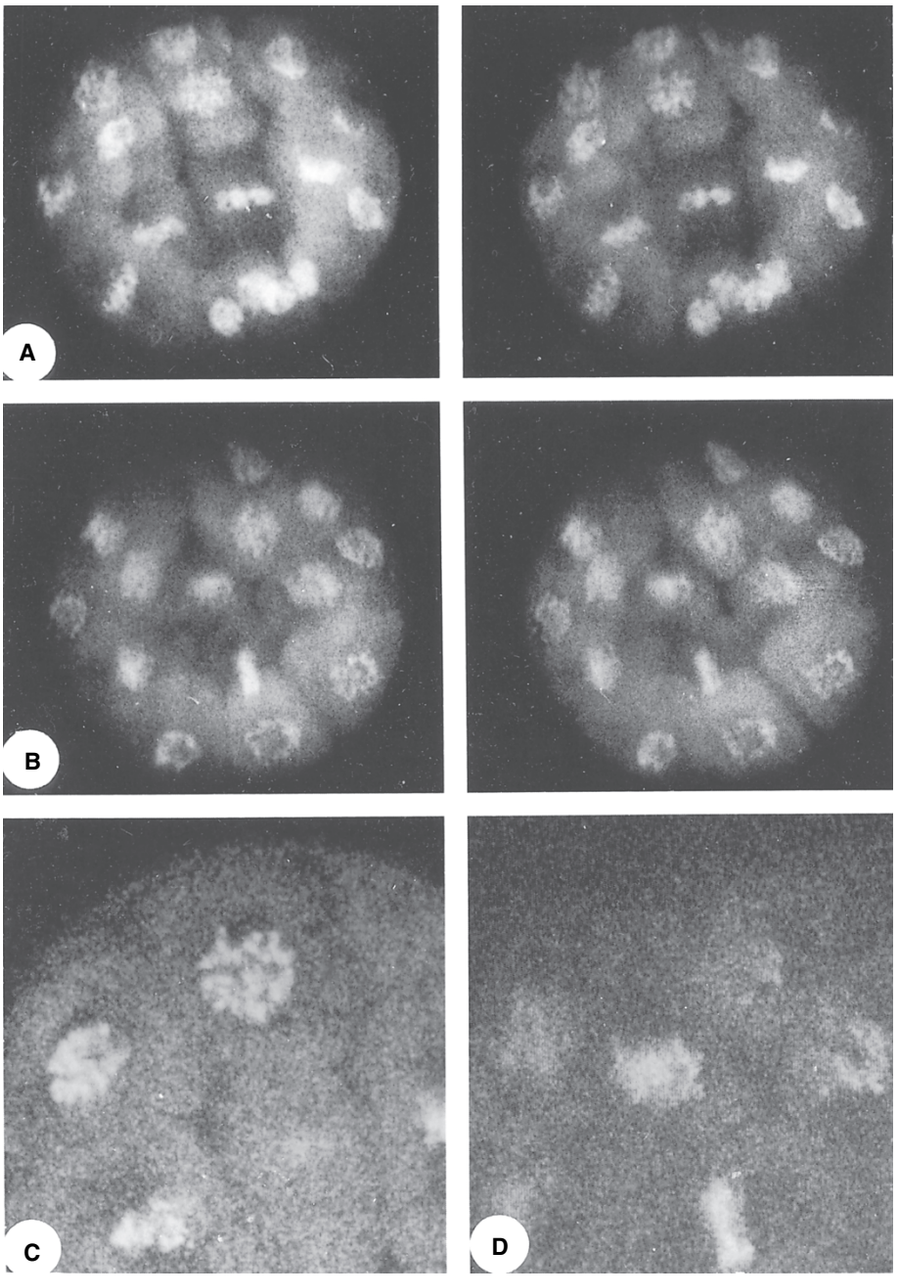

FIGURE 8.56. Two stereo-pairs showing the top half (A) and bottom half (B) of a sea urchin embryo (*Strongylocentrotus purpuratus*). Note the deterioration of image definition in the lower half. The specimen was Feulgen stained, cleared in glycerol, and scanned for 16 s on each of 15 sections using a Bio-Rad MRC 500 operating at 514 nm, full power with a Nikon 40×, NA 1.3 Fluor lens. The *S. purpuratus* embryo [80 µm diameter is less transparent than the species *Lytechinus variegatus* shown in Fig. 8.27(C)]. An optical section obtained from the top of the embryo (10 µm deep). (D) An optical section obtained from 70 µm deep. (Specimen courtesy of Dr. R. Summers, Department of Anatomical Sciences, State University of New York at Buffalo.)

ARTIFICIAL CONTRAST

Contrast Resulting from Instrument Vibration and Ambient Lighting

Vibrations resulting from the mechanical scanning systems of confocal microscopes and/or vibrations from external sources can have a serious negative effect on image contrast because they can alter the position of the specimen relative to the focal plane of the objective lens (Overington, 1976).

Interference from room light can also have a drastic effect on the recorded image. Room light scattered by the specimen and entering the detecting system can increase the DC background level as well as make moiré patterns between the AC component from the fluorescent lights and the pixel clock of the digitizer. Figure 8.57 shows the effect of AC components resulting from fluorescent room light. It is important to note that, especially when using an inverted microscope for either a widefield or multi-photon fluorescence with non-descanned detection, the specimen should be covered with a dark cup and the room should be kept in almost total darkness.

Vibration-induced variations in the relative positions of the pinholes can cause similar artifacts, degrading the effective resolution of the confocal imaging system. Figure 8.53 shows the effects of mechanical vibration on a confocal image of a dirty first-surface mirror. The image shows vibration contrast due to poor mechanical isolation from the building vibration (Fig. 8.58). An actively isolated optical bench can significantly improve the situation. Instability in the pointing direction of the laser (Chapter 5, *this volume*) can also contribute artificial contrast to the image, and laser intensity variations can introduce complex moiré patterns in signals recorded in a single-beam system.

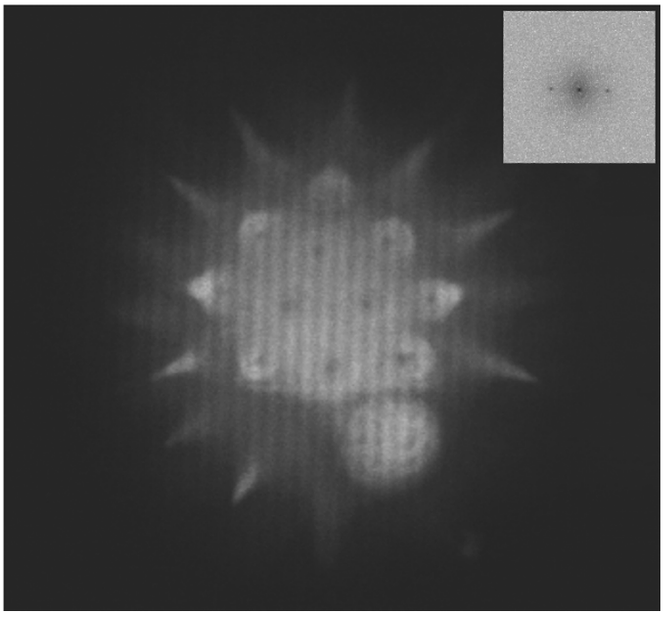

FIGURE 8.57. AC components in a confocal image resulting from fluorescent lights in the laboratory. Insert: Fourier power spectrum of the image showing spots related to the AC frequency.

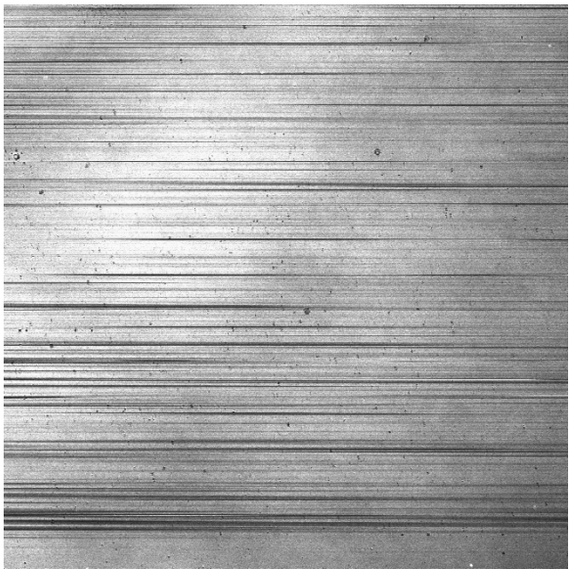

FIGURE 8.58. The effect of mechanical vibration on the confocal reflection image of a cover glass surface.

Contrast Resulting from Interference of Cover Glass Surfaces

Interference can also introduce spurious contrast into the recorded data. Figure 8.59 shows three confocal images (and their Fourier transforms) recorded from a focus plane located near the surface of a coverslip on which an *A. thaliana* seedling was resting. Patterns generated by the interference of light reflected from the two surfaces of the cover glass are clearly visible in the reflection image (489 nm) collected in a channel near the excitation wavelength (488 nm) [Fig. 8.59(A,D)]. However, this reflective light can still be detected in the 500 nm channel of the Zeiss 510 Meta system as shown in the Fourier transform of the fluorescence image [Fig. 8.59(B,E)]; since the cover glass surface reflection is much more intense than the fluorescence of the specimen, this signal is actually the scattered light leaking through the microscope monochrometer system. The spots are not visible in the image collected at 703 nm because the detecting channel is far away from the 489 nm [Fig. 8.59(C,F)]. Using the Fourier transform in this way provides a very sensitive test for the leakage of excitation light into the detector channels. One focuses the microscope on the surface of a cover glass to obtain an interference pattern and records the image in all the spectral channels in a normal way. Then examine the power spectrum of each image to determine if specific diffraction spots corresponding to the frequency of the interference pattern are present.

Background Level and Ghost Images from the Transmission Illuminator

Because the confocal microscope has high resolution along the *z*-axis, it can be very difficult to locate areas of interest if one searches in the confocal mode. Therefore, initial searching is generally done using conventional bright-field or widefield epi-fluorescence microscopy. Once an area of interest has been identified, one switches to confocal mode by redirecting the imaging path to the confocal scanning/detecting unit and by blocking the optical path from the trans-/epi-illuminator. However, if one

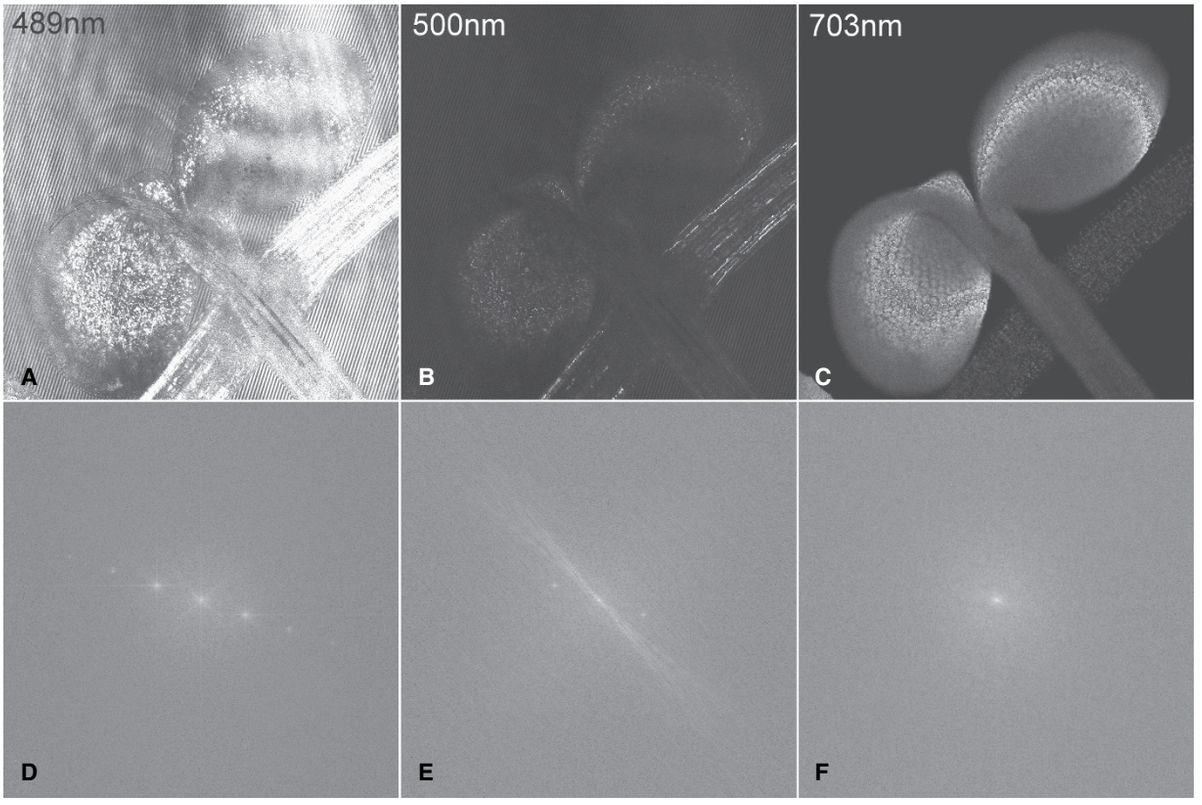

FIGURE 8.59. A young seeding of *A. thaliana* was placed in water under a cover glass and imaged at 488 nm using a Zeiss 510 META confocal microscope. (A) 489 nm channel shows strong backscattered light from the specimen and the surface of cover glass. Interference fringes are clearly visible. (B) 500 nm channel shows low intensity of autofluorescence. (C) 703 nm channel shows autofluorescence of chlorophylls. (D) Fast Fourier transform (FFT) of (A) shows the diffraction spots resulting from the interference fringes. (E) Even though there are no visible interference fringes in (B), its FFT indicates a significant amount of 488 nm illumination contamination in the image. (F) FFT of (C). (Specimen courtesy of Shu-Hsing Wu, Institute of Plant and Microbial Biology, Academia Sinica, Taipei, Taiwan.)

forgets to block the light from the conventional illuminator, some of it will reach the detector, producing excessive background. Depending on the spectral output of the illuminator, different fluorescence channels will record particular background levels. In an extreme case, when the specimen is relatively opaque, a ghost image may form.

Figure 8.60 shows a pollen grain of maize stained with periodic-acid Schiff (PAS) reagent for starch. The trans-illuminator was turned on at low intensity during the confocal scanning. The substage condenser was purposely misaligned off the optical axis to emphasize the ghost image effect. Note that the confocal fluorescence image of the pollen grain shows only the periphery of the pollen grain as a result of self-shadowing. However, the non-confocal transmitted-light ghost image (arrows) simply shows the shadow of the pollen grain. Therefore, it is important to turn off the trans-illuminator/epi-illuminator of the microscope during confocal observation as even a low glow can add significantly to the background level and produce complex image features that confuse interpretation.

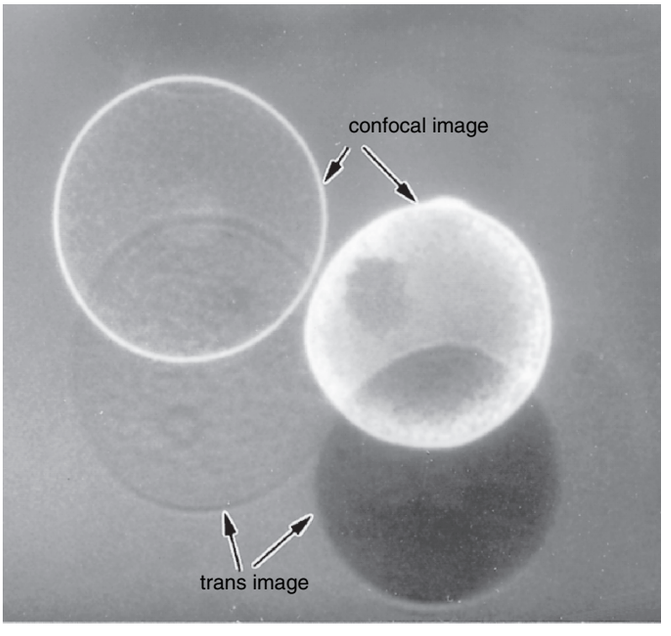

FIGURE 8.60. An epi-fluorescence confocal image of a pollen grain of maize stained with PAS. Due to the abundance of starch granules, the pollen was deeply stained. During the image acquisition, the substage illuminator was purposely turned on and misaligned to demonstrate the effect of a "ghost" image.

Contrast Resulting from Differences in Photobleaching Dynamics

Because different fluorophores in a multi-labeled specimen often photobleach at different rates, photobleaching that occurs while recording a series of optical sections can cause the first section to have a different spectral balance from the last. This complicates

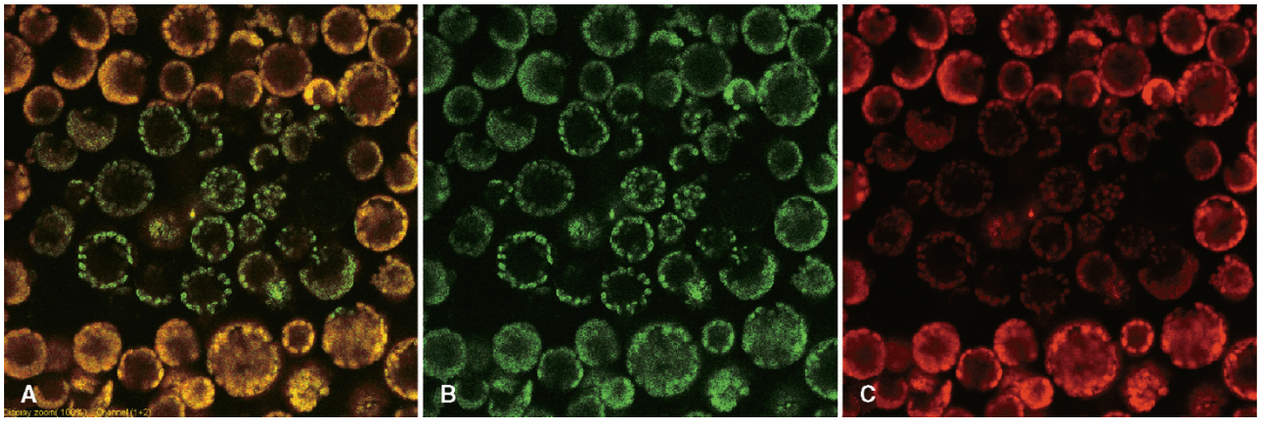

FIGURE 8.61. Photobleaching in the mesophyll protoplasts of *A. thaliana* by 780 nm NIR (A). Note that the green autofluorescence (B) bleaches more slowly than does the red autofluorescence (C) caused by chlorophyll.

any effort to correct for bleaching or for the signal loss that occurs as the *z*-stack penetrates farther into the specimen. Figure 8.61 is a dual-channel recording of mesophyll protoplasts of *A. thaliana*. It shows that the red fluorescence (chlorophylls) and the green autofluorescence photobleach at very different rates and, therefore, that bleach rate must be considered as a contrast parameter when imaging such specimens.

Effect of Spectral Leakage and Signal Imbalance Between Different Channels

The spectral resolution of the detection system is an important factor controlling image contrast in fluorescence microscopy. Poor spectral resolution, caused either by leakage and poor cut-off sharpness in the filter system (see Chapter 3, *this volume*), the spectral response of detector(s), or variations in the transmittance or properties of the optics can have a pronounced impact on image contrast and S/N.

A significant imbalance in image intensity among different detection channels in a multi-channel setup can have a serious impact on the spectral purity of the final image. If, in a typical specimen, labeled with fluoroscein-isothiocyanate and rhodamine (FITC-Rh), the concentration of FITC is significantly higher than that of Rh, then given equal excitation, the FITC will emit much more fluorescence than the Rh. Even 0.1% leakage of stray FITC light through the dichroic mirror and barrier filters into the Rh channel can contribute significantly to the detected signal. Clearly, any imbalance noted between two fluorescence channels may be due not to a difference in the concentration of the two fluorescent dyes but to an imbalance in their fluorescence efficiency with respect to the spectral bandwidth and blocking efficiency of the excitation and emission filters used. For example, attempts to view a specimen labeled with balanced amounts of FITC and Rh but excited using only the 488-nm line of an argon-ion laser will result in a very poor signal in the Rh channel. The use of dual excitation wavelengths (488 and 568 nm) from a krypton/argon laser can reduce this problem.

A simple plot of the pixel-by-pixel correlation between the intensity values detected in each channel can reveal possible cross-talk. Figure 8.62 shows such a plot between two fluorescence channels recorded from a FITC-labeled specimen, excited at 488 nm.

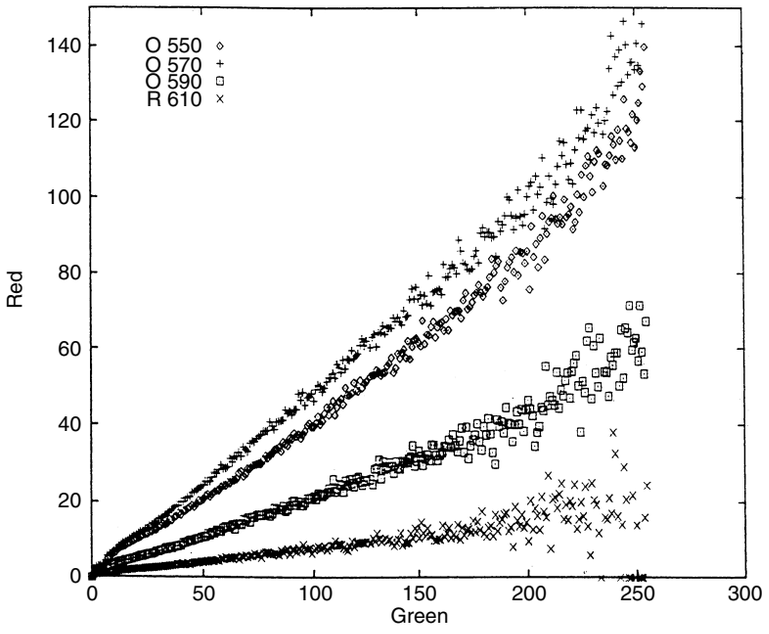

FIGURE 8.62. Spill-over from the FITC channel (*green*) to the rhodamine channel (*red*) for different low-pass filters.

The two channels were separated using a 570 nm dichroic beamsplitter; a 535 nm bandpass filter was used for channel 1 and various long-pass filters ranging from 570 to 610 nm were used for channel 2. Note that the correlation line decreases in slope as the cut-on wavelength of the barrier filter increases and the amount of excitation light reaching the detector is reduced.

NEW CONTRASTS: FLUORESCENCE LIFETIME AND COHERENT ANTISTOKES RAMAN SPECTROSCOPY

Since the second edition of the volume, the use of confocal contrast based on the fluorescence lifetime (FLIM) has become much more common. While this is partially because the equipment needed to record it is now commercially available, to an even greater extent it is because it seems that FLIM may be the best way to obtain a quantitative measure of FRET in living cells (Fig. 8.63). Chapter 27 explores this exciting new modality in more depth.

Although Raman microscopy had been available for some time, the chemical specificity it offers was only available at the cost of having to use relatively high illumination power while having to accept sensitivity so low that it was useless for detecting most biological molecules at the concentrations likely to be found in biological specimens. More recently, developments in laser technology have made coherent antistokes raman spectroscopy (CARS) a realistic contrast mode for 3D microscopy (Fig. 8.64). This new technique has better chemical sensitivity than normal Raman microscopy and requires less laser power to strike the specimen. Chapter 33 provides more details.

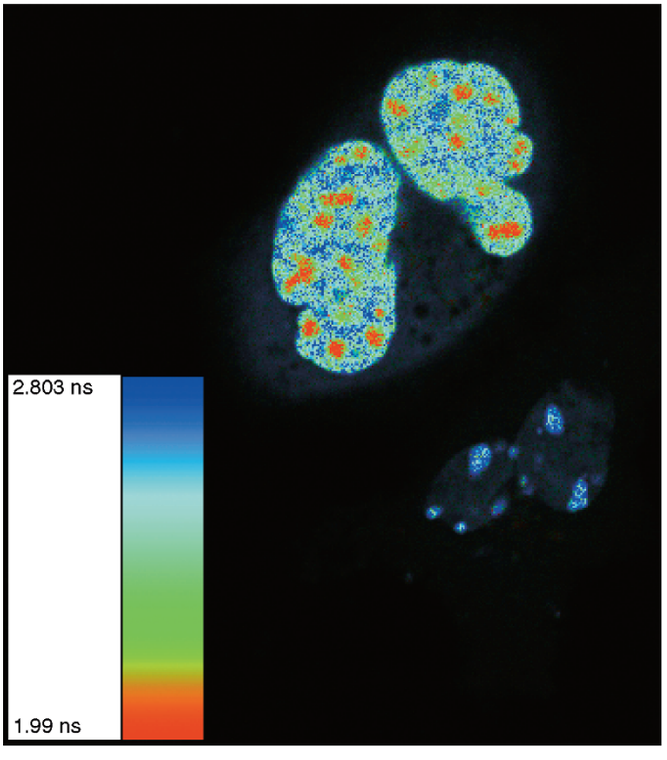

FIGURE 8.63. The FLIM images are color coded and overlaid on an intensity image. Blue represents short lifetime and red represents long lifetimes. The image was taken with an Olympus FV1000 with fiber output coupling to a PicoQuant FLIM system and a 405 nm pulsed laser was used for illumination. The sample is a living cell expressing cyan fluorescent protein (CFP) and yellow fluorescent protein (YFP). In the image, there are four cells. Two of them demonstrate FRET, as is shown by the blue color. (Image provided by Yiwei Jia of Olympus and Uwe Ortmann of PicoQuant; the image was taken at the University of Virginia FRET microscopy course.)

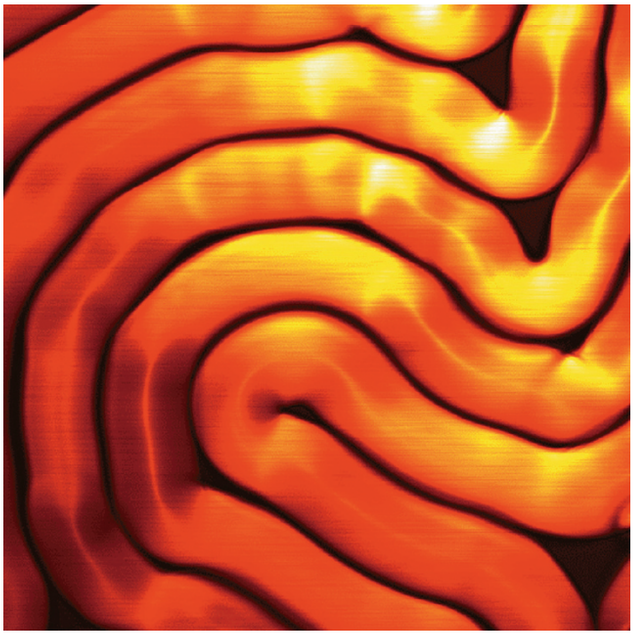

FIGURE 8.64. CARS Image of lecithin myelin figures using modified Olympus FV300 confocal system. ωp-ωs is tuned to the CH_2 symmetric stretch vibration at 2,838 cm^{-1}. This image shows that the myelin core is not composed of pure water but is enriched in lecithin. (Provided by Ji-Xin Cheng, Weldon School of Biomedical Engineering, Purdue University.)

Finally, although until recently, one usually viewed the electrical state of excitable cells indirectly by sensing Ca^{++}, there have long been membrane-incorporated or membrane-translocating fluorescent dyes that change their fluorescent output with membrane potential (Zochowski *et al.*, 2000). Recently, the combination of a disk-scanning microscope with an electron-multiplying CCD camera has provided the researcher with a method of detecting the electrical state directly and on a time scale almost fast enough to measure transients that are physiologically significant (Fig. 8.65).

SUMMARY

Image contrast mechanisms in confocal microscopy depend on a number of variables, many of which have been presented in this chapter. The acquisition parameters of the imaging system should be adjusted to emphasize to the signals carrying the information required and these adjustments must also take into account the characteristics of the specimen, and the image processing method to be used. To observe detailed structures with the appropriate contrast requires careful preparation of the specimen, and this depends in turn on an understanding of its chemical and physical properties.

In order to improve the visibility of structures in 3D while minimizing unwanted artifacts, the parameters needed for proper

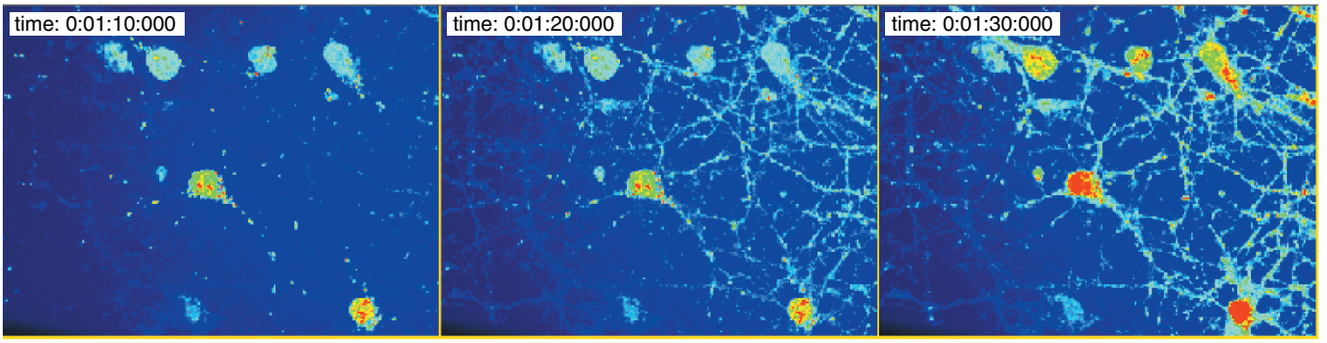

FIGURE 8.65. Cultured rat hippocampal neurons loaded with $DiSBAC_2(3)$, a voltage sensitive, membrane-translocating dye, and imaged with an Andor Revolution 488. Twenty 100 ms exposures on the iXon 887BV EM-CCD were obtained for each *z*-stack, using an EM Gain of 200. The last frame was taken almost simultaneously with the addition of 100 m*M* KCl, which depolarizes the cells and shows a near instantaneous rise in the $DiSBAC_2(3)$ signal. The change in signal is ~45%. (Image provided by Iain Johnson, Molecular Probes/Invitrogen, Eugene, Oregon, and Mark Browne, Andor, South Windsor, Connecticut.)

volume rendering must be properly selected (particularly, Nyquist sampling in *x*, *y*, *z*, and *t*). Improving the quality of the confocal data should always be the first goal. This includes maximizing the dynamic range of the recording system, the contrast between the structure of interest, and the background and the S/N of the recorded data.

ACKNOWLEDGMENTS

Most of the images presented in this chapter were obtained at the author's laboratories at the State University of New York at Buffalo and at the National University of Singapore (NUS) where he is a part-time professor of the Department of Biological Sciences (DBS). The author is grateful for the wonderful support and friendship from Professor Hew Choy Leong, Head of DBS-NUS and Professor Hanry Yu (Department of Physiology, NUS) during his 2003 and 2004 stay. The SHG work is a collaboration with Professor Chi-kuang Sun of the Department of Electrical Engineering, National Taiwan University, Taipei, Taiwan. Some of the images used in this chapter were obtained by the author in demonstration experiments at the International 3D Microscopy of Living Cell Course (organized by Professor J. Pawley) held annually at the University of British Columbia, Canada. Special thanks to Dr. T. Holmes at AutoQuant for providing the Auto-Deblur deconvolution software, to Drs. M. and D'A. Weis, Agriculture Canada, Summerland, British Columbia, Canada, for Figures 8.10 and 8.44, to Dr. A. Periasamy, University of Virginia, Charlottesville, Virginia, for Figures 8.34 through 8.36, and to Iain Johnson (Molecular Probes/Invitrogen, Eugene, OR) and M. Browne (Andor, South Windsor, CT) for Figure 8.65.

REFERENCES

An, J.J., Goodman, M.B., and Schwartz, E.A., 1990, Simultaneous fluorescent and transmission laser scanning confocal microscopy, *Biophys. J*. 59:155a.

Barad, Y., Eisenberg, H., Horowitz, M., and Silberberg, Y., 1997, Nonlinear scanning laser microscopy by third-harmonic generation, *App. Phys. Lett.* 70:922–924.

Barr, M.L., and Kieman, J.A., 1988, *The Human Nervous System — An Anatomical Viewpoint*, 5th ed., Lippincott, London, p. 17.

Born, M., and Wolf, E., 1980, *Principles of Optics*, 6th ed., Pergamon Press, Oxford.

Boyde, A., 1985, The tandem scanning reflected light microscope. Part II. Pre-Micro'84 application at UCL, *Proc. RMS* 20:131–139.

Carminati, R., and Greffet, J.J., 1995a, Two-dimensional numerical simulation of the photon scanning tunneling microscope. Concept of transfer function, *Opt. Commun.* 116:316–321.

Carminati, R., and Greffet, J., 1995b, Influence of dielectric contrast and topography on the near field scattered by an inhomogeneous surface: Boundary conditions for diffusion of light, *J. Opt. Soc. Am. A* 12:2716.

Carney, P., and Schotland, J., 2001, Three-dimensional total internal reflection microscopy, *Opt. Lett.* 26:1072.

Chen, I.-H., Chu, S.-W., Sun, C.-K., Lin, B.-L., and Cheng, P.C., 2002, Wavelength dependent damage in biological multi-photon confocal microscopy: A micro-spectroscopic comparison between femtosecond Ti:Sapphire and Cr:Forsterite laser sources, *Opt. Quantum.* 34(12):1251–1266.

Chen, V.K.-H., and Cheng, P.C., 1989, Real-time confocal imaging of Stentor coeruleus in epi-reflective mode by using a Tracer Northern Tandem scanning microscope, *Proc. 47th Annual Meeting EMSA* 47:138–139.

Chen, Y., Mills, J.D., and Periasamy, A., 2003, Protein interactions in cells and tissues using FLIM and FRET, *Differentiation.* 71:528–541.

Cheng, P.C., and Cheng, W.Y., 2001, Artifacts in confocal and multi-photon microscopy, *Microsc. Microanal*. 7:1018–1019.

Cheng, P.C., and Kriete, A., 1995, Image contrast in confocal light microscopy, In: *Handbook of Biological Confocal Microscopy* (J.B. Pawley, ed.), Plenum Press, New York, pp. 281–310.

Cheng, P.C., and Lin, T.H., 1990, The use of computer-controlled substage folding optics to enhance signal strength in fluorescent confocal microscopy, *Trans. Roy. Micros. Soc*. 1:459–642.

Cheng, P.C., Chen, V.H.-K., Kirn, H.G., and Pearson, R.E., 1989, An epi-fluorescent spinning-disk confocal microscope, *Proc. 47th Annual Meeting EMSA* 47:136–137.

Cheng, P.C., Hibbs, A.R., Yu, H., and Cheng, W.Y., 2002, An estimate of the contribution of spherical aberration and self-shadowing in confocal and multi-photon fluorescent microscopy, *Microsc. Microanal*. 8:1068–1069.

Cheng, P.C., Pareddy, D.R., Lin, T.H., Samarabandu, J.K., Acharya, R., Wang, G., and Liou, W.S., 1994, Confocal microscopy of botanical specimens, In: *Multidimensional Microscopy* (P.C. Cheng, T.H. Lin, W.L. Wu, and J.L. Wu, eds.), Springer-Verlag, Berlin, pp. 339–380.

Cheng, P.C., Sun, C.-K., Kao, F.-J, Lin, B.L., and Chu, S.-W., 2001, Nonlinear multi-modality spectro-microscopy: Multiphoton fluorescence, SHG and THG of biological specimen, *SPIE Proc*. 4262:98–103.

Cheng, P.C., Sun, C.K., Lin, B.L., Chu, S.W., Chen, I.S., Liu, T.M., Lee, S.P., Liu, H.L., Kuo, M.X., and Lin, D.J., 2002, Biological photonic crystals — Revealed by multi-photon nonlinear microscopy, *Microsc. Microanal.* 8:268–269.

Cheng, P.C., Sun, C.K., Cheng, W.Y., and Walden, D.B., 2003, Nonlinear biophotonic crystal effect of opaline silica deposits in maize, *J. Scanning Microsc.* 235:80–81.

Chu, S.W., Chen, I.S., Li, T.M., Lin, B.L., Cheng, P.C., and Sun, C.K., 2001, Multi-modality nonlinear spectral microscopy based on a femtosecond Cr:forsterite laser, *Opt. Lett.* 26:1909–1911.

Chu, S.W., Chen, I.-S., Liu, T.-M., Sun, C.-K., Lin, B.-L., Lee, S.-P., Cheng, P.C., Liu, H.-L., Kuo, M.-X., and Lin, D.-J., 2003, Nonlinear bio-photonic crystal effects revealed with multi-modal nonlinear microscopy, *J. Microsc.* 208:190–200.

Cogswell, C.J., 1994, High resolution confocal microscopy of phase and amplitude objects, In: *Multidimensional Microscopy* (P.C. Cheng, T.H. Lin, W.L. Wu, and J.L. Wu, eds.), Springer-Verlag, Berlin, pp. 87–102.

Deng, Y., Marko, M., Buttle, K.F., Leith, A., Mieczkowski, M., and Mannella, C.A., 1999, Cubic membrane structure in amoeba (*Chaos carolinesis*) mitochondria determined by electron microscopy tomography, *J. Struct. Biol.* 127:231–239.

Holmes, T., and Cheng, P.C., 2005, Basic principles of imaging, In: *Multi-Modality Microscopy* (H. Yu, P.C. Cheng, P.C. Lin, and F.J. Kao, eds.), World Scientific Publishing, in press.

Johansen, D.A., 1940, *Plant Microtechnique*, McGraw-Hill, New York.

Oldenbourg, R., 2004, Polarization microscopy with the LC-PolScope, In: *Live Cell Imaging: A Laboratory Manual* (D.L. Spector and R.D. Goldman, eds.), Cold Spring Harbor Laboratory Press, Cold Spring Harbor, New York, pp. 205–237.

Overington, J., 1976, *Vision and Acquisition*, Pentech Press, London.

Paddock, S.W., 1989, Tandem scanning reflected-light microscopy of cell-stratum adhesions and stress fibers in Swiss 3T3 cells, *J. Cell. Sci.* 93:143–146.

Patterson, G., and Lippincott-Schwartz, J., 2002, A photoactivatable GFP for selective photolabeling of proteins and cells, *Science.* 297:1873–1877.

Prieve, D.C., and Walz, J.Y., 1993, The scattering of an evanescent surface wave by a dielectric sphere in total internal reflection microscopy, *Appl. Opt*. 32:1629.

Reits, E.A., Neefjes, J.J., 2001, From fixed to FRAP: Measuring protein mobility and activity in living cells, *Nat. Cell Biol.* 3(6):E145–147.

Rose, A., 1948, Television pickup tubes and the problem of noise, *Adv. Electron* 1:131.

Scheibel, M.E., and Scheibel, A.B., 1970, The rapid Golgi method. Indian summer or renaissance? In: *Contemporary Research Methods in Neuroanatomy* (W.J.H. Nauta and S.O.E. Ebbeson, eds.), Springer-Verlag, New York, pp. 1–11.

Sharonov, S., Morjani, H., and Manfait, M., 1992, Confocal spectral imaging analysis: A new concept to study the drug distribution in single living cancer cell, *Anticancer Res*. 12:1804.

Sheppard, C.J.R., 1993, Confocal microscopy: Basic principles and system performance, In: *Multidimensional Microscopy* (P.C. Cheng, T.H. Lin, W.L. Wu, and J.L. Wu, eds.), Springer-Verlag, Berlin, pp. 1–31.

Shinozaki, D.M., Cheng, P.C., Haridoss, A., and Fenster, A., 1991, Three dimensional optical microscopy of water trees in polyethylene, *J. Mater. Sci.* 26:6151–6160.

Shinozald, D.M., Klauzner, A., and Cheng, P.C., 1991, Inelastic deformation of polyimide-copper thin films, *Mater. Sci. Eng. A* 142:135–144.

Shribak, M., and Oldenbourg, R., 2003, Techniques for fast and sensitive measurements of two-dimensional birefringence distributions, *Appl. Opt.* 42:3009–3017.

Sun, C.K., 2005, *Abstract of Focus on Microscopy*, Jena, Germany.

Sun, C.K., Huang, Y.C., Liu, H.C., Lin, B.L., and Cheng, P.C., 2001, Cell manipulation using diamond microparticles as optical tweezers handles, *J. Opt. Soc. Amer. B*, 18(10):1483–1489.

Tsou, C.-H., and Fu, Y.L., 2002, Pollen tetrad formation in *Annona* (Annonaceae): Proexine formation and binding mechanism, *Am. J. Botany* 89:734–747.

Van Labeke, D., Barchiesi, D., and Baida, F., 1995, Optical characterization of nanosources used in scanning near-field optical microscopy, *J. Opt. Soc. Am. A* 12(4):695–703.

Watson, T.F., 1989, Real-time confocal microscopy of high speed dental burr/tooth cutting interactions, *Abstracts of the 1st International Conference on Confocal Microscopy and the 2nd International Conference on 3D Image Processing in Microscopy*, Amsterdam, March 15–17, 1989.

Watson, T.F., Azzopardi, A., Etman, L.M., Cheng, P.C., and Sidhu, S.K., 2000, Confocal and mulit-photon microscopy of dental tissues and biomaterials, *Am. J. Dentistry* 13:19–24.

Webb, W.W., 1976, Perspectives on Cell Surface Mobility, In: *Measurement of Lateral Transport on Cell Surfaces* (V.T. Marchesi, ed.), Alan R. Liss, Inc., New York, pp. 276–278.

Wells, K.S., Sandison, D.R., Strickler, J.H., and Webb, W.W., 1990, Quantitative fluorescence imaging with laser scanning confocal microscopy, In: *Handbook of Biological Confocal Microscopy* (J. Pawley, ed.), Plenum Press, New York.

White, J.G., Amos, W.B., and Fordham, F., 1987, An evaluation of confocal vs. conventional imaging of biological structures by fluorescent light microscopy, *J. Cell Biol*. 105:41–48.

Wijaendts van Resandt, W., Marsman, H.J.B., Kaplan, R., Davoust, J., Stelzer, E.H.K., and Stricker, R., 1984, Optical fluorescence microscopy in three dimensions: Microtomoscopy, *J. Microsc.* 138:29–34.

Xiao, G.O., Corle, T.R., and Kino, G.S., 1988, Real-time confocal scanning microscope, *Appl. Phys. Lett*. 53:716–718.

Zochowski, M., Wachowiak, M., Falk, C.X., Cohen, L.B., Lam, Y.W., Antic, S., and Zecevic, D., 2000, Imaging membrane potential with voltage-sensitive dyes, *Biol. Bull*. 198:1–21.